

## BIBLIOGRAPHIC INFORMATION

PB95-124335

Report Nos:

Title: Development of the Generated Sequential Displacement Procedure and the Simulated Seismic Testing of the TCCMAR 3-Story In-Plane Walls.

Date: Jun 93

Authors: A. Igarashi, F. Seible, and G. A. Hegemier.

Performing Organization: United States-Japan Coordinated Program for Masonry Building Research. \*\*California Univ., San Diego, La Jolla. Dept. of Applied Mechanics and Engineering Sciences.

Sponsoring Organization: \*National Science Foundation, Arlington, VA.

Contract Nos: NSF-ECE85-52672

Supplemental Notes: Also pub. as California Univ., San Diego, La Jolla. Dept. of Applied Mechanics and Engineering Sciences rept. no. SSRP-93/04 and United States-Japan Coordinatd Program for Masonry Building Research rept. no. REPT-3.1(B)-2.

NTIS Field/Group Codes: 89D (Structural Analyses), 89G (Construction Materials, Components, & Equipment)

Price: PC A06/MF A02

Availability: Available from the National Technical Information Service, Springfield, VA, 22161

Number of Pages: 118p

Keywords: \*Masonry, \*Earthquake resistant structures, \*Earthquake damage, \*Walls, \*Displacement, \*Dynamic structural analysis, Earthquake engineering, Algorithms, Deformation, Structural vibrations, Buildings, Moments, Structural failure, Degrees of freedom, Dynamic response, Loads(Forces), Damage assessment, USA, International cooperation, Japan, \*Masonry buildings, \*Generated Sequential Displacement Test Method.

Abstract: A testing methodology for subjecting full-scale reinforced concrete masonry structures to simulated seismic loads under laboratory conditions was developed, and the test method implementation and verification on three-story full-scale reinforced masonry shear walls are discussed. The new GSD (Generated Sequential Displacement) test method allows realistic seismic load simulation and the trace of higher mode effects, even in the initial undamaged state of the structure. Problems typically associated with the stiff coupling between servo-controlled actuators in a multi-degree of freedom system were overcome with the introduction of elastomeric loading pads, which act as displacement amplifiers in the loading system. Advances in the on-line actuator control algorithm also allowed testing without artificial numerical damping in the time integration scheme, thus permitting the tested three-degree of freedom structural masonry walls to respond with lateral load implementation verification is described in detail together with seismic response characteristics of the 3-story walls.



PB95-124335



**U.S. - JAPAN COORDINATED PROGRAM  
FOR  
MASONRY BUILDING RESEARCH**

**REPORT NO. 3.1 (b)-2**

**DEVELOPMENT OF THE GENERATED  
SEQUENTIAL DISPLACEMENT  
PROCEDURE AND THE SIMULATED  
SEISMIC TESTING OF THE TCCMAR  
3-STORY IN-PLANE WALLS**

by

**AKIRA IGARASHI  
FRIEDER SEIBLE  
GILBERT A. HEGEMIER**

**JUNE 1993**


**supported by:**

**NATIONAL SCIENCE FOUNDATION**

**GRANT NO. ECE 85-52672**

---

**DEPARTMENT OF APPLIED MECHANICS & ENGINEERING SCIENCES  
UNIVERSITY OF CALIFORNIA, SAN DIEGO**

REPRODUCED BY:   
U.S. Department of Commerce  
National Technical Information Service  
Springfield, Virginia 22161



**This report presents the results of a research project which was part of the U.S. Coordinated Program for Masonry Building Research. The program constitutes the United States part of the United States - Japan Coordinated Masonry Research Program conducted under the auspices of the Panel on Wind and Seismic Effects of the U.S.-Japan Natural Resources Development Program (UJNR).**

**This material is based on work supported by the National Science Foundation under the direction of Program Director, Dr. S.C. Liu.**

**Any opinions, findings, and conclusions or recommendations expressed in this publication are those of the authors and do not necessarily reflect the views of the National Science Foundation and/or the United States Government.**

University of California, San Diego  
Structural Systems Research Project

Report No. SSRP-93/04

**DEVELOPMENT OF THE GENERATED SEQUENTIAL DISPLACEMENT  
PROCEDURE AND THE SIMULATED SEISMIC TESTING OF THE  
TCCMAR 3-STORY IN-PLANE WALLS**

by

***Akira Igarashi***  
Graduate Research Assistant

***Frieder Seible***  
Professor of Structural Engineering

and

***Gilbert A. Hegemier***  
Professor of Applied Mechanics

Department of Applied Mechanics and Engineering Sciences  
University of California, San Diego  
La Jolla, California 92093-0411

June 1993

## TABLE OF CONTENTS

TABLE OF CONTENTS	i
ABSTRACT	iii
ACKNOWLEDGEMENTS	iv
1. INTRODUCTION	1
2. DEVELOPMENT OF ON-LINE TESTING TECHNIQUE	3
2.1. Pseudo Dynamic Testing Technique	3
2.1.1. General Principle	3
2.1.2. Newmark Explicit Method	6
2.1.3. Modified Newmark Explicit Method	6
2.1.4. Hilber's Alpha Method	7
2.2. Difficulties Found in Pseudo Dynamic Testing	7
2.2.1. Integration Schemes	7
2.2.2. Error Propagation Effects	8
2.2.3. Problems with Stiff MDOF Structures	9
2.3. Generated Sequential Displacement (GSD) Test	10
2.3.1. Elastomeric Pads	12
2.3.2. Displacement Amplification and Error Reduction Effect	12
2.3.3. Restoring Force Error Reduction Effect	15
2.3.4. Inner Control Loop	17
3. IMPLEMENTATION OF ON-LINE TESTING FOR THREE-STORY WALL	19
3.1. Loading System	19
3.2. Control Software	21
3.3. Shakedown Tests on Steel Frame	23
3.4. Three-Story Wall Test Specimen	23
3.5. Instrumentation	25
4. TEST DESCRIPTION	30
4.1. Numerical Modeling	30
4.2. GSD Test Implementation and Verification	32
4.3. GSD Test Refinements	38
4.4. Inverse Triangular and Uniform Loading Tests	46
4.5. Stiffness Measurement Test	46
5. BEHAVIOR OF THREE-STORY WALLS	50
5.1. Global Structural Displacement Response	50
5.1.1. Time History	50

5.1.2. Moment and Base Shear vs. Displacement Hysteresis .....	50
5.1.3. Inverse Triangular Loading Tests and Filtered Data .....	50
5.2. Individual Panel Deformations .....	68
5.2.1. Decomposition of Behavior Modes .....	70
5.2.2. Test Results .....	73
5.3. Curvature Distribution .....	73
5.4. Reinforcement Strains .....	86
5.5. Repair and Retest of 3-Story Wall .....	86
6. DEVELOPMENTS FOR THE TCCMAR 5-STORY BUILDING TEST .....	96
6.1. Convergence Analysis .....	96
6.2. Improvement of Convergence .....	101
7. CONCLUSIONS .....	103
REFERENCES .....	104

## **ABSTRACT**

A testing methodology for subjecting full-scale reinforced concrete masonry structures to simulated seismic loads under laboratory conditions was developed, and the test method implementation and verification on three-story full-scale reinforced masonry shear walls are discussed. The new GSD (Generated Sequential Displacement) test method allows realistic seismic load simulation and the trace of higher mode effects, even in the initial undamaged state of the structure. Problems typically associated with the stiff coupling between servo-controlled actuators in a multi-degree of freedom system were overcome with the introduction of elastomeric loading pads, which act as displacement amplifiers in the loading system. Advances in the on-line actuator control algorithm also allowed testing without artificial numerical damping in the time integration scheme, thus permitting the tested three-degree of freedom structural masonry walls to respond with lateral load distribution patterns consistent with the degree of structural stiffness deterioration. The GSD implementation verification is described in detail together with seismic response characteristics of the 3-story walls.

## **ACKNOWLEDGEMENTS**

**The present research was funded by the National Science Foundation under NSF Grant No. BCS 85-18701. The construction of the three-story wall test structure was donated by the Masonry Association of California and Nevada, and ready-mix grout was donated by the San Diego Rock Producers Association.**



## **1. INTRODUCTION**

Modern design of structural systems for seismic loading relies heavily on inelastic deformations to absorb the seismic energy input by large inelastic deformations at reliable capacities rather than by large capacities at small deformation levels. Thus, earthquake resistant structural systems will experience local distress and need to accommodate large inelastic deformation cycles without significant deterioration of design capacity levels. Since the structure is expected to perform well beyond the proportionality or yield limit state during its lifetime, traditional analysis and design models, which relate unfactored or factored design loads and linear elastically determined demand to service or ultimate capacity levels, are no longer appropriate to capture the relevant realistic structural response. Thus, new analysis and design tools are needed which can (1) realistically capture the post-yield to ultimate deformation limit state response, (2) account for realistic seismic load input and (3) determine the location and nature of local and global failure modes.

A large number of complex nonlinear analysis models and advanced capacity design models have been developed in the academic research environment, but the quality and usefulness of these models depends to a large extent on their appropriate verification and calibration. Since the unpredictable and devastating nature of earthquakes allows gathering of post-yield field data only to a very limited degree, the validation of these models depends largely on experimental laboratory testing. These laboratory tests need to be performed at a large or full scale in order to capture the correct onset and development of failure modes at the local level, and their complex interaction at the global structural systems level. Since failure mechanisms and their nonlinear behavior are typically controlled by the structural detailing of joints, connections etc., only limited scaling is permissible in the experimental verification. Thus, experimental techniques are needed, which can take complete full or large scale structural systems under realistic seismic

load input from the undamaged initial state through the yield limit state and the formation of local mechanisms all the way to the final global collapse mode. Realistic seismic load input to these full scale models requires not only the application of mass proportional loading but also the participation of the structure in the load determination, both, in terms of stiffness degradation effects on the dynamic response characteristics and in terms of higher mode effects.

In an effort to develop new design guidelines for masonry structures in seismic zones, the TCCMAR[1] (Technical Coordinating Committee for Masonry Research) has conducted extensive experimental and analytical research in both the U.S. and Japan to provide a broad data base for analysis and design model development. The final verification of the developed procedures and models is by means of a five-story full scale reinforced concrete masonry building test under simulated seismic load input. A detailed description of the development of the test procedure for the U.S.-TCCMAR five-story full scale research building test is provided in the following. After a brief introduction of the theoretical basis for simulated seismic on-line testing, the GSD (Generated Sequential Displacement) test procedure is presented, starting with a general description of the test methodology and the formulation of the test method, followed by the test method implementation, verification and fine-tuning, and an interpretation of obtained test results from full scale multi-story reinforced concrete masonry shear wall systems. It should be noted, that the primary objective of the described work was not the development of new pseudo-dynamic testing theories or techniques but rather the application and refinement of existing procedures to allow the on-line testing of stiff multi-degree of freedom systems under seismic load input.

## 2. DEVELOPMENT OF ON-LINE TESTING TECHNIQUE

The on-line testing of stiff multi-degree-of-freedom masonry shear wall structure requires enhancements to the conventional pseudo dynamic testing technique. In this chapter, the theoretical development of the GSD test procedure is described.

### 2.1. Pseudo Dynamic Testing Technique

Because real-time testing of full-scale structural systems under seismic excitation is usually not practical, a combined analytical, experimental technique, called the pseudo-dynamic method, was developed in Japan[5] and in the U.S.[9] This method quasi-statically simulates seismic response in the time domain. A brief overview of the governing principles is presented in the following.

#### 2.1.1. General Principle

If the structural system can reasonably be represented by a discrete system, its equation of motion is expressed by

$$\mathbf{M}\ddot{\mathbf{d}}(t) + \mathbf{C}\dot{\mathbf{d}}(t) + \mathbf{r}(t) = \mathbf{f}(t) \quad (2.1)$$

where

- $t$  : time
- $\mathbf{M}$  : mass matrix
- $\mathbf{C}$  : damping matrix
- $\mathbf{d}(t)$  : structural displacement vector
- $\mathbf{f}(t)$  : excitation force vector

For a linear elastic structure, the structural restoring force vector  $\mathbf{r}(t)$  is expressed by the product

of stiffness matrix  $\mathbf{K}$  and displacement vector  $\mathbf{d}(t)$ , as

$$\mathbf{r}(t) = \mathbf{K}\mathbf{d}(t) \quad (2.2)$$

Given the initial conditions, this equation is solved numerically by an appropriate time integration scheme, giving structural displacements  $\mathbf{d}(t_i)$  at discrete time steps ( $i=1,2,\dots$ ). In the pseudo-dynamic technique the mass and damping characteristics of the structure are modeled analytically, whereas the typically nonlinear structural restoring forces  $\mathbf{r}(t_i)$ , are measured experimentally. After the proper starting procedure, the structural displacements calculated at each time step are imposed on the test structure by means of servo-controlled hydraulic actuators, and the resulting restoring forces  $\mathbf{r}(t_i)$  are measured and used in the analytical model to compute the displacements at the next time step. A schematic overview of the procedure is shown in Fig.2.1 and the outline of the algorithm is as follows:

- 1) Provide or assume initial conditions for the structure and set time step  $i=0$ .
- 2) Using the input forcing function  $\mathbf{f}(i)$ , calculate the displacements  $\mathbf{d}(i)$  at the next step by means of a numerical time integration scheme.
- 3) Impose the calculated displacements to the specimen with servo controlled actuators.
- 4) Measure with built-in load cells the restoring forces  $\mathbf{r}(i)$ , see eqn. (2.2).
- 5) Set  $i$  to  $i+1$  and go to step 2.

The algorithm may vary slightly according to the particular numerical time integration scheme used. Explicit and implicit integration schemes have both been used by various researchers with varying degrees of success. In the present work, three numerical integration schemes were used: the Newmark Explicit method, the Modified Newmark Explicit method and Hilber's alpha method. These are outlined in the following.

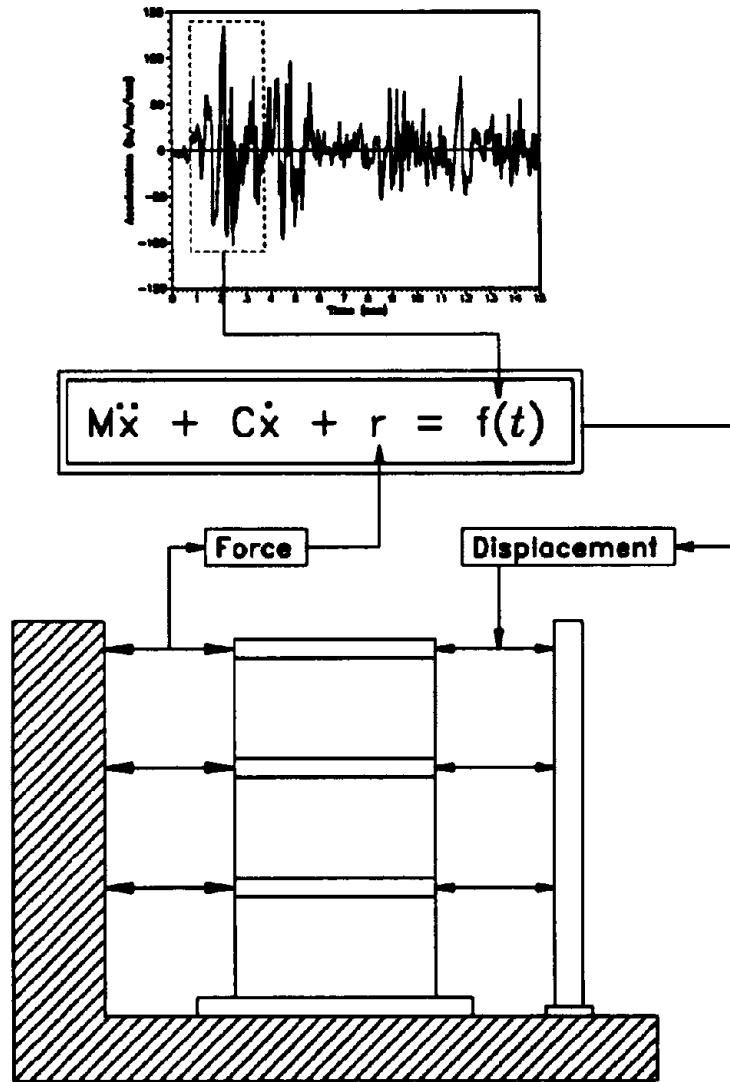


Fig. 2.1. Schematic Pseudo Dynamic Test Procedure

### 2.1.2. Newmark Explicit Method

This scheme can be summarized by

$$\begin{aligned}d(i+1) &= d(i) + \Delta t v(i) + \frac{\Delta t^2}{2} a(i) \\v(i+1) &= v(i) + \frac{\Delta t}{2} (a(i) + a(i+1)) \\a(i+1) &= \left[ M + \frac{\Delta t}{2} C \right]^{-1} \left( f(i+1) - r(i+1) - C v(i) - \frac{\Delta t}{2} C a(i) \right)\end{aligned}\tag{2.3}$$

where  $\Delta t$  is the integration time interval. The method has no numerical damping and is stable only if  $\omega \Delta t \leq 2$ , where  $\omega$  represents the highest natural circular frequency of the system. Thus, very small time steps are generally required for numerical stability, particularly for stiff multi-degree of freedom systems.

### 2.1.3. Modified Newmark Explicit Method

This method can be described by

$$\begin{aligned}d(i+1) &= d(i) + \Delta t v(i) + \frac{\Delta t^2}{2} a(i) \\v(i+1) &= v(i) + \frac{\Delta t}{2} (a(i) + a(i+1)) \\a(i+1) &= M^{-1} \{ f(i+1) - (1 + \alpha) r(i+1) + \alpha r(i) \} + \frac{\rho}{\Delta t^2} (d(i) - d(i+1))\end{aligned}\tag{2.4}$$

in which  $\alpha$  and  $\rho$  are constants. Approximately frequency-proportional numerical damping can be achieved by the appropriate choice of  $\alpha$  and  $\rho$ . It has been shown that this method is less sensitive to experimental error propagation effects than the central difference method [4,6]. Upper and lower stability bounds for  $\omega \Delta t$  are determined by the condition

$$\sqrt{\frac{-\rho}{\alpha}} \leq \omega \Delta t \leq \frac{1 + \sqrt{1 - (1 + \alpha)\rho}}{1 + \alpha} \quad (2.5)$$

with  $\alpha > 0$  and  $\rho < 0$ .

#### 2.1.4. Hilber's Alpha Method

This implicit integration scheme can be described by

$$\begin{aligned} M\mathbf{a}(i+1) &= (1 + \alpha)\mathbf{f}(i+1) - \alpha\mathbf{f}(i) - (1 + \alpha)\mathbf{r}(i+1) + \alpha\mathbf{r}(i) - (1 + \alpha)\mathbf{C}\mathbf{v}(i+1) + \alpha \\ \mathbf{d}(i+1) &= \mathbf{d}(i) + \Delta t\mathbf{v}(i) + \Delta t^2 \left\{ \left( \frac{1}{2} - \beta \right) \mathbf{a}(i) + \beta \mathbf{a}(i+1) \right\} \\ \mathbf{v}(i+1) &= \mathbf{v}(i) + \Delta t \{ (1 - \gamma)\mathbf{a}(i) + \gamma \mathbf{a}(i+1) \} \end{aligned} \quad (2.6)$$

where  $\alpha$ ,  $\beta$  and  $\gamma$  are integration constants. Although advantages in terms of stability and numerical energy dissipation can be expected, implementation of this method to pseudo-dynamic testing requires considerable effort because it is an implicit method ( Note that the definition of  $\mathbf{d}(i+1)$  contains  $\mathbf{a}(i+1)$  ) and requires an iterative procedure, as well as an estimate of the stiffness matrix. An example of the implementation of this method is given in a paper by Shing and Manivannan[14].

## 2.2. Difficulties Found in Pseudo Dynamic Testing

### 2.2.1. Integration Schemes

Although explicit integration schemes can determine the displacements at the next step from the current displacements, the maximum time step for stable operation can be very small. Small time steps lead to long tests, that in turn introduce other problems such as stress relaxation and the acceleration of error accumulation and propagation effects. Implicit schemes, in general, have much better stability characteristics, allowing larger time steps and thus shorter experiments with

less error. However, they inevitably require an iterative process to determine the next displacement vector, using an estimate of the tangent stiffness of the structure. In spite of the problem of stiffness determination in nonlinear structures, recent progress has been made [13,14], and an implicit integration scheme is being developed for use in the testing of TCCMAR 5-Story research building at University of California, San Diego [22].

### 2.2.2. Error Propagation Effects

The propagation of experimental errors in measuring structural displacements and restoring forces, as well as in imposing the calculated displacements on the test structure accurately, can cause problems in MDOF systems. These problems are manifested in the appearance of spurious higher mode response. This effect is especially acute for stiff MDOF structures, where very small errors in imposed displacements can translate to high restoring force deviations. Error propagation effects have been extensively studied [12,15,16]. Integration schemes with numerical damping can reduce this problem of spurious higher mode response, and various schemes for applying corrections to the measured structural restoring forces based on measured displacement errors and an estimate of the tangent stiffness matrix have also been successfully implemented. Nakashima and Kato [16] proposed new algorithms to suppress the response error growth caused by the displacement error. In these algorithms, the measured restoring force is modified in accordance with the detected displacement error and the initial elastic stiffness or the instantaneous stiffness estimated in each step of loading. This modified restoring force is then incorporated into the equation of motion to calculate the next displacement level. It appears that improving the accuracy of the imposed structural displacements and the measurement of the restoring forces, requiring high quality equipment, is still the single most important factor in reducing error propagation effects in simulated seismic on-line testing.



### 2.2.3. Problems with Stiff MDOF Structures

The testing of stiff MDOF systems, such as multi-story shear walls, present additional difficulties. The stability condition (if any) of the integration algorithm for such systems is typically governed by the highest natural frequency which may be very high for stiff structures, thus requiring small time steps and the imposition of very small displacement increments at the active or controlled degrees of freedom. These may easily be beyond the resolution of the hydraulic actuators used to impose them. Also, the stiff coupling between active DOFs in a stiff MDOF system, combined with geometric amplification effects controlled by the systems geometry, results in actuator control problems for small displacement levels, since individual actuator adjustments can cause large deformations in coupled DOFs. Relative displacement errors and resulting restoring force errors can then be high, resulting in error accumulation and ultimately in erroneous structural response. Since pseudo-dynamic testing is essentially a displacement-controlled test procedure, displacement errors and their accumulative effects will be directly reflected in the test results. For a known load-displacement relationship, one could use a scheme which employs load-controlled actuators to impose the specified structural displacement, but this idea is irrelevant to a structure that inherently has highly nonlinear behavior characteristics.

Another difficulty is the proper simulation of mass proportional inertia loading. While it is commonly accepted for building systems to apply lateral seismic loads at the floor slabs, long buildings and particularly coupled shear wall structures require mass proportional load input along the length of the floor slab which should be independent of the structural deterioration of the floor system. In addition, the distributed loading system should not constrain or alter the floor slab rotations or deformations.

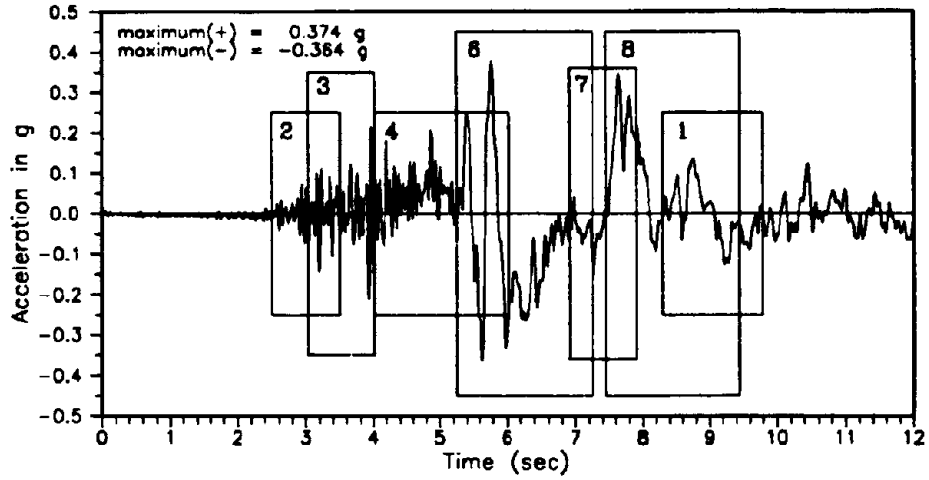
The methodology used in testing 3-story reinforced masonry shear walls, as described in this report, was designed to overcome some of these difficulties. The method entails two essential features: an improved loading system, and a dual control algorithm for imposing structural displacements. The detail of the methodology is presented in the following section.

### **2.3. Generated Sequential Displacement (GSD) Procedure**

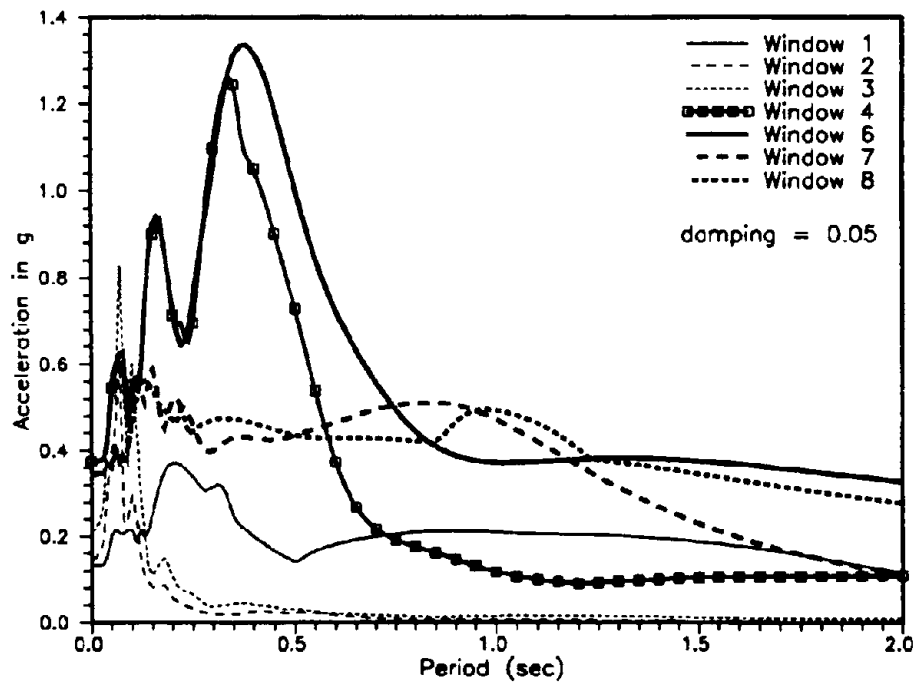
As a direct extension of the pseudo-dynamic on-line technique, the GSD procedure was developed for the full scale seismic testing of stiff multi-degree of freedom structures. Since the method was developed in direct support of models for design guidelines, the test procedure must allow the test structure to be exposed to seismic input segments which cause structural response representative of critical design limit states. Thus, a carefully selected sequence of input segments is developed which will not only provide the structural response to one particular seismic event but rather a sequence of critical structural response states including higher mode effects which need to be considered in the design process.

An example of such a sequential load side definition is provided in Fig. 2.2a where the James Rd 230° component of the 1979 Imperial Valley acceleration record was used to provide input segments of various response characteristics as diagnosed by the corresponding segment response spectra, see Fig. 2.2b. Based on the measured structural stiffness characteristics, an appropriate input segment can now be selected and scaled to produce the desired critical design limit state.

Displacements generated by these input segments through a numerical time integration scheme must now be applied sequentially to the test structure as mass proportional floor loads. Thus, the GSD test method consists of four components: (1) the selected sequence of recorded or generated seismic ground motion input segments, (2) the analytical model and the numerical time integration scheme (typically referred to as the outer loop of the control system), (3) the computer-controlled inner loop of the on-line servo-controlled actuator system, and (4) the actuator and loading system itself with ramp generator and servo-control. Since pseudo dynamic test applications and developments are reported in detail in [5 to 16], only modifications to the basic concept are reported in the following.



(a) Time History



(b) Response Spectra

Fig. 2.2. Segments Selected from Imperial Valley 1979 Earthquake, James Rd. 230° Record

### 2.3.1 Elastomeric Pads

The idea behind the use of elastomeric pads is that they act as (a) equal load distributors, and (b) soft springs between actuators and the specimen (structure). The first feature provides a mass-proportional loading to the specimen, and limited unconstrained structural rotations and expansions of the floor system, thus allowing structural deterioration without compromising the mass proportional loading. The second feature, which is illustrated in Fig. 2.3 on a 2-DOF system, improves the displacement control of the structure at small displacement levels through displacement amplification and reduces coupling between DOFs. It also protects the structure from actuator instabilities during shake down testing. The mechanical displacement amplification from this soft spring effect of the elastomeric pads is discussed in the next section.

### 2.3.2. Displacement Amplification and Error Reduction Effect

In the following, symbols with a hat (^) refer to "actually measured" or "experimental" values, while symbols without a hat represent values which are "computed" or "idealized". Consider a structure with  $n$  degrees of freedom, and the actuator displacements as an  $n$ -dimensional vector  $\mathbf{x}_a$  and structural displacements as an  $n$ -dimensional vector  $\mathbf{x}$ . Let us assume that the actuators cannot be controlled precisely, resulting in an actuator displacement error  $\hat{\mathbf{x}}_a - \mathbf{x}_a$  with an actuator displacement error bound  $\delta$  of the form

$$\|\hat{\mathbf{x}}_a - \mathbf{x}_a\| \leq \delta \quad (2.7)$$

where  $\mathbf{x}_a$  is the calculated actuator displacement vector or command signal, and  $\|\cdot\|$  represents the norm of a vector. The value of the actuator displacement error bound is dependent on the servo controlled actuator system and cannot be zero. If the actuators are directly connected to the specimen without elastomeric pads, the (experimental) structural displacement vector  $\hat{\mathbf{x}}$  will be such that

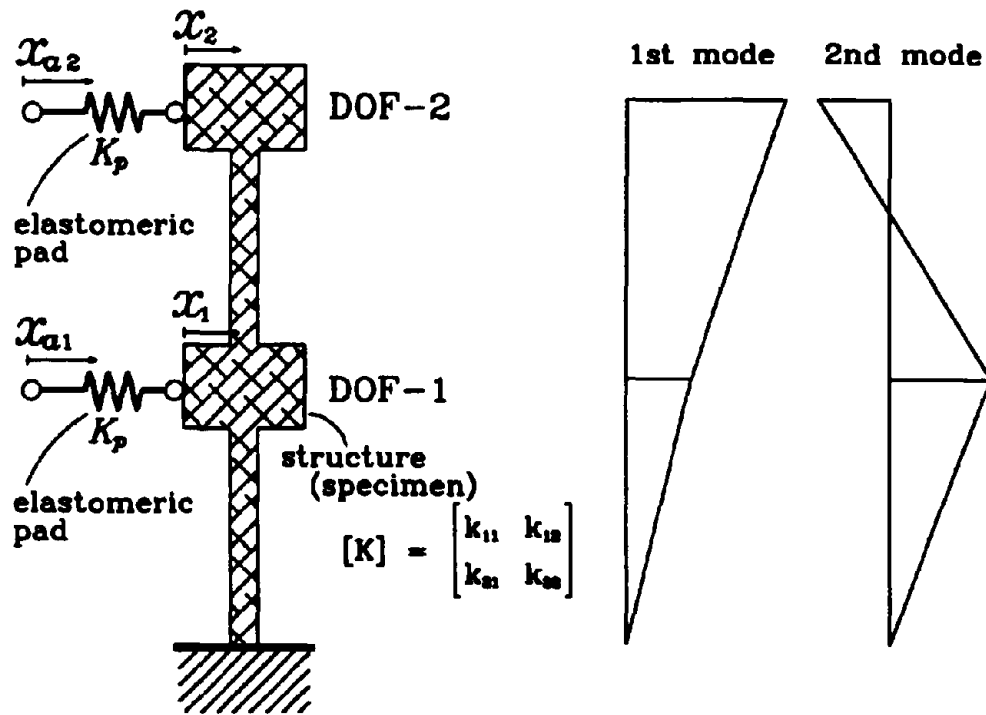


Fig. 2.3. Linear 2-DOF System Model

$$\|\hat{x} - x\| \leq \delta \quad (2.8)$$

This indicates that the error bound for the structural displacement is also  $\delta$ , i.e. the precision of the structural displacements is equal to the precision of the actuator displacements.

Now, consider the case in which the specimen and the actuators are connected through elastomeric pads. This situation is described by the model shown in Fig. 2.3. The actuator displacement vector and the structural displacement vector are related by

$$\hat{x}_a = Q\hat{x} \quad (2.9)$$

where  $Q$  is an  $n \times n$  "displacement amplification matrix", which can be expressed by

$$Q = I + \frac{1}{k_p}K \quad (2.10)$$

where  $k_p$  is the elastomeric pad stiffness,  $K$  is the stiffness matrix of the structure. It can be shown from the above relations that  $\|\hat{x}_a\| \geq \|\hat{x}\|$ , so the actuator displacement is greater than the structural displacement. For a stiff structure, this amplification is substantial due to the large contribution of the second term in eqn. (2.10). In this case where the structural displacement tends to be small, the amplification effect will be beneficial. Since

$$\hat{x} - x = Q^{-1}(\hat{x}_a - x_a) \quad (2.11)$$

the structural displacement error can be bounded as follows:

$$\begin{aligned} \|\hat{x} - x\| &\leq \|Q^{-1}\|_2 \|\hat{x}_a - x_a\| \\ &\leq \|Q^{-1}\|_2 \cdot \delta \end{aligned} \quad (2.12)$$

where  $\|\cdot\|_2$  denotes the two-norm of a matrix [19]. If the stiffness matrix  $K$  is positive definite, the matrix  $Q^{-1}$  is also positive definite, and in this case, the two-norm of the matrix  $Q^{-1}$  is

simply the largest eigenvalue of  $Q^{-1}$ , i.e.

$$\begin{aligned} \|Q^{-1}\|_2 &= \left\| \Phi \operatorname{diag} \left( \frac{1}{1 + \frac{\lambda_1}{k_p}}, \dots, \frac{1}{1 + \frac{\lambda_n}{k_p}} \right) \Phi^T \right\|_2 \\ &= \frac{1}{1 + \frac{\lambda_1}{k_p}} \end{aligned} \quad (2.13)$$

where  $\lambda_i$  ( $i=1,2,\dots,n$ ) is the eigenvalue of the stiffness matrix  $K$  for the  $i$ th mode, and  $\Phi$  is the matrix consisting of eigenvectors  $\varphi_i$  such that  $K\varphi_i = \lambda_i\varphi_i$  and  $\|\varphi_i\|=1$ . Note that these eigenvectors coincide with the dynamic mode shapes if the lumped masses are equal for all the DOFs. Therefore,

$$\|\hat{x} - x\| \leq \frac{\delta}{1 + \frac{\lambda_1}{k_p}} \quad (2.14)$$

This result indicates that by using a small elastomeric pad stiffness  $k_p$ , the structural displacement error vector  $\hat{x} - x$  can be made smaller than the actuator precision.

### 2.3.3. Restoring Force Error Reduction Effect

It can also be shown that the elastomeric pads lessen the restoring force error resulting from inaccurate actuator displacements, and reduce the coupling between structural DOFs, thus almost eliminating spurious higher mode interaction effects during the initial load stages at which the structure is undamaged and stiff.

Let  $f$  be the restoring force vector when  $x_u$  is achieved. The assumption (2.7) is also used here to evaluate the error in the restoring forces when the actuator displacement error is not negligible.

When the actuators are directly connected to the structure, structural displacements are

equal to the actuator displacements, and restoring force vectors are given by

$$\begin{aligned} f &= Kx_a \\ \hat{f} &= K\hat{x}_a \end{aligned} \quad (2.15)$$

Consequently, the restoring force error can be bounded as follows:

$$\begin{aligned} \|\hat{f} - f\|_2 &= \|K(\hat{x}_a - x_a)\|_2 \\ &\leq \|K\|_2 \|\hat{x}_a - x_a\|_2 \\ &\leq \|K\|_2 \delta \end{aligned} \quad (2.16)$$

Since  $K$  is assumed to be positive-definite,  $\|K\|_2 = (\text{largest eigenvalue of } K) = \lambda_n$ . Therefore, we have

$$\boxed{\|\hat{f} - f\|_2 \leq \lambda_n \delta} \quad (2.17)$$

Consider the case where elastomeric pads are applied between the actuators and the test structure. The apparent stiffness matrix  $K_{app}$  including the effect of the elastomeric pads is defined to satisfy the relation

$$K_{app} x_a = f \quad (2.18)$$

If the elastomeric pad stiffness is uniform for all the DOFs with the value  $k_p$ , this apparent stiffness matrix is given by

$$K_{app} = \left[ K^{-1} + \frac{1}{k_p} I \right]^{-1} \quad (2.19)$$

and can be diagonalized as



$$\mathbf{K}_{\text{app}} = \Phi \text{diag} \left( \frac{1}{\frac{1}{\lambda_1} + \frac{1}{k_p}}, \frac{1}{\frac{1}{\lambda_2} + \frac{1}{k_p}}, \dots, \frac{1}{\frac{1}{\lambda_n} + \frac{1}{k_p}} \right) \Phi^T \quad (2.20)$$

with the two-norm of

$$\|\mathbf{K}_{\text{app}}\|_2 = \frac{1}{\frac{1}{\lambda_n} + \frac{1}{k_p}} = \frac{\lambda_n}{1 + \frac{\lambda_n}{k_p}} \quad (2.21)$$

With the same argument as in the previous case, the restoring force error is now bounded by

$$\|\hat{f} - f\|_2 \leq \|\mathbf{K}_{\text{app}}\|_2 \delta \quad (2.22)$$

Hence, by eqn. (2.21), we have

$$\boxed{\|\hat{f} - f\|_2 \leq \frac{\lambda_n \delta}{1 + \frac{\lambda_n}{k_p}}} \quad (2.23)$$

Comparing the results of eqn. (2.17) and eqn. (2.23), it can be concluded that the application of elastomeric pads permits the reduction of the restoring force error by a factor of

$$\frac{1}{1 + \frac{\lambda_n}{k_p}} \quad (< 1)$$

This factor depends on the higher eigenvalue  $\lambda_n$  of the stiffness matrix  $\mathbf{K}$  and therefore turns out to be even smaller than the error reduction factor for structural displacement which appears in eqn. (2.14) and depends on the lowest eigenvalue of  $\mathbf{K}$ .

#### 2.3.4. Inner Control Loop

Although the introduction of the elastomeric pads provides the discussed advantages for stiff multi-degree-of-freedom system, it also adds complications to the actuator control algorithm. For a highly nonlinear test structure, it is difficult to obtain the actuator displacement which provides the target structural displacement specified by the pseudo-dynamic algorithm. An iterative procedure to search for the appropriate actuator displacement vector must be implemented.

The inner control loop can be described as follows: After the structural displacement measurements are compared with calculated target displacement levels in a software control loop, the structural displacement increments to be imposed are obtained. These increments are then appropriately scaled (to improve convergence and test speed) and used as the next actuator displacement increment.

This inner loop algorithm can be expressed by either

$$\mathbf{x}_a^{(k+1)} = \mathbf{x}_a^{(k)} + v(\mathbf{x}_{target} - \mathbf{x}^{(k)}), \quad k=0,1,\dots \quad (2.24)$$

or

$$\mathbf{x}_a^{(k+1)} = \mathbf{x}_a^{(k)} + v(\mathbf{x}_{target} - \mathbf{x}^{(k)}), \quad k=0,1,\dots \quad (2.25)$$

with  $k$  denoting the inner loop iteration step and  $v$  the displacement increment scale factor.

### **3. IMPLEMENTATION OF GSD ON-LINE TESTING FOR THREE-STORY WALLS**

The GSD test method was implemented on three-story reinforced masonry shear walls. Two three-story wall specimens were used, and the schematic test setup is depicted in Fig.3.1. The loading system of the test structure consisted of three pairs of servo-controlled hydraulic actuators, load distribution beams and elastomeric loading pads. The actuator forces were reacted against the UCSD Structural Systems Laboratory's 50 ft (15.24m) reaction strong wall. The six actuators were controlled and monitored by computers (VAX workstations) through Analog-Digital and Digital-Analog converters. Since high accuracy was required from the instrumentation for the test control, this group of instruments was treated separately from other general instrumentation, which was installed to record structural response characteristics.

#### **3.1. Loading System**

To properly simulate mass proportional floor loading, loads have to be uniformly introduced to the test structure not only along the length of the test building but also over the width. Thus, two actuators were employed per floor level, which will ultimately also allow the testing of a building under torsional response as long as the actuators are force coupled, and prevent torsional response when the actuators are displacement slaved. Two 165-kip (733.9kN) actuators with  $\pm 6.00$  inch (152.4mm) stroke were used to load the structure at each floor level through the arrangement shown in the Fig. 3.1. One of the two actuators, designated as "master", was controlled in displacement command by the software through a digital interface. The load cell output from the master actuator was then fed into the load controlled slave actuator as a command signal. Because of the tight analog coupling, the net effect is that of a single displacement controlled actuator with uniform loading on both sides of the wall.

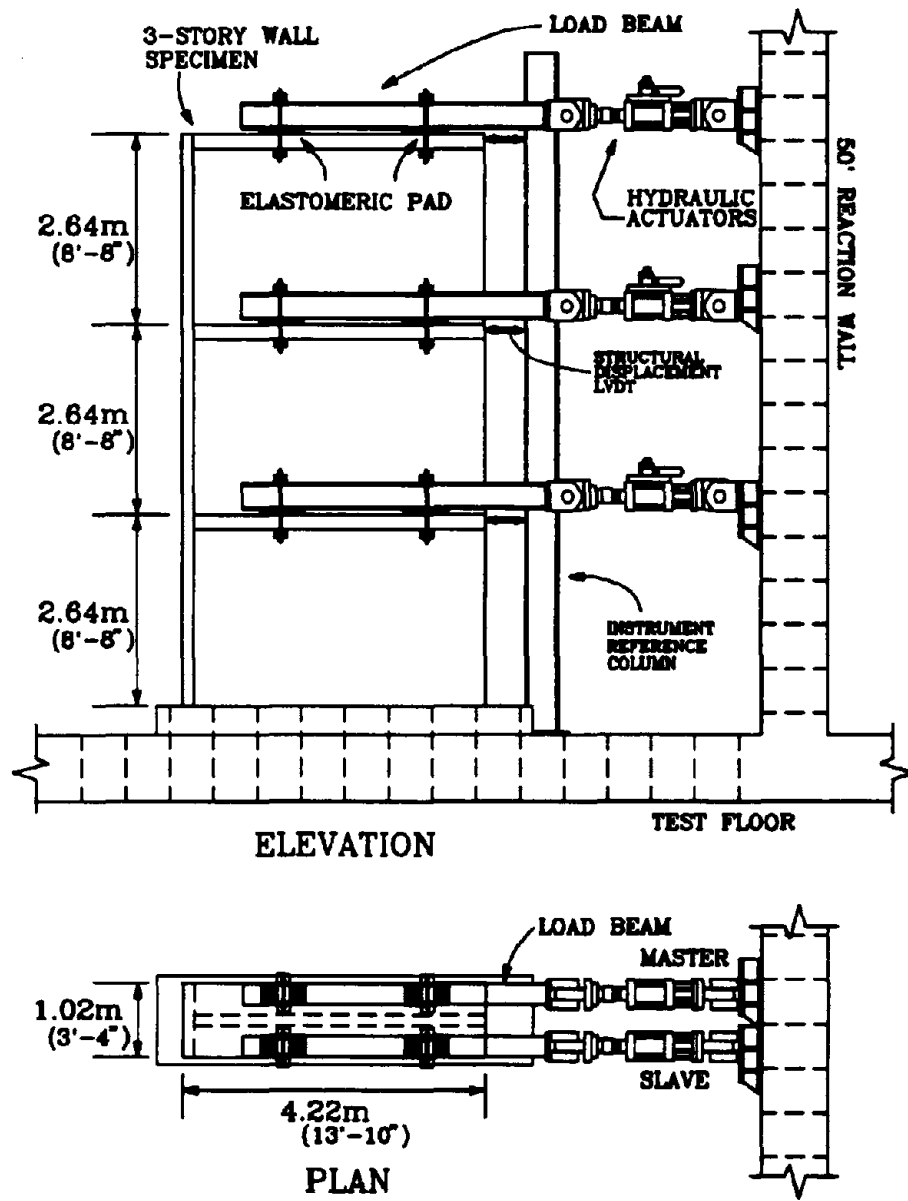


Fig. 3.1. Three-Story Wall Test Setup and Dimensions

The actuators were connected to the shear wall via stiff load beams and soft 1/2 inch (12.7mm) thick elastomeric pads. A vertical preload of up to 100 kips (444.8kN) was applied to each of the elastomeric pads to allow friction based load transfer. There exists the danger that the actuators reach their stroke limit with this displacement amplification due to elastomeric pads. However, with the small elastomeric pad thickness of 1/2" used for the tests shown in Fig. 3.1, higher amplification is obtained at low load levels when displacements are very small, while the amplification effect decreases with increasing loads due to deformation constraint in the elastomeric pads at strain levels exceeding 100%.

### 3.2. Control Software

The control algorithm developed for the GSD procedure is summarized in Fig.3.2. The essential feature of the algorithm is the use of an "outer" and an "inner" software loop. The outer loop calculates the structural displacements to be imposed through the pseudo-dynamic algorithm at each time-step. These target displacements are provided to the inner loop, which calculates the necessary actuator displacements.

The inner loop can be described as follows: The actual structural displacements are measured, and the difference between the target and actual structural displacements is multiplied by a scale factor, resulting in an incremental actuator displacement for the next sub-iteration. This increment is added to the current actuator displacement to arrive at the next desired actuator displacement, which is subsequently applied through a ramp generator to the displacement controlled master actuator. The structure is moved and the new structural and actuator positions are measured. The process is then repeated until the measured and target floor displacements satisfy certain convergence criteria, such as a specified displacement error tolerance (for example,  $\pm 0.001$  in. =  $\pm 0.025$  mm).

Equations (2.24) and (2.25) were both tested as the inner control loop algorithm, and it was found that the algorithm in eqn. (2.25) provided faster convergence and less structural

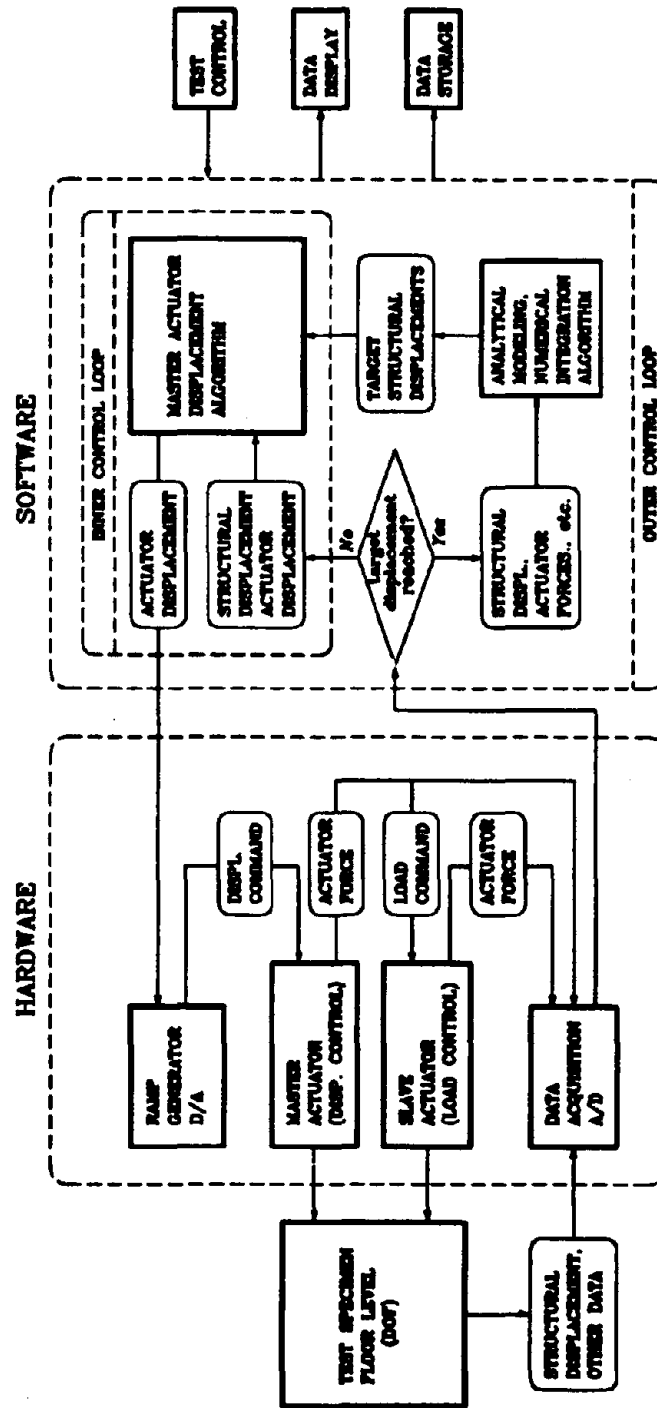


Fig. 3.2. Flow Chart of GSD Procedure and Testing System

displacement error than eqn. (2.24) as described in the next chapter. The reason for the better performance of eqn. (2.25) is in the incompletely linear (and possibly off-biased) relationship between the command signal (  $x_g^{(k)}$  ) and the actuator displacement (  $x_g^{(k)}$  ).

It can be shown that if the value of the multiplier  $\nu$  lies between 0 and 2, the convergence of the structural displacement to the target displacement is guaranteed. However, the most suitable value of the multiplier depends on the anticipated bearing pad displacement amplification. The value of the multiplier should be chosen such that oscillation of the structural displacement increments (i.e. flip flopping) is avoided.

When the desired structural displacements are reached the restoring forces are measured and are used in the outer loop to calculate the next structural target displacement. This process is repeated for all required acceleration input segments.

### **3.3. Shakedown Tests on Steel Frame**

Before the three-story wall specimens were tested, a series of simulated GSD tests on a steel frame were carried out for the purpose of the checking the algorithms and test methods for MDOF systems and the performance of the physical testing system and equipment. The steel frame was tested as a 2-DOF system, and pseudo dynamic tests simulating the response of the steel frame under El Centro record, under free vibration response etc. were performed. These tests provided a shakedown of the basic techniques for the GSD procedure for MDOF structures, including stiffness measurement procedures, which allow the determination of the structural damage state. After the shakedown tests at linear-elastic levels of response, the steel frame was subsequently used as the independent reference frame to measure the structural displacements.

### **3.4. Three-Story Wall Test Specimen**

The RM (reinforced masonry) test specimen, shown in Fig.3.3, was built with 6-inch (152.4 mm) hollow block concrete masonry units. All wall reinforcement consisted of No.4 (12mm  $\phi$ ) bars.

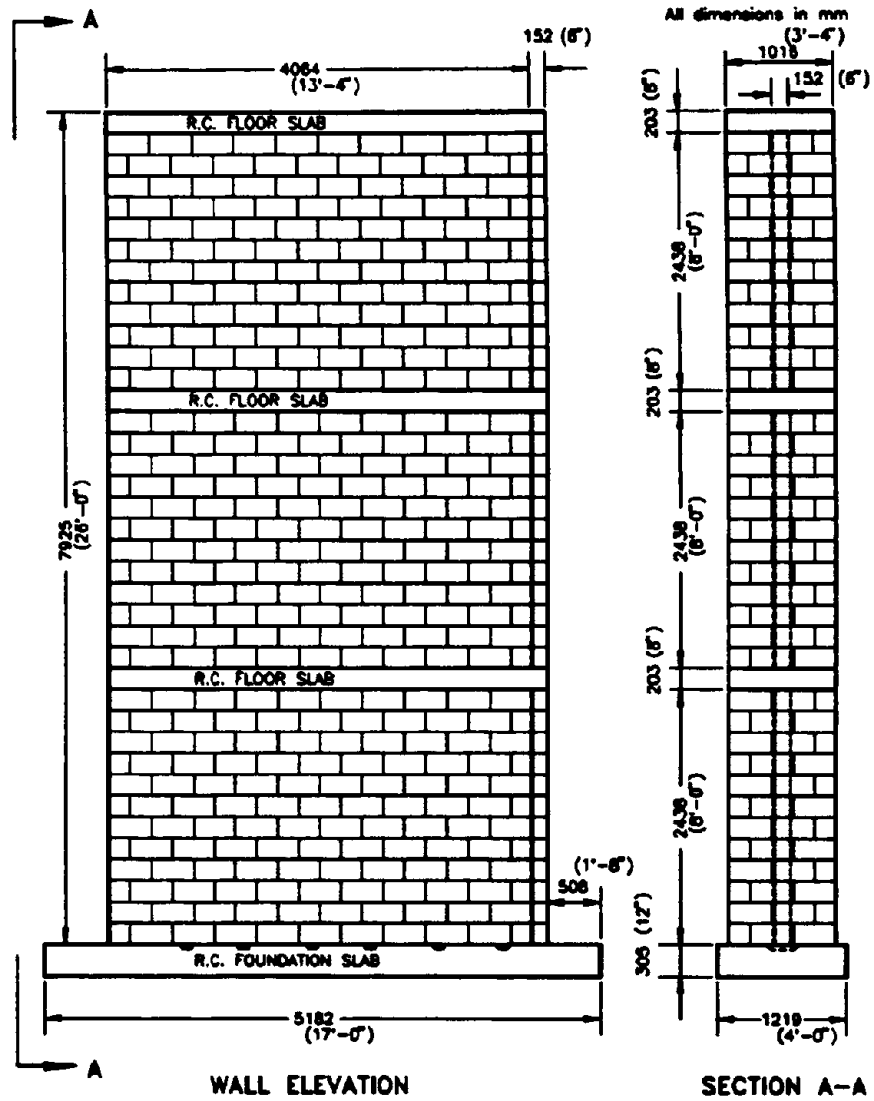


Fig. 3.3. Three-Story Wall Specimen Dimensions



The horizontal reinforcement bars were spaced at 16 in. (406.4 mm), and the vertical reinforcement bars were arranged as shown in Fig.3.4. The walls were fully grouted with normal weight Portland cement concrete with 3/8" max. aggregate size and GroutAid. The base and floor slabs used No.6 and No.4 bars. All reinforcement was Grade 60. Tapered and greased shear keys were provided between the wall and the footing (see Fig.3.3) to prevent sliding between the base and the bottom masonry course. The splicing of vertical reinforcement at the wall bases followed common industry practice and the splice length was 20 inches (508 mm, 40 bar diameters). The specimen was in contact with the laboratory test floor through a 0.5-in. (12.7 mm) layer of hydrostone to provide an even bearing surface. The footing was post-tensioned to the test floor with 2x8 #10 high strength Grade 150 thread bars on 2-ft (609.6mm) centers. This tie down arrangement resulted in no measurable base sliding throughout the test series. During construction material test samples were obtained for the grout and 3-course high masonry block test prisms were built and tested for each floor. These material tests resulted in a nominal masonry compressive strength of  $f'_m = 1890$  psi (13.03 N/mm<sup>2</sup>). The reinforcement bars were tested for yield strength, and an average value of 62 ksi (427.5 N/mm<sup>2</sup>) was obtained.

### 3.5. Instrumentation

The instrumentation was designed to provide information in two specific areas: (1) test control and (2) structural response. The structural displacement and restoring force information required for the pseudo-dynamic algorithm was provided by 3 LVDTs measuring floor displacements (at the center of floor slabs) relative to an independent instrumentation column placed between the specimen and the reaction wall and by 6 load cells attached to the hydraulic actuators, see Fig.3.1. The LVDTs measuring the structural displacements had a range of  $\pm 0.2$  in. ( $\pm 5$  mm) for tests on the stiff, undamaged structure. Extended range LVDTs were used to accommodate greater floor displacements after the structure softened. The analog circuitry of the load cells was also optimized to the anticipated load levels. To further reduce displacement measurement errors,

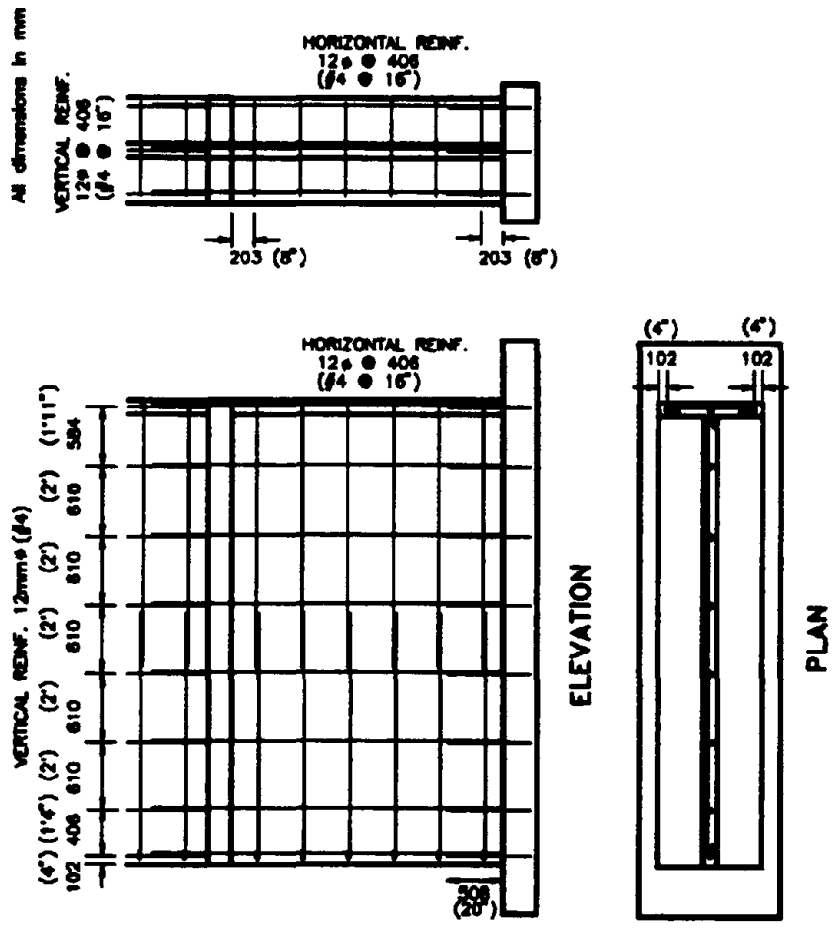


Fig. 3.4. Typical Wall Panel Reinforcement Detail

the average of at least 25 A/D readings for each displacement channel was used in the outer control loop calculations.

Figures 3.5 and 3.6 show the structural response instrumentation layout. Reinforcing bar strain gages, see Fig. 3.5, were used on all starter and continuation bars at the first floor level and in regions of highest expected strains in the second and third story wall panels. Slippage between the laboratory test floor and wall base, and between floor slabs and walls, was monitored by a set of LVDTs. Linear potentiometers were installed at the web and flange ends of the first story wall panel to provide first floor curvature information, as shown in Fig. 3.6. Figure 3.6 also shows the set of 13 LVDTs installed between the corners of the wall panels to monitor the overall deformation modes of the individual wall panels.

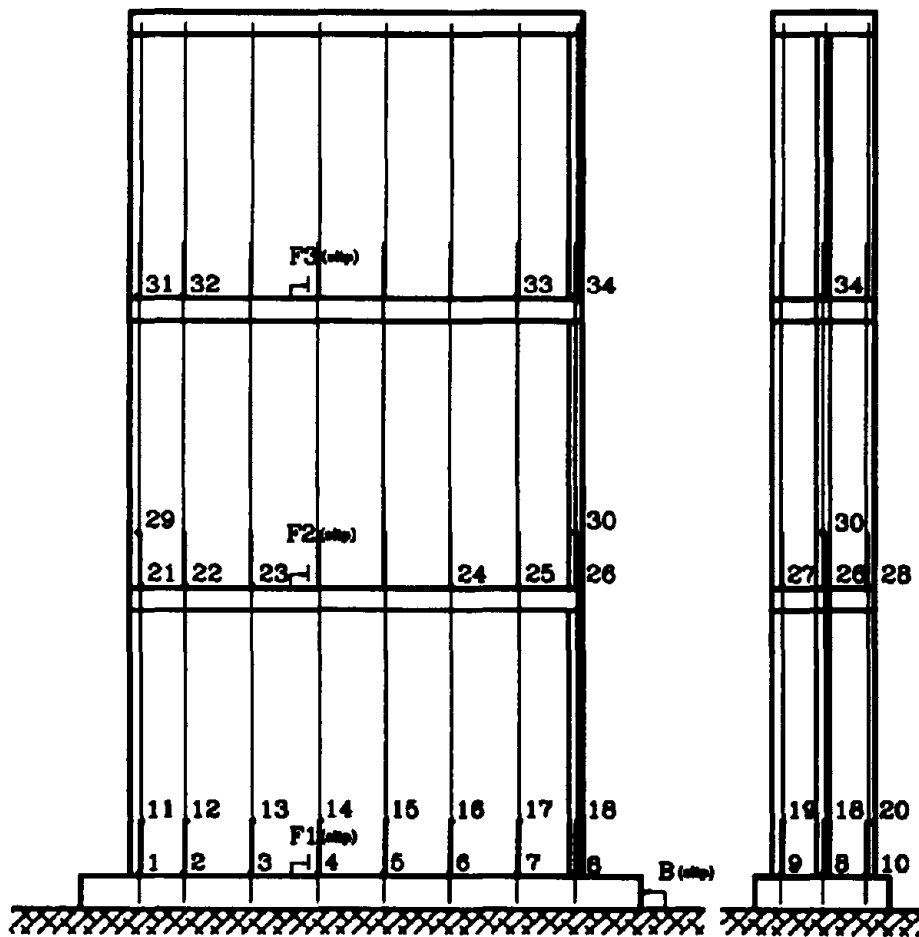


Fig. 3.5. Rebar Strain Gage and Slip Gage Locations

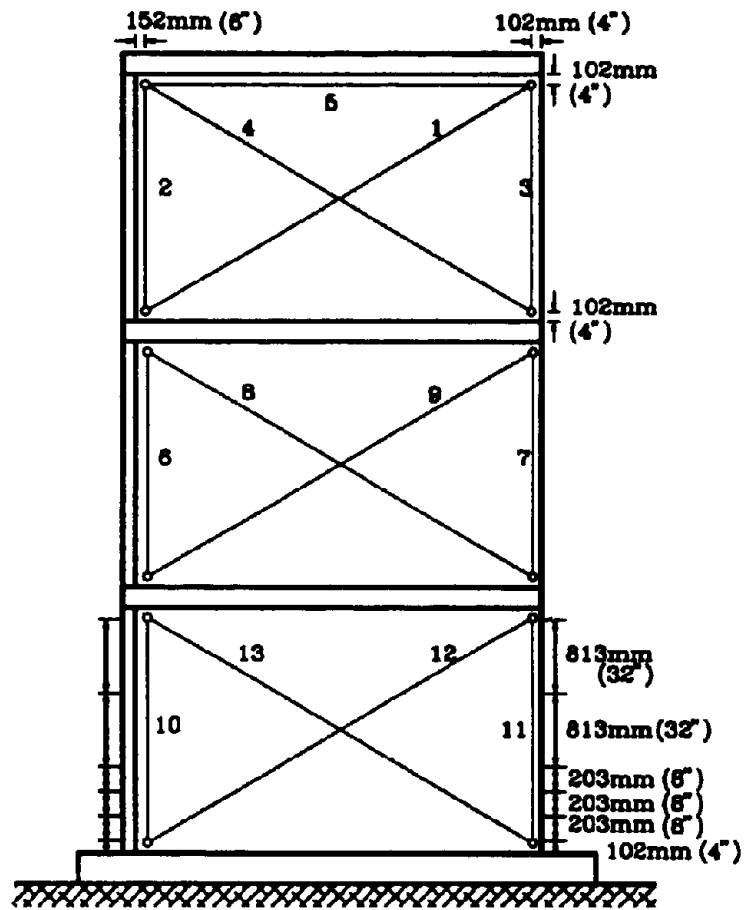


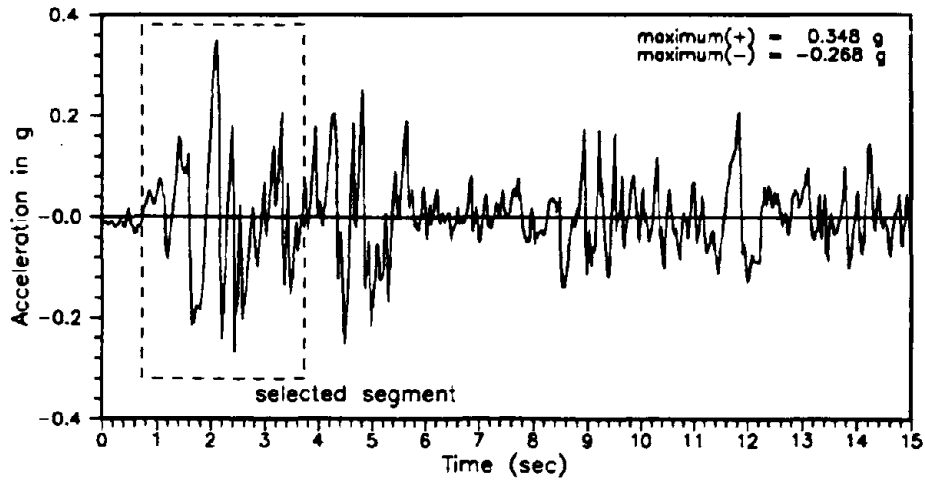
Fig. 3.6. Instrumentation of Wall Panel Deformation and Curvature

## **4. TEST DESCRIPTION**

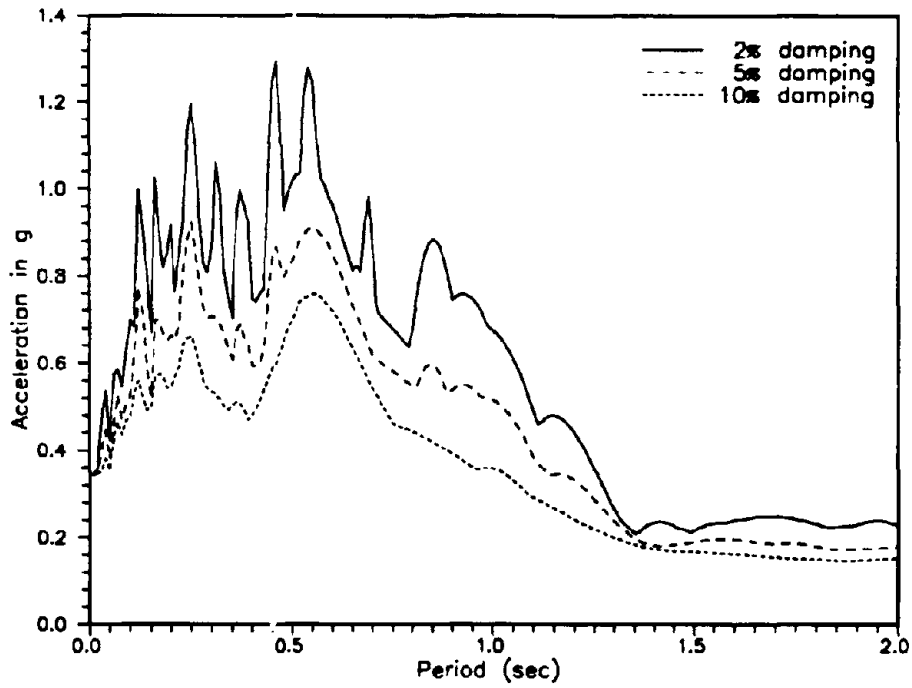
A series of GSD tests was performed with the structure and loading system described in the previous chapters. Two different input excitations were used, namely a segment of the El Centro 1940 NS component, shown in Fig.4.1, and segments of the Imperial Valley 1979, James Road 230' component, already shown in Fig.2.2. The amplitude of the record was adjusted to keep structural displacements within desired deformation limit states based on linear elastic predictions made with the measured stiffness after completing the previous loading segments. The initial tests were designed to keep the structure below first yield, later the displacement levels were increased to the yield limit state and maximum capacity limit state simulations, and finally to complete toe crushing.

### **4.1. Numerical Modeling**

The Pseudo-dynamic algorithms and parameters chosen for the present test series reflect the issues discussed in Chapter 2. The 3-story wall specimens were idealized as 3-DOF systems, with the masses lumped at the floor levels. The mass of the floors was adjusted in order to allow a the time integration interval of at least 0.005 seconds in the conditionally stable algorithms. The initial structural stiffness (see Section 4.5 for the measurement procedure) and the actual test specimen mass resulted in natural frequencies of 17.7, 63.1, and 117.5 Hz for the 3-DOF model. Considering the frequency range of the major source of energy of the earthquake input, and to provide for integration time steps of reasonable length, the analytical model was adjusted with contributory mass equal to 15 times the specimen mass, resulting in initial (uncracked) natural frequencies of 4.6, 16.3, and 30.3 Hz, which permitted the use of integration time interval of 0.005 sec.



(a) Time History



(b) Response Spectra

Fig. 4.1. El Centro 1940 NS Record

Although the Newmark Explicit method was first applied with 5% modal viscous damping, cases without numerical damping were also examined for later stages of the tests. When the Modified Newmark Explicit algorithm was used, the parameters were chosen such that larger damping effects were obtained in the higher modes, while still providing realistic damping in the first mode. For the implicit Hilber's Alpha method, a standard set of parameter values ( $\alpha=0$ ,  $\beta=0.25$  and  $\gamma=0.5$ ) were used, which leads to the constant-average-acceleration integration without numerical damping.

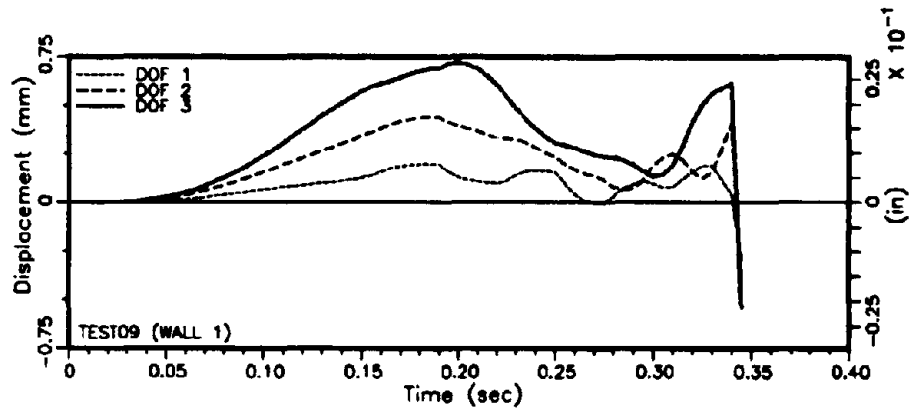
#### 4.2. GSD Test Implementation and Verification

The first 3-story shear wall specimen was used to implement and verify the proposed GSD testing procedure. The El Centro 1940 NS record and the one-second window selected for the initial series of experiments is shown in Fig.4.1. A scale factor of 0.5 was applied to the input record to keep the structural response at desired limit states.

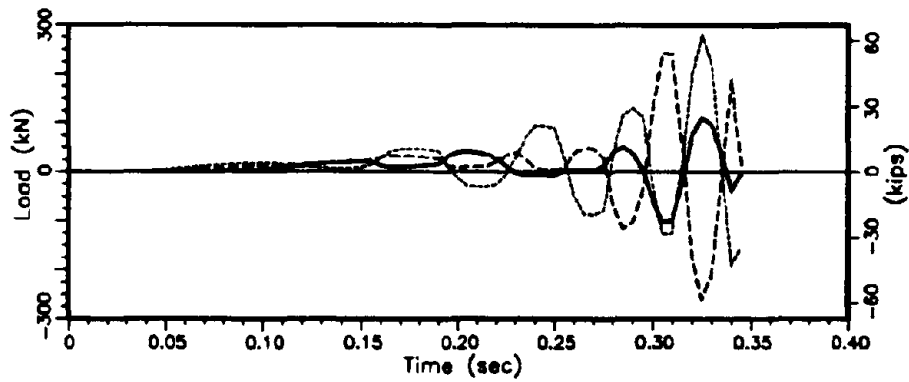
First, two experiments were performed using the Newmark Explicit time integration scheme with a time step of 0.005 sec, constant 5% modal damping, and a structural displacement error tolerance of 0.001 in.=0.0254mm. The response obtained in Test 9 is shown in Fig.4.2. Both the displacement and restoring force histories show diverging oscillatory behavior, representing the uncontrolled growth of spurious higher modes leading to unrealistic relative story shear forces in the structure, and ultimately to an instability in the loading system. This phenomenon has been observed in other MDOF pseudo dynamic tests [4]. Following these tests, the time integration algorithm was changed to the Modified Newmark Explicit scheme, having frequency proportional damping to suppress the spurious higher modes. Using the pretest measured stiffness, calculated damped natural frequencies were 3.8, 15.4, and 28.0 Hz, and the integration parameters were adjusted to give 3.4, 22.8, and 59% damping for the first three modes respectively.

The results of tests at the earliest stage, Tests 13 and 15, along with a prediction, are shown in Fig.4.3. The noteworthy features of these results are the dominance of first mode

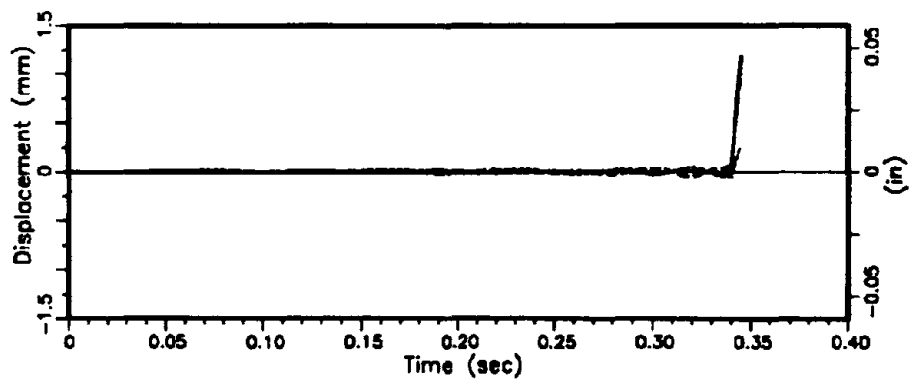




(a) Displacement Time History



(b) Restoring Force Time History



(c) Displacement Error Time History

Fig. 4.2. Failed Convergence with Newmark Explicit Method

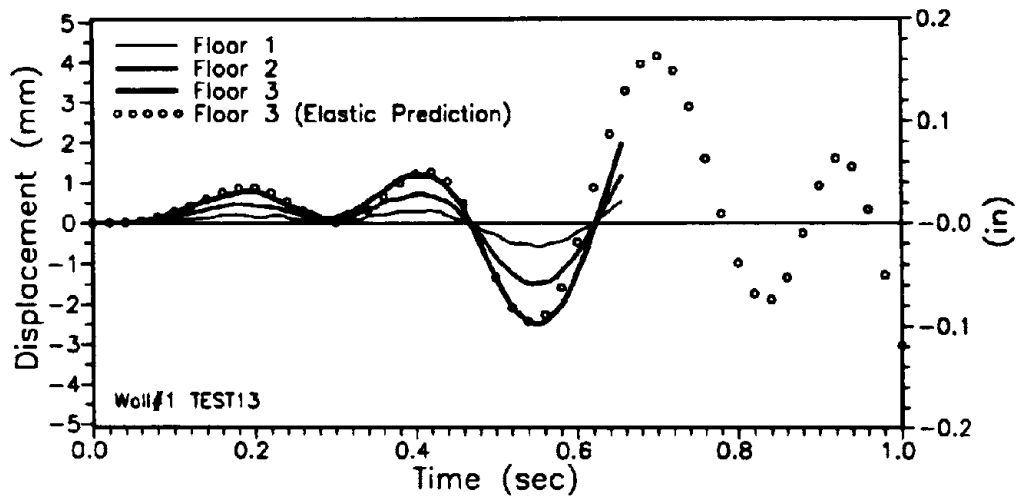
response, controlled higher modes, and the good reproducibility between the two tests. The latter feature shows stability of the structural properties at least to the end of Test 13 corresponding to top floor peak displacement of 0.1 in. with the flange in tension. The results indicate the onset of nonlinearity at about 0.45 seconds. This coincided with the first observed flexural cracking at the wall base, resulting in the expected period elongation and amplitude increase over the linear elastic prediction, see Fig.4.3.

During these tests elastomeric pad deflections resulted in actuator displacement amplifications of 3 to 5. The structural displacement errors were kept below the 0.001 in. error tolerance. Restoring force oscillations remained, despite the lack of significant higher mode displacement participation.

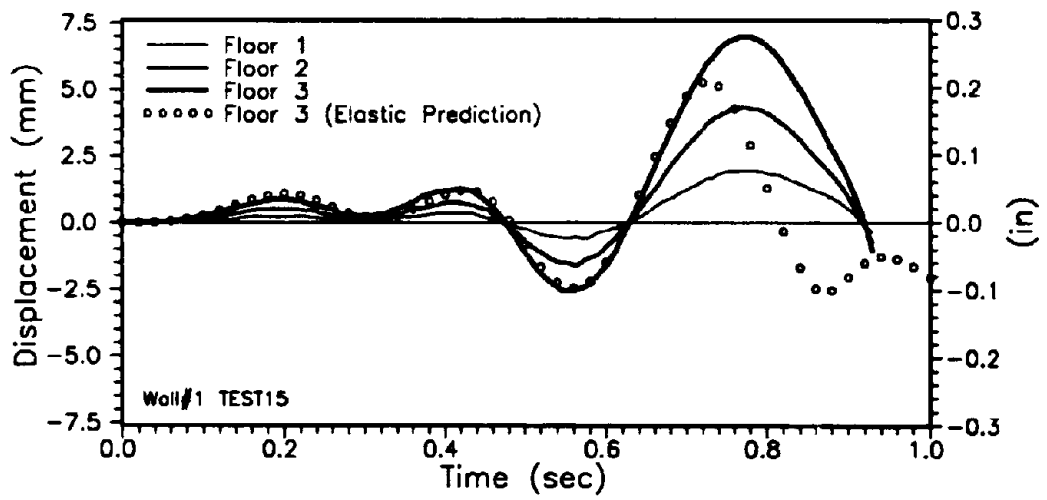
The displacement, load, and error histories for the three active DOFs of the full scale 3-story wall specimen, after a slight degradation in stiffness, are depicted in Fig.4.4. The measured stiffness resulted in natural frequencies of 3.91, 13.24, 24.2 Hz in this case. The same acceleration scale factor, integration algorithm, time step, and error limit were used as in Test 13. The response at low displacement levels still appears close to linear elastic, but deviates significantly thereafter. The load oscillations observed earlier persist, although the errors are reasonably well bounded.

Results of Test 35 on the significantly softened structure are presented in Fig.4.5. Pretest stiffness measurements gave 1.45, 8.65, and 19.81 Hz for the first three modes, a significant reduction from the undamaged values for the first two modes. The acceleration scale factor of 0.5 was retained, as were the integration algorithm, time step, and error limit. The top floor displacement reached 2 in. (50.8 mm) corresponding to a drift of 0.64%. Load oscillations with about the same frequency remain to about 0.8 sec of the response, but appear with a much lower frequency thereafter. Significant diagonal cracking and toe crushing occurred at this time.

Wall 1 tests showed that the developed GSD method can simulate seismic loads on stiff MDOF systems. It was left for investigation on the Wall 2 tests to capture higher mode effects

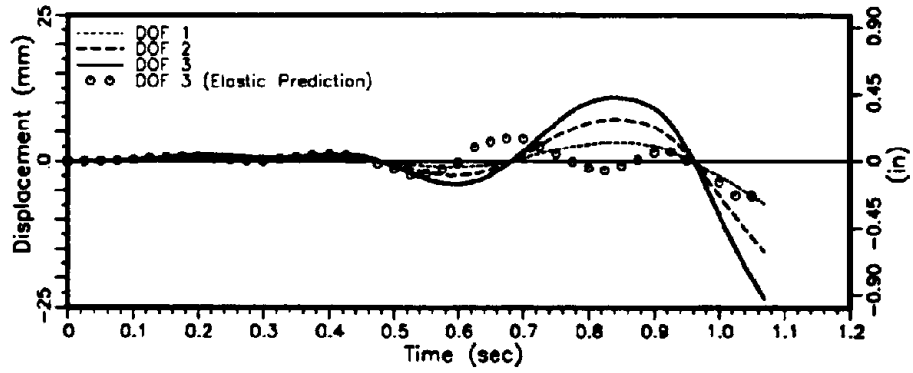


(b) Result of Test 13

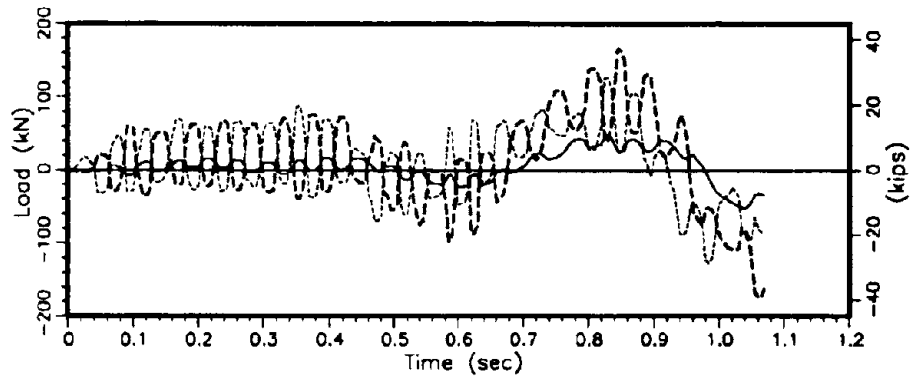


(b) Result of Test 15

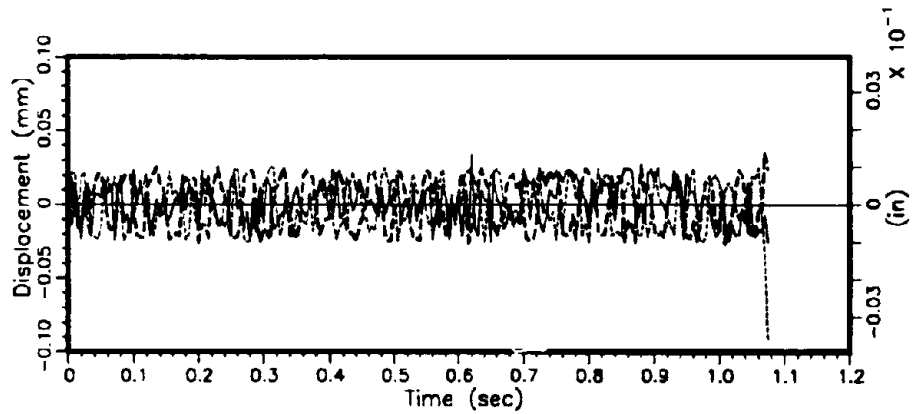
Fig. 4.3. Test Results at the Earliest Stage



(a) Displacement Time History

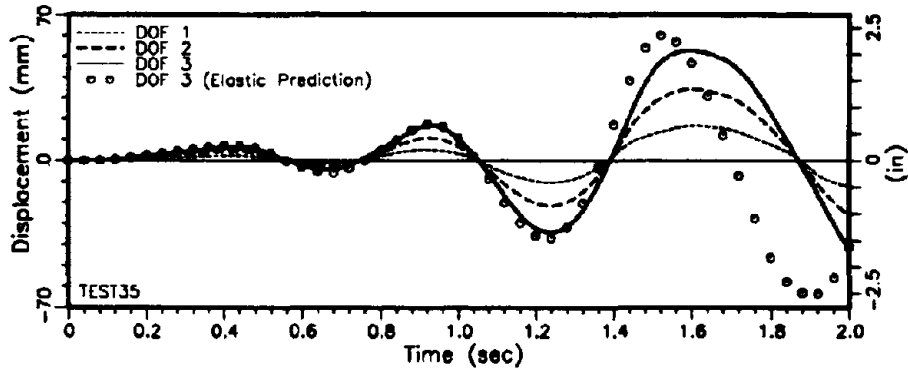


(b) Restoring Force Time History

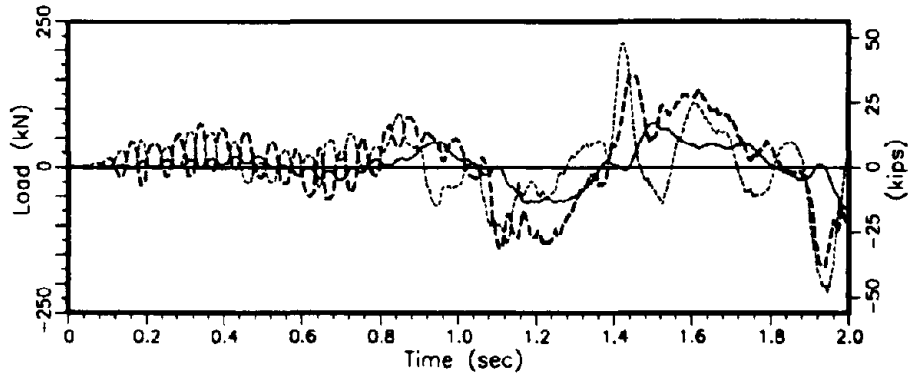


(c) Displacement Error Time History

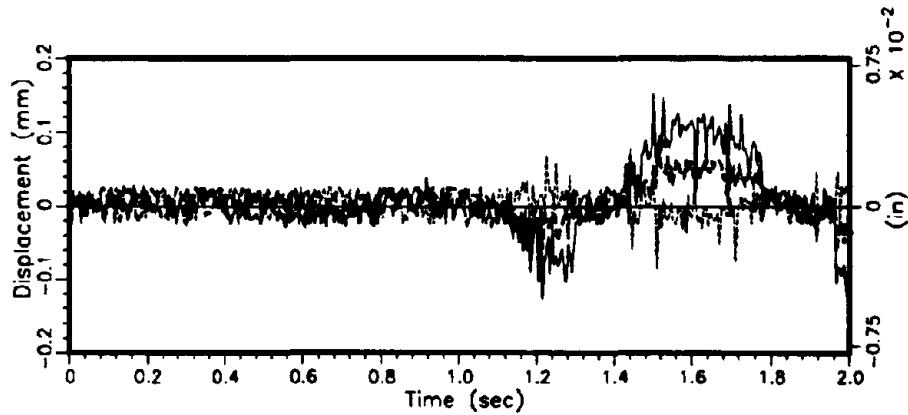
**Fig. 4.4. Result of Test 28**



(a) Displacement Time History



(b) Restoring Force Time History



(c) Displacement Error Time History

**Fig. 4.5. Result of Test 35**

and to improve the control of errors and corresponding load oscillations.

### 4.3. GSD Test Refinements

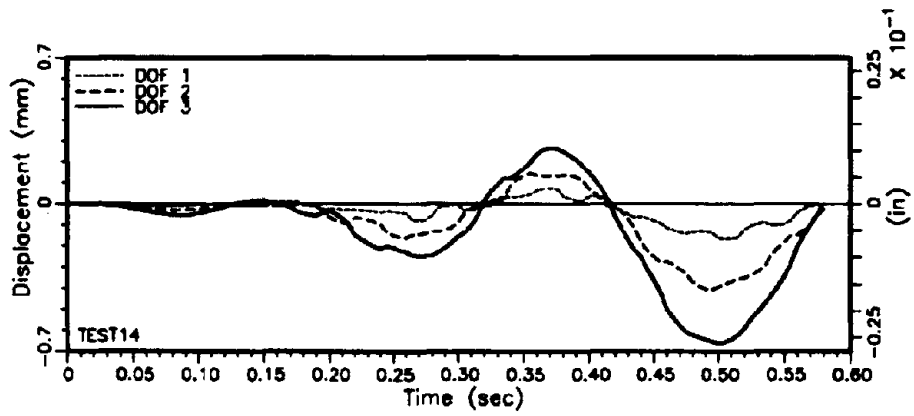
Wall specimen 2, which was the same as specimen 1 in dimensions and properties, was used to refine the GSD procedure. Several time integration schemes, such as Newmark Explicit, Modified Newmark Explicit, and the Hilber's Alpha method with initial stiffness iteration were implemented in the outer control loop for comparison. Also, a restoring force correction scheme [16] was added to the outer loop. In this correction, the difference between the calculated structural target displacement and the actual measured structural displacement is multiplied by the initial structural stiffness (measured experimentally at the beginning of the test segment), yielding a restoring force correction which is added to the measured restoring force in the subsequent outer loop calculation of the next target displacement.

Specifically, at time step  $i$ , the outer loop calculation of the next target displacement  $x_{target}(i+1)$  used a "corrected" restoring force

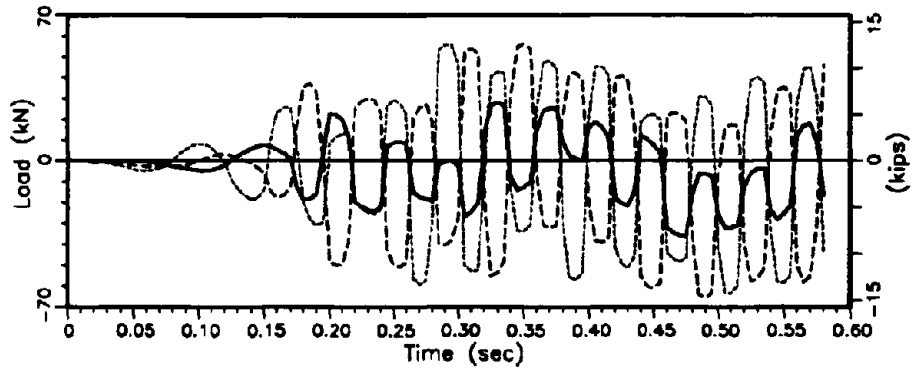
$$\bar{r}(i) = r(i) + \hat{K}_0(x_{target}(i) - \hat{x}(i)) \quad (4.1)$$

instead of the measured restoring force  $r(i)$ . In eqn.(4.1),  $\hat{K}_0$  is the initial structural stiffness measured experimentally at the beginning of the test segments. Since the restoring force errors result in spurious higher mode effects, a correction to the restoring forces reduces spurious higher mode effects and allows for smoother structural response.

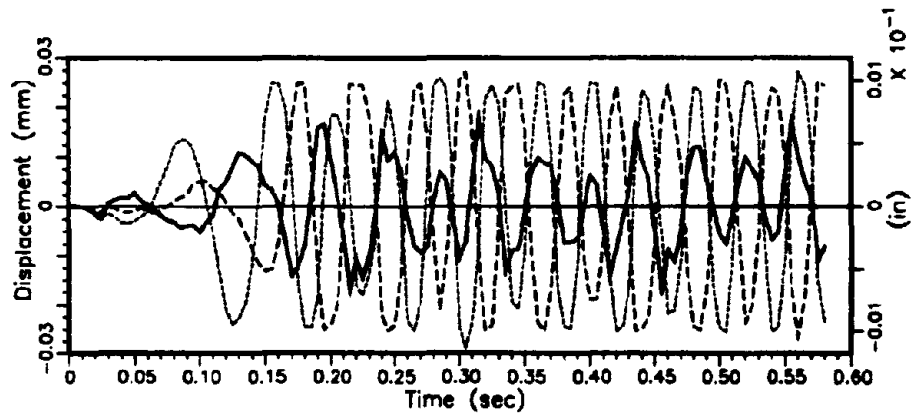
Figures 4.6 and 4.7 show the effect of the correction scheme described above. In both of the test, the same input acceleration and same integration scheme (Modified Newmark Explicit method) were used. Figure 4.6, without the correction, shows the kind of load oscillation observed in the Wall 1 verification tests. On the other hand, the results in Fig.4.7, which reflect the effect of the restoring force correction, indicate that the load oscillation is largely suppressed, with a significant reduction in the displacement error.



(a) Displacement Time History

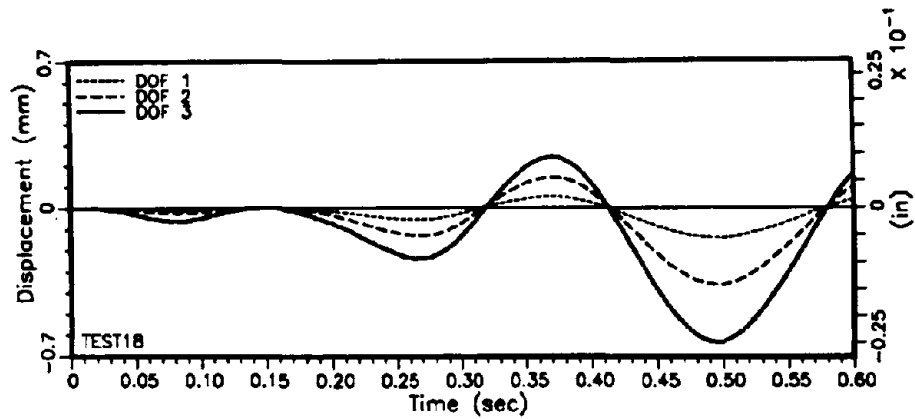


(b) Restoring Force Time History

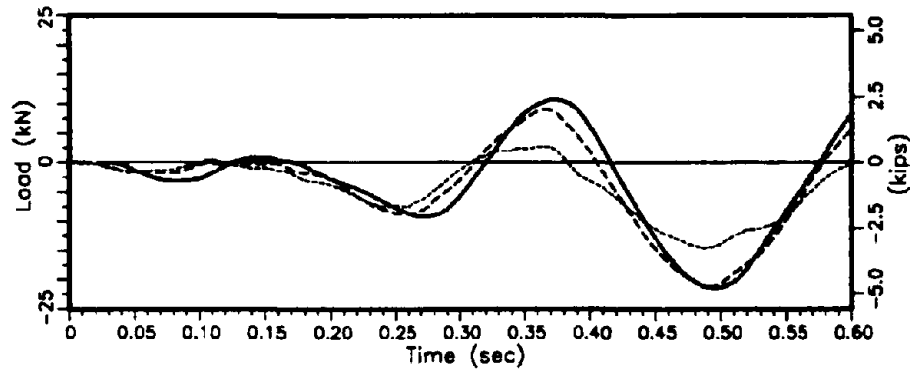


(c) Displacement Error Time History

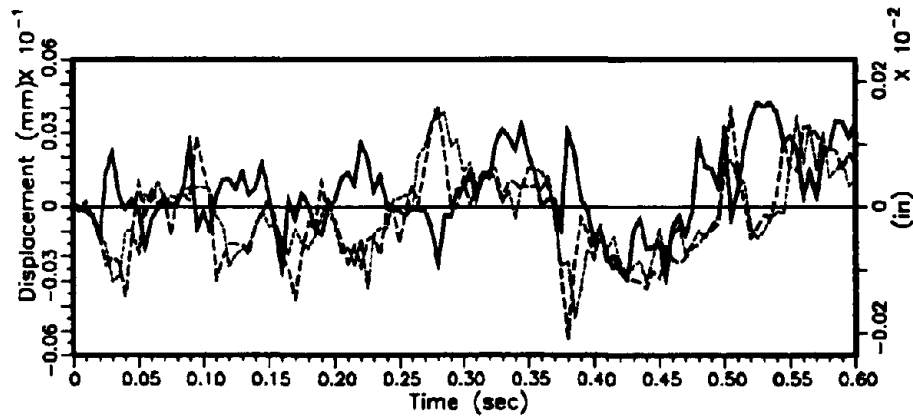
Fig. 4.6. Test Result without Restoring Force Correction



(a) Displacement Time History



(b) Restoring Force Time History



(c) Displacement Error Time History

Fig. 4.7. Test Result with Restoring Force Correction



After confirming the effectiveness of the correction scheme, it was used in the following sequence of tests on the 3-story wall, summarized in Table 4.1. The table shows, in addition to the acceleration window, the integration scheme and the scale factor, and also the change in the three natural response periods for the masonry wall prior to the associated test, as well as overall test speed information.

Three analytical models were used, as mentioned above, in analyzing the outer loop target story displacements, namely the Newmark Explicit (NE), the Modified Newmark Explicit (MNE) and the implicit Hilber's Alpha (HA) methods. The implicit scheme (HA) allowed constant damping for all modes without artificially suppressing higher mode effects. With the restoring force correction, even the NE method showed stable results and was successfully implemented without any artificial numerical damping, thus capturing all possible higher mode effects. Thus, for the second wall, the restoring force correction was applied to all integration schemes shown in Table 4.1.

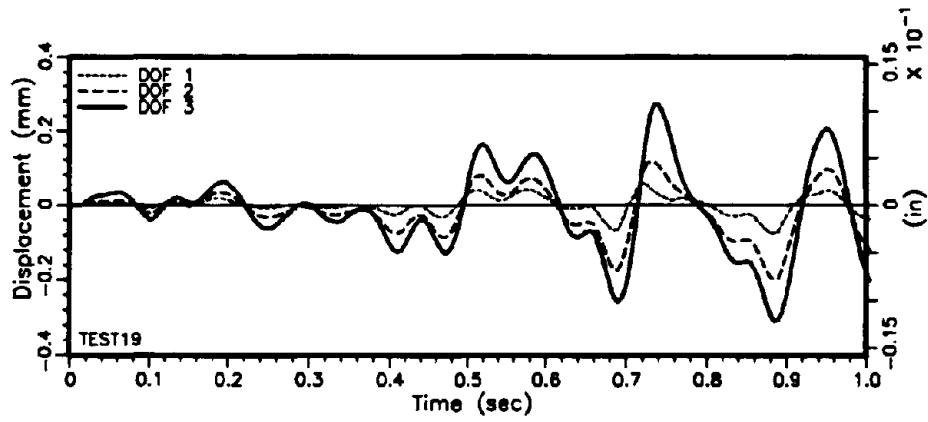
The computer-controlled inner loop was modified with two special features to improve testing speed. First, the actuator displacement amplification factor was applied to the difference between the target and the measured structural displacements to account for the elastomeric loading pad amplifications and for opposite direction displacements in higher mode response. Second, since the command signal and the actuator displacement relationship may be off-bias and not completely linear, the new displacement increment for individual actuator movement is added to the previous command signal rather than to the measured actuator displacement, thus reducing the flip-flop phenomena in the inner control loop convergence.

The pre-yield phase was used to compare the effect of the different time integration schemes, e.g., Tests 19, 20 and 21 in Table 4.1. Response time-histories for the three tests are depicted in Figs. 4.8, 4.9 and 4.10. As can be seen, Test 19, the MNE scheme (Fig.4.8) results in a first mode response, since all higher mode effects are numerically damped out. Some higher mode effects were captured with the HA method (Test 20), with 5% damping per mode. The

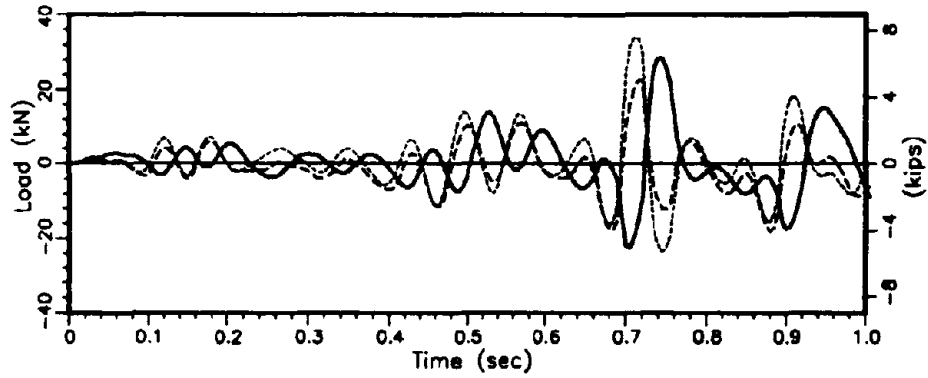
Table 4.1 Representative GSD Tests on Three-Story Wall Specimen No.2

TEST number	integration scheme	accl. window	scale factor	damping $\zeta_1/\zeta_2/\zeta_3$ (%)	Test Length (sec)	Time (sec)	Test speed ratio	Natural Period $T_1/T_2/T_3$ (sec)	maximum top displacement push/pull (mm)
TEST 19	MNE	2	0.5	6.7/27/72	1.0	2575	2575	0.23/0.064/0.035	0.271/ -0.067
TEST 20	HA	2	0.5	5/5/5	1.0	9225	9225	0.23/0.061/0.034	0.300/ -0.376
TEST 21	NE	2	0.5	-	1.0	4289	4289	0.23/0.061/0.034	0.366/ -0.452
TEST 31	MNE	2	6.0	6.7/24/58	0.74	7856	10616	0.23/0.070/0.038	3.752/ -1.952
TEST 44	NE	3	2.5	-	0.92	11046	12007	0.29/0.087/0.046	3.878/ -7.684
TEST 48	NE	4	0.25	-	1.66	7622	4592	0.30/0.094/0.050	10.045/ -5.401
TEST 56	NE	6	0.3	-	1.64	9055	5521	0.42/0.122/0.055	31.688/ -11.424
TEST 60	NE	7	1.5	-	0.75	4790	6387	0.38/0.139/0.059	35.458/ -35.141
TEST 65	NE	8	-0.6	-	1.82	5745	3157	0.85/0.174/0.060	28.902/ -56.667
TEST 66	NE	8	0.9	-	0.40	1405	3513	0.85/0.174/0.060	102.308/ -0.036
TEST 67	NE	8	-0.9	-	0.39	1570	4025	0.85/0.174/0.060	0.0356/ -100.83

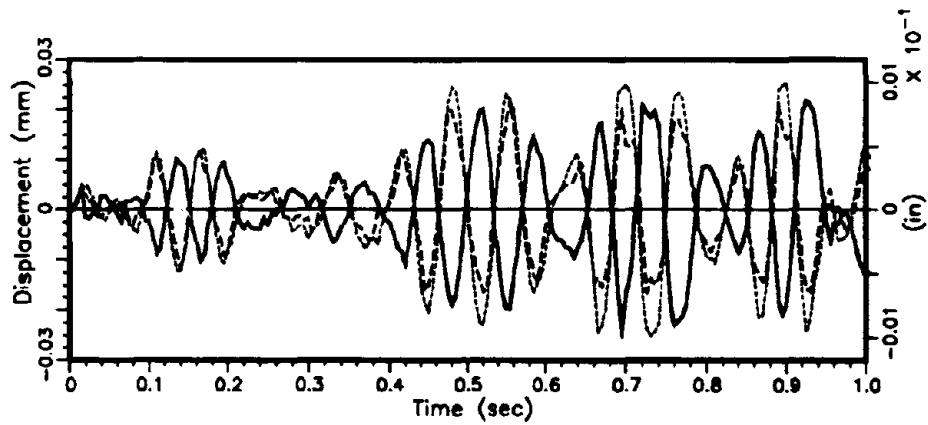
- \* MNE : Modified Newmark Explicit method
- HA : Hilber's Alpha method (implicit)
- NE : Newmark Explicit method



(a) Displacement Time History

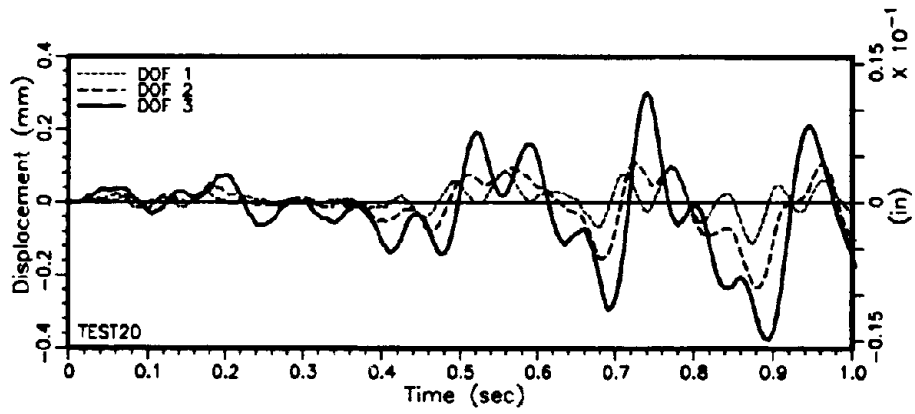


(b) Restoring Force Time History

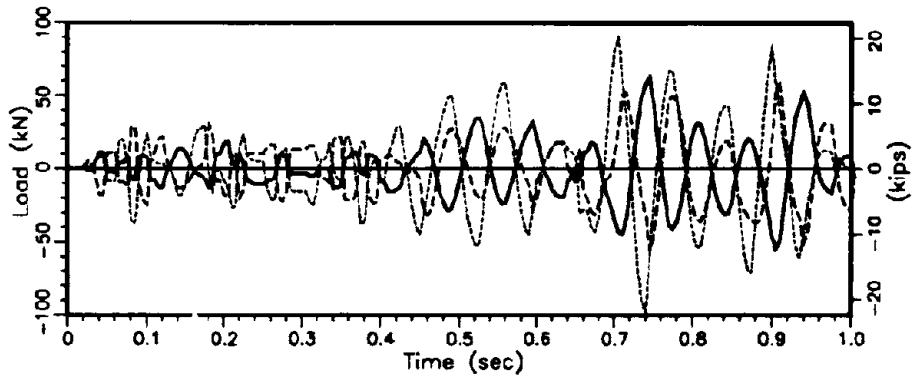


(c) Displacement Error Time History

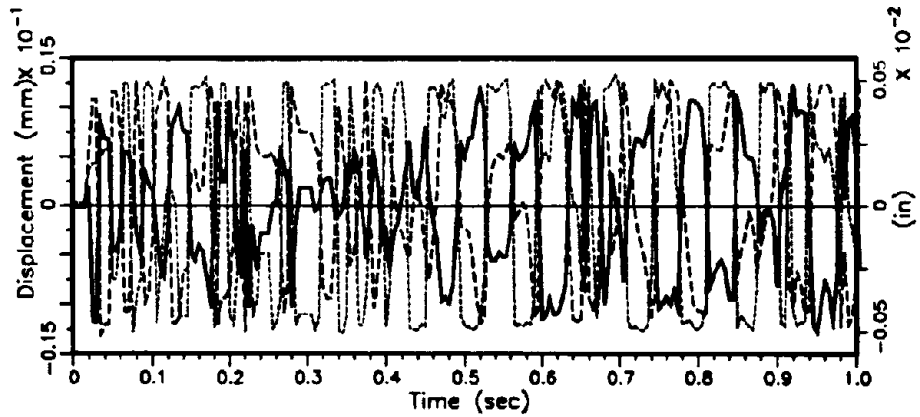
**Fig. 4.8. Result using Modified Newmark Method**



(a) Displacement Time History

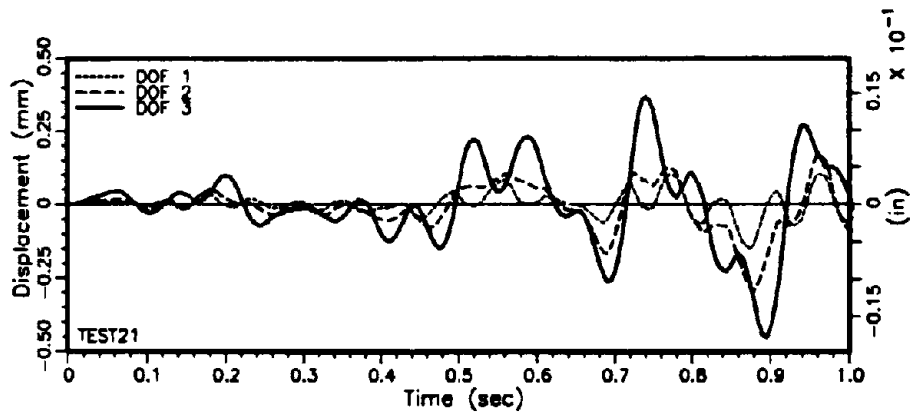


(b) Restoring Force Time History

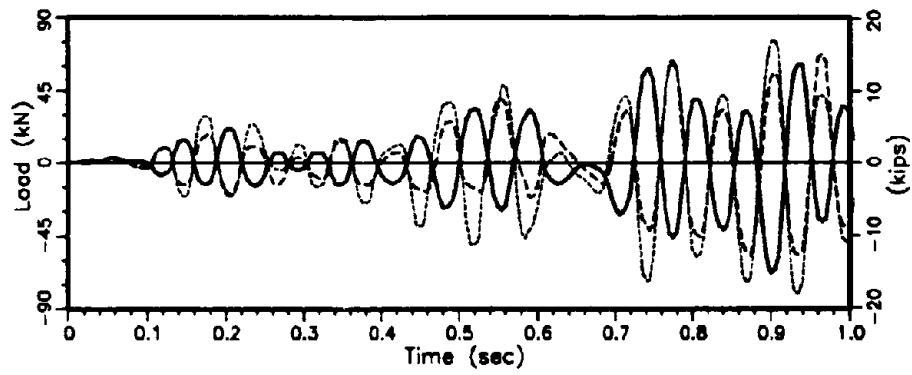


(c) Displacement Error Time History

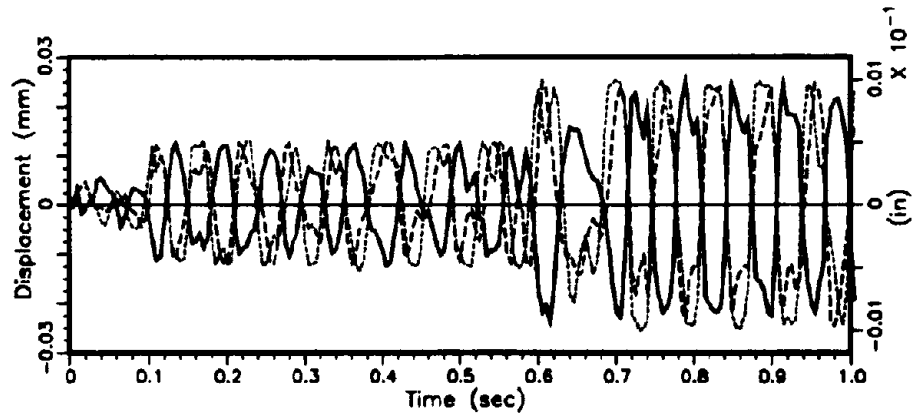
Fig. 4.9. Result using Hilber's Alpha Method



(a) Displacement Time History



(b) Restoring Force Time History



(c) Displacement Error Time History

Fig. 4.10. Result using Newmark Explicit Method

higher mode response is visible in Fig.4.9 in the displacement time-history and in the increased restoring forces. Finally, the NE scheme, without any numerical damping, featured the largest second mode contributions, as can be seen in Fig.4.10. The displacement error can be tightly controlled by specified error tolerances (note the three different levels in Fig.4.10c), where the error tolerance was adjusted in three steps.

The above discussed modifications to conventional on-line testing techniques have allowed the testing of stiff masonry wall systems with GSD using reliable integration schemes such as NE without introducing artificial numerical damping and resulted in pseudo-dynamic test rates of one to four thousand times the real seismic event, or in test durations of typically less than one hour per one second of earthquake time-history, see Table 4.1.

In the tests at the later stage, the Newmark Explicit method was mainly used, up to final toe crushing of wall specimen 2.

#### **4.4. Inverse Triangular and Uniform Loading Tests**

Since design criteria for buildings in seismic zones are often compared with the hysteretic load-displacement envelopes for specified load distribution patterns, the second 3-story wall specimen was subjected to uniform and inverse triangular loading patterns following each GSD segment and loaded to the previously obtained maximum building drift level. Results from these fixed load distribution patterns are discussed in Chapter 5.

#### **4.5. Stiffness Measurement Test**

As mentioned in Chapter 2, the natural frequencies of the test structure are the most fundamental parameter to carry out the GSD test procedure, since the stability of the numerical integration scheme is determined by the natural frequencies. The stiffness matrix provides not only this vital information, but also a good measure of the damage state of the test structure during the GSD test sequence. For this reason, stiffness matrix measurements by means of static loading tests

were performed prior to the GSD tests.

Since the 3-story wall is modeled as 3-DOF discrete system, the dimension of its stiffness matrix is  $3 \times 3$ . The measurement procedure is as follows. A specified small displacement is imposed to one of the floors while fixing the other floors using the loading system, and the loads are measured for all the floor levels. By performing this loading at each floor level, 3 sets of the measured displacement vector and the measured restoring force vector are obtained. These measured displacement vectors and the measured restoring force vectors are arranged columnwise in a measured displacement matrix  $\hat{\mathbf{X}}$  (dimension  $3 \times 3$ ) and a measured restoring force matrix  $\hat{\mathbf{R}}$  (dimension  $3 \times 3$ ), respectively. In principle, the stiffness matrix  $\hat{\mathbf{K}}_0$  can then be obtained by calculating

$$\hat{\mathbf{K}}_0 = \hat{\mathbf{R}} \hat{\mathbf{X}}^{-1} \quad (4.2)$$

The small applied displacement is typically chosen to be  $\pm 0.005 \text{ in.} = 0.127 \text{ mm}$  in the push or pull direction. However, the value of the stiffness matrix given by eqn. (4.2) depends on the direction of the imposed displacement, since the behavior of the 3-story wall in the push direction and in the pull direction is slightly different. For the appropriate representation of the behavior of the wall during the GSD tests in which the wall moves in both directions, the stiffness measurements are individually done in both, the pushing and pulling directions. The average of these two matrices is interpreted as the overall or average stiffness matrix. Furthermore, the symmetric part of the matrix is extracted by taking the average of the matrix and its transpose, since a symmetric stiffness matrix is theoretically correct and convenient for the computations. The result of this procedure is used as the measured stiffness matrix of the 3-story wall.

Table 4.2 shows the representative result of the stiffness measurement tests for the second 3-story wall specimen. Because the stiffness matrix measurement was performed prior to the GSD tests, the data shown in the table describes the characteristics of the 3-story wall at the beginning of each GSD test. The main diagonal stiffness values and the natural frequencies were observed to decrease as the test sequence proceeded, clearly indicating the accumulated damage and the

Table 4.2. Result of Representative Stiffness Measurement Tests

Test No.	Corresponding GSD Test	Measured Stiffness Matrix (kN/mm)	Natural Frequencies*, 1st, 2nd and 3rd Modes (Hz)
16	Test 17, Test 18, Test 19	1869.0   -952.4   194.2 -952.4   1289.4   -533.3 194.2   -533.3   318.7	4.26, 15.74, 28.37
34	Test 35	1302.0   -665.7   140.9 -665.7   855.1   -341.0 140.9   -341.0   198.3	3.52, 12.53, 23.53
43	Test 44	1047.9   -572.1   120.5 -572.1   758.1   -298.1 120.5   -298.1   176.5	3.46, 11.44, 21.61
47	Test 48	1014.0   -483.4   94.8 -483.4   585.2   -224.0 94.8   -224.0   137.1	3.35, 10.62, 20.19
55	Test 56	612.5   -425.3   132.2 -425.3   536.1   -242.7 132.2   -242.7   146.0	2.40, 8.23, 18.14
59	Test 60	497.2   -378.3   125.1 -378.3   501.1   -216.9 125.1   -216.9   131.9	2.61, 7.19, 17.06
63	Test 65 (Test 66, Test 67)	366.4   -363.9   139.6 -363.9   489.5   -240.0 139.6   -240.0   140.6	1.18, 5.74, 16.7

\* Assumed Mass = 0.08586 kN-sec<sup>2</sup>/mm (1st & 2nd DOF), 0.05687 kN-sec<sup>2</sup>/mm (3rd DOF)



**stiffness deterioration of the structure.**

## **5. BEHAVIOR OF THREE-STORY WALLS**

In this Chapter, the behavior of the second 3-story shear wall for several representative GSD and subsequent Inverse Triangular Loading and Uniform Loading tests is described.

### **5.1. Global Structural Displacement Response**

#### **5.1.1. Time History**

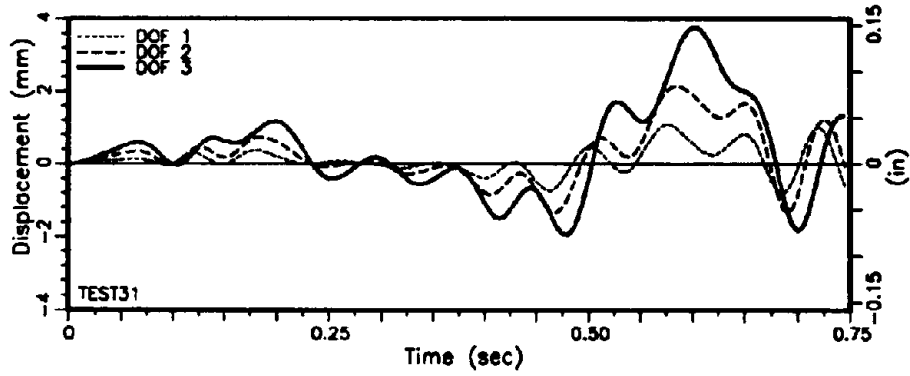
Floor displacements, floor loads and displacement error time histories are shown in Figs. 5.1 through 5.8. Test 31, Test 44 and Test 48 have some higher mode response. In summary, the GSD method allowed the testing of stiff three-story walls for selected displacement time histories without artificially eliminating higher mode effects.

#### **5.1.2. Moment and Base Shear vs. Displacement Hysteresis**

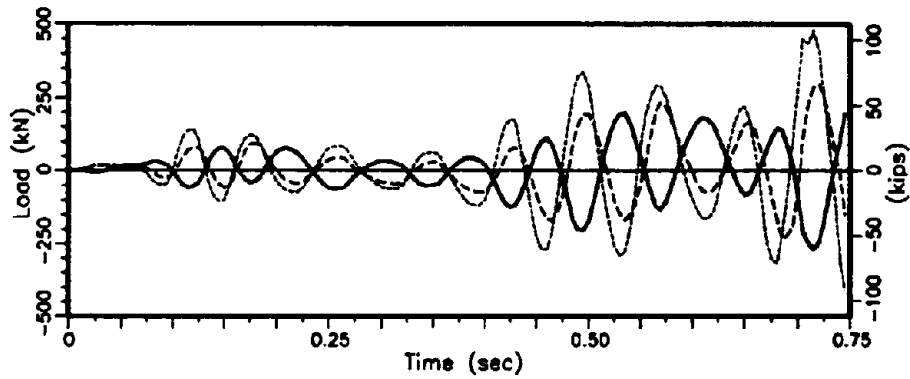
Two types of hysteresis loop plots, namely base shear vs. top displacement and base moment vs. top displacement are shown from Figs. 5.9 to 5.16. When structural response is dominated by 1st mode, (later stage of Test48, Test56, Test 60 and Test 65), nonlinear hysteretic behavior, especially stiffness degradation is revealed. In the final tests (Test 66 and Test 67), structural failure is clearly visible. When the structure is excited with higher modes (Test 31, Test 44, earlier stage of Test 48), these plots do not provide readily useful information.

#### **5.1.3. Inverse Triangular Loading Tests and Filtered Data**

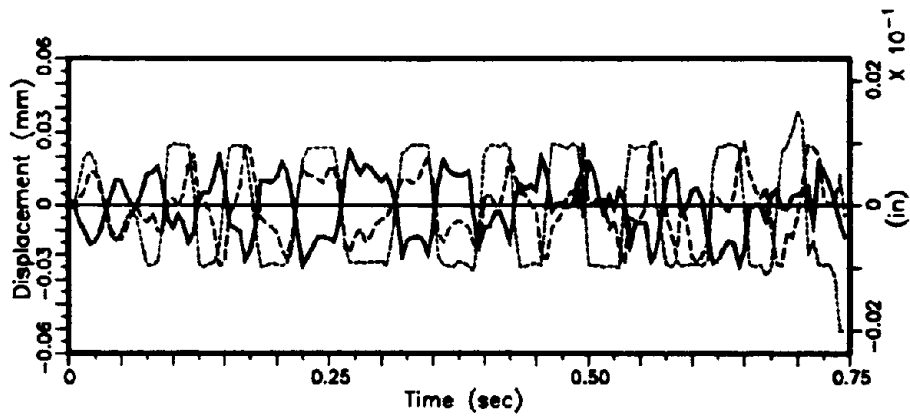
Results of fixed load pattern tests (Inverse Triangular Loading and Uniform Loading tests) are depicted in Fig. 5.17. Since pseudo-dynamic shear wall tests result in constantly changing moment and shear ratios, additional filtering is needed to correlate pseudo-dynamic test data with



(a) Displacement Time History

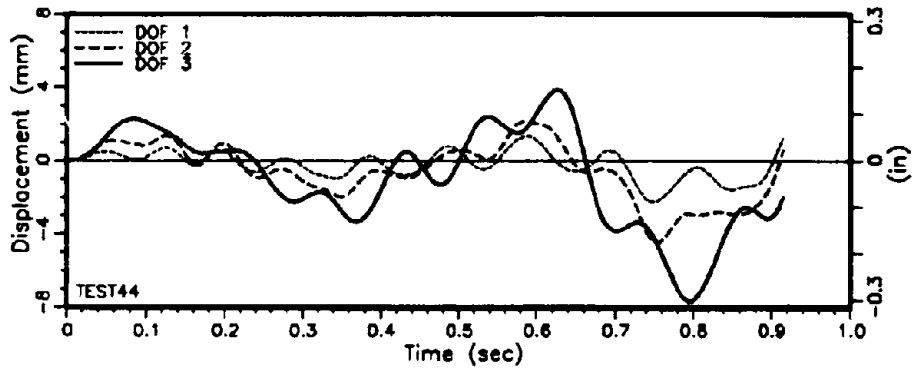


(b) Restoring Force Time History

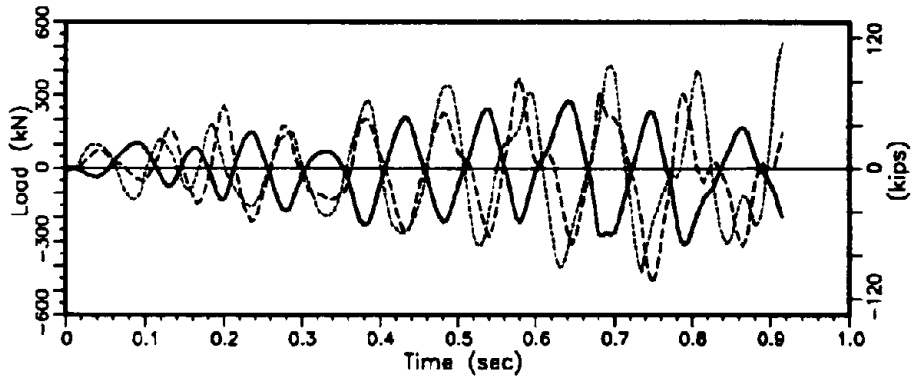


(c) Displacement Error Time History

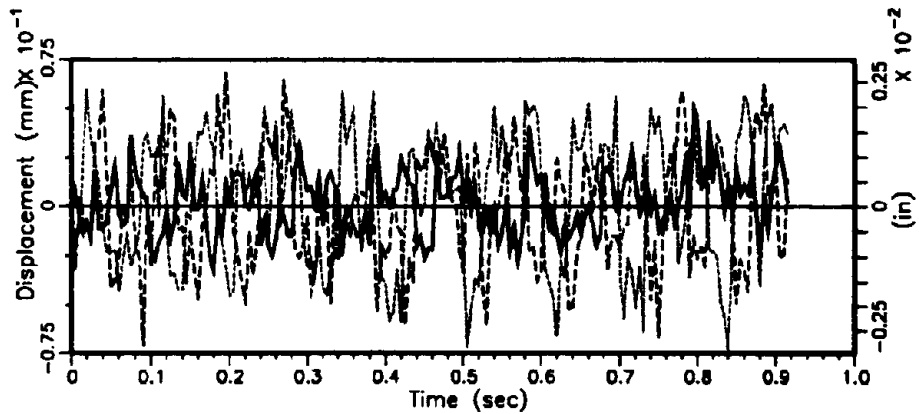
Fig. 5.1. Time Histories, Test 31



(a) Displacement Time History

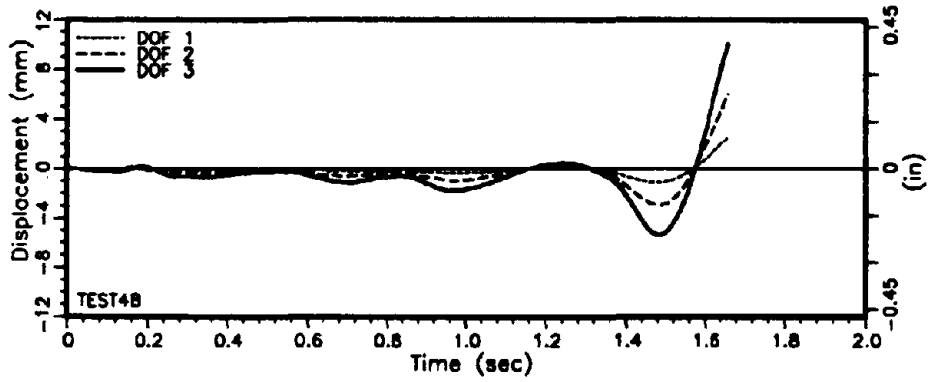


(b) Restoring Force Time History

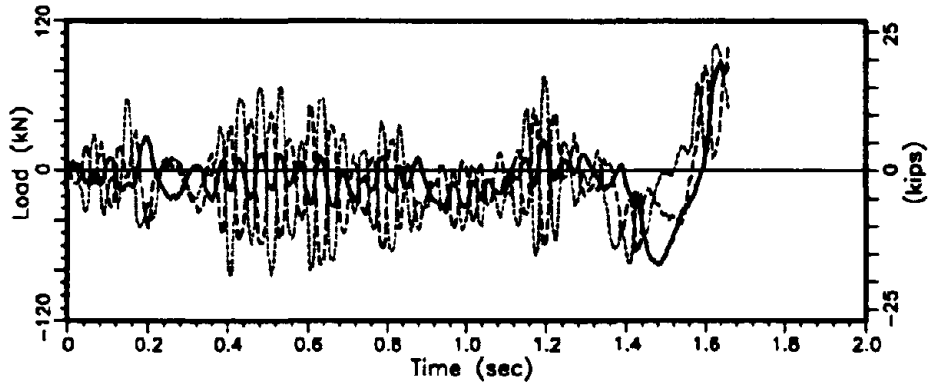


(c) Displacement Error Time History

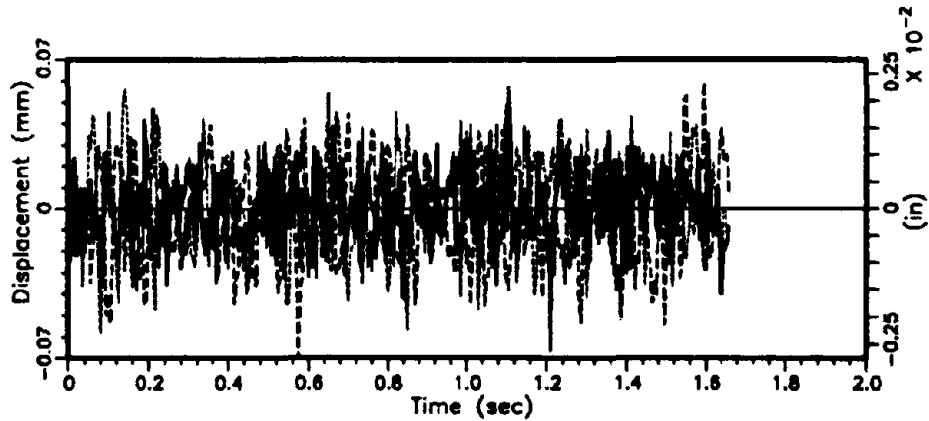
Fig. 5.2. Time Histories, Test 44



(a) Displacement Time History

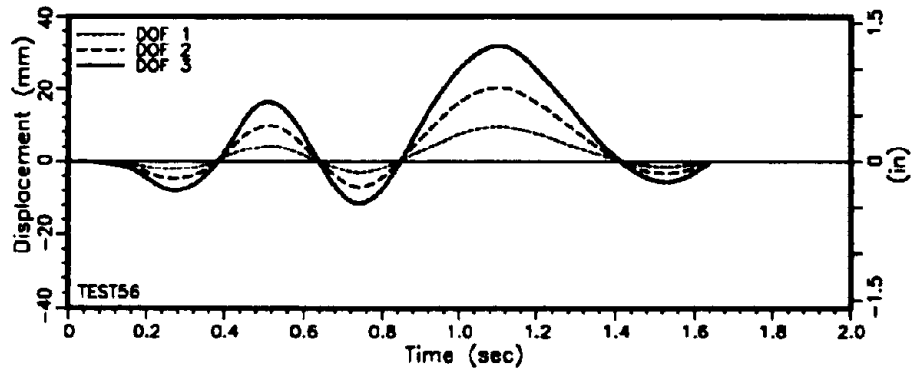


(b) Restoring Force Time History

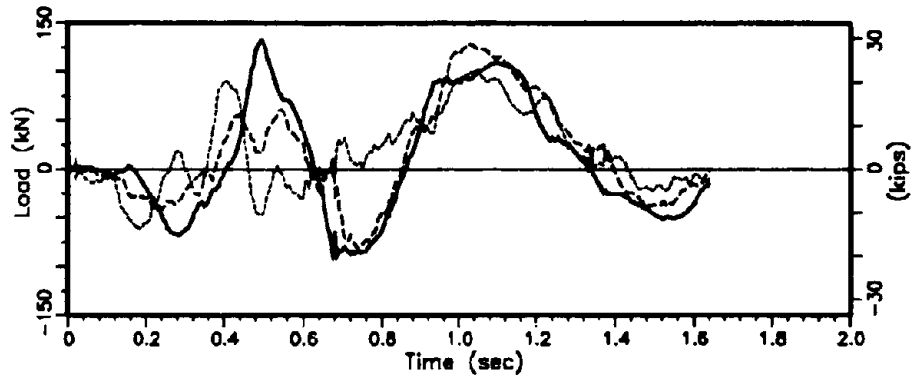


(c) Displacement Error Time History

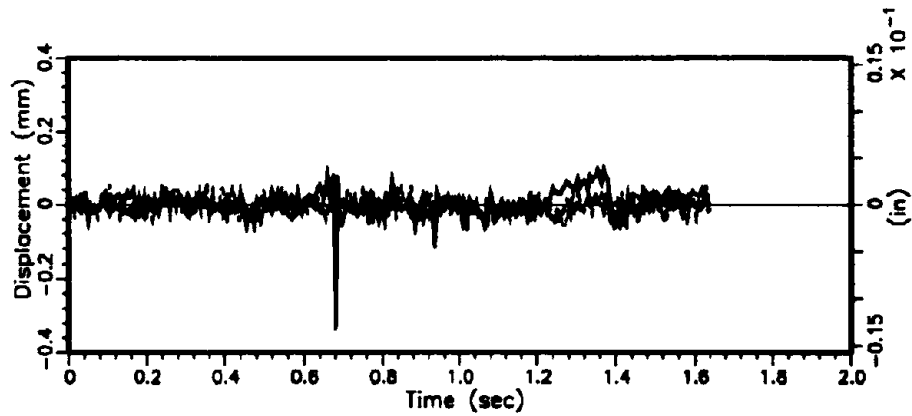
Fig. 5.3. Time Histories, Test 48



(a) Displacement Time History

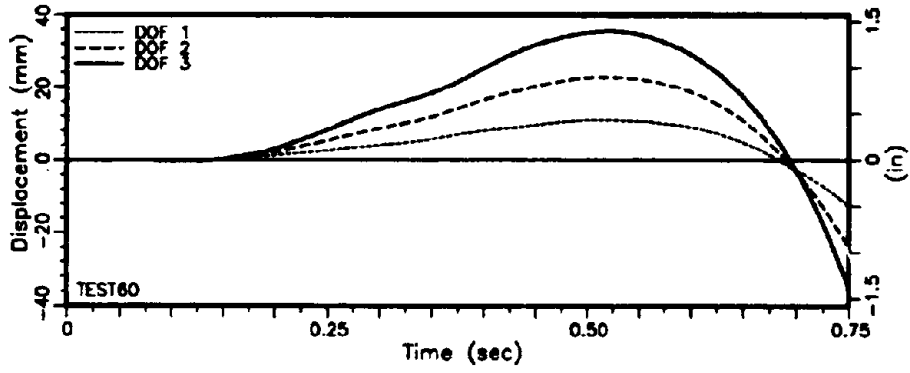


(b) Restoring Force Time History

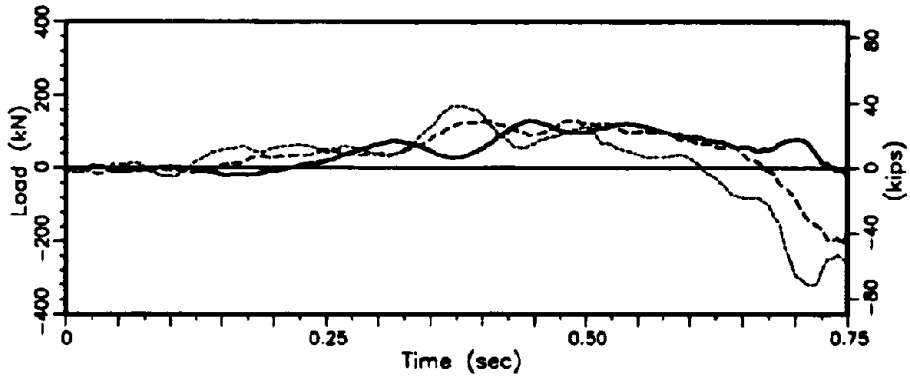


(c) Displacement Error Time History

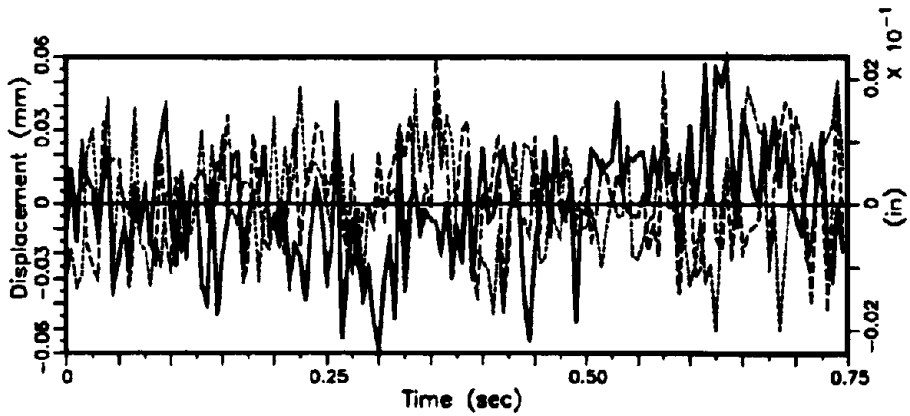
Fig. 5.4. Time Histories, Test 56



(a) Displacement Time History

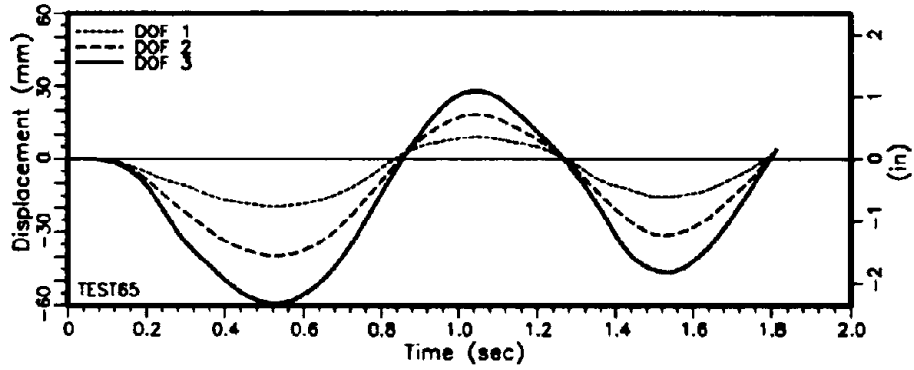


(b) Restoring Force Time History

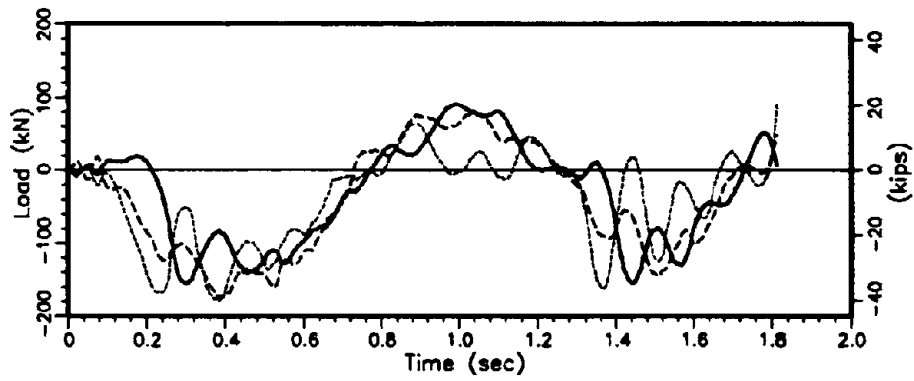


(c) Displacement Error Time History

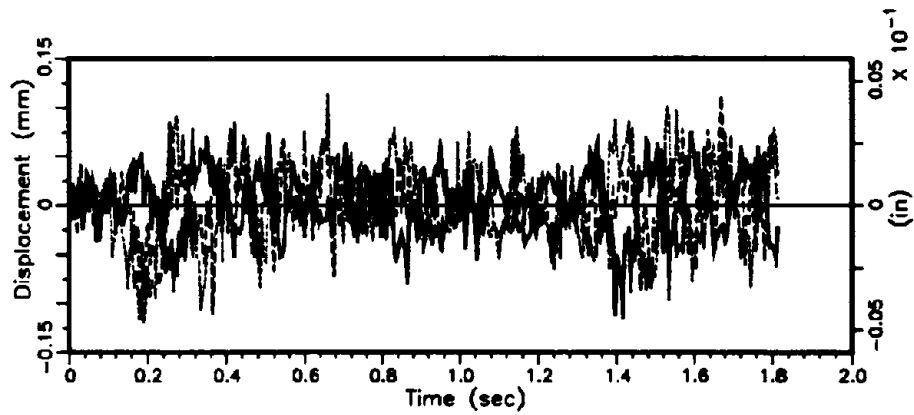
Fig. 5.5. Time Histories, Test 60



(a) Displacement Time History



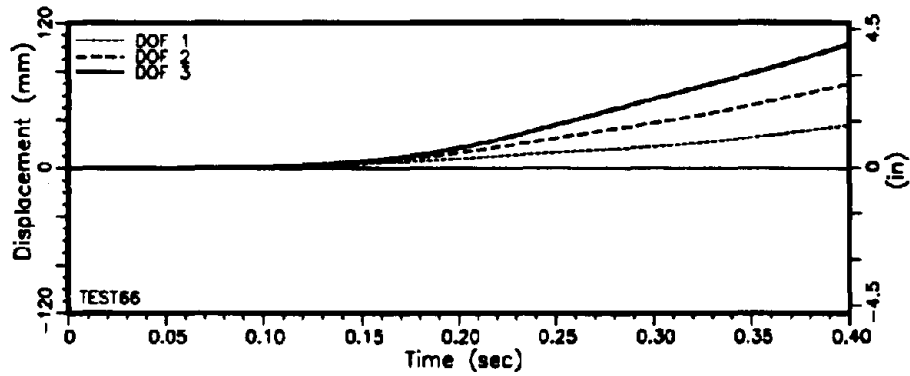
(b) Restoring Force Time History



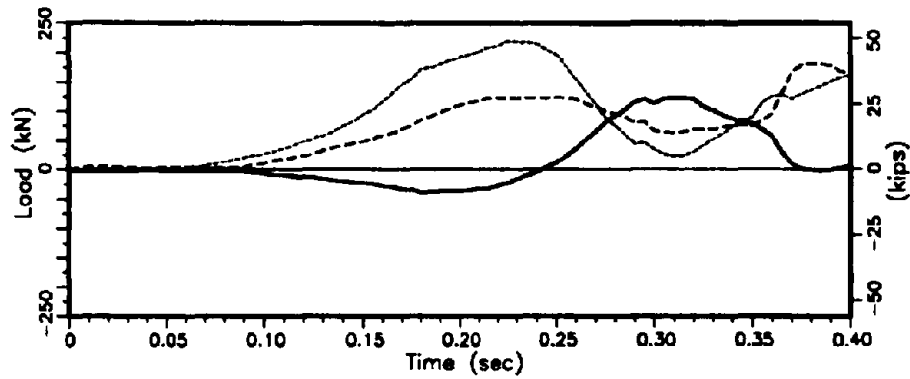
(c) Displacement Error Time History

Fig. 5.6. Time Histories, Test 65

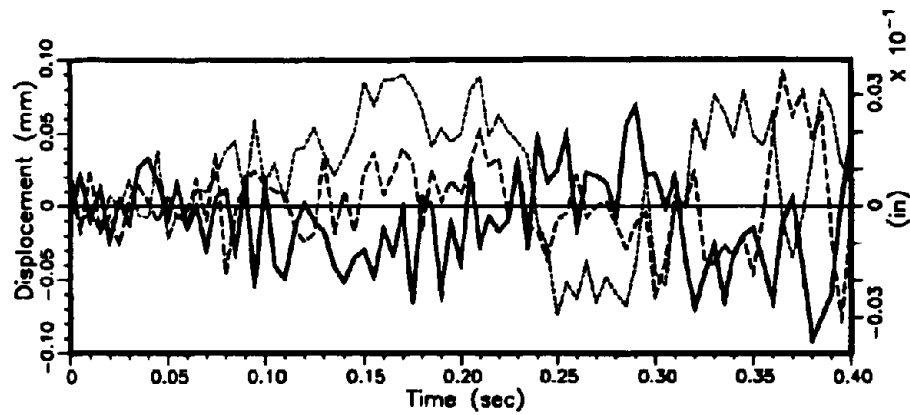




(a) Displacement Time History

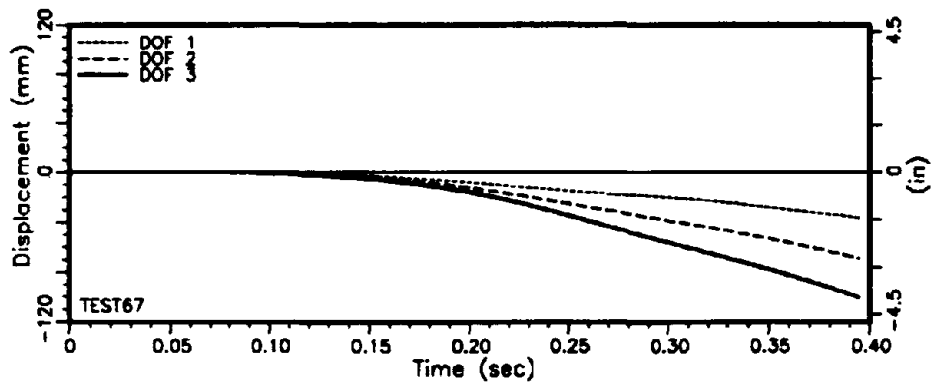


(b) Restoring Force Time History

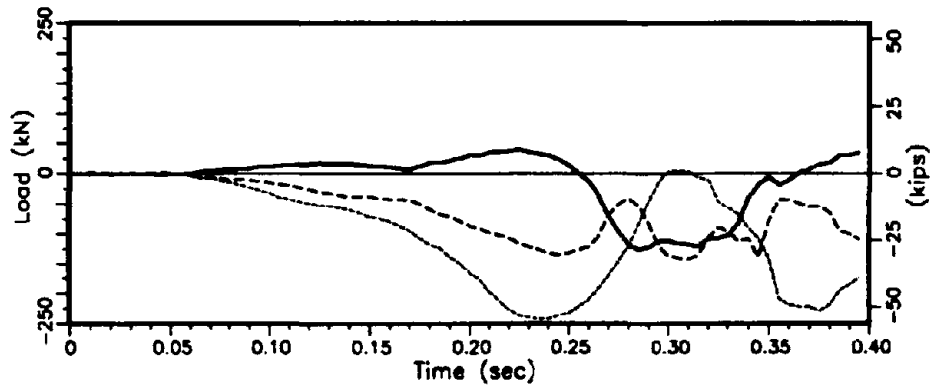


(c) Displacement Error Time History

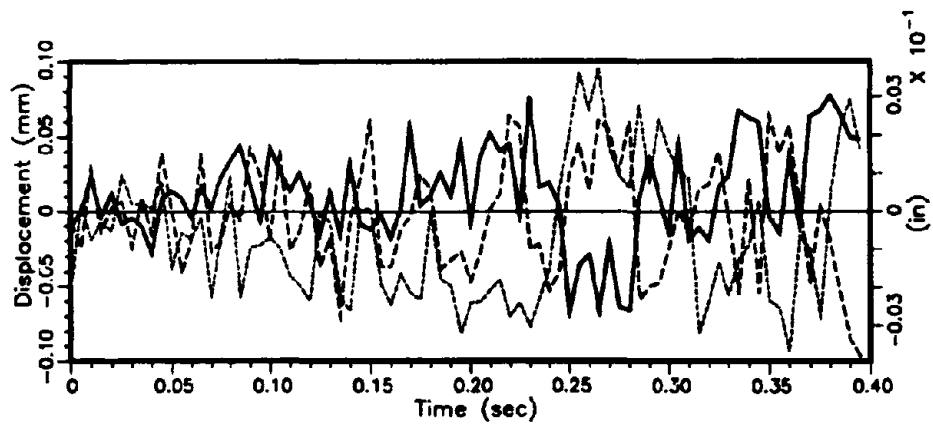
Fig. 5.7. Time Histories, Test 66



(a) Displacement Time History

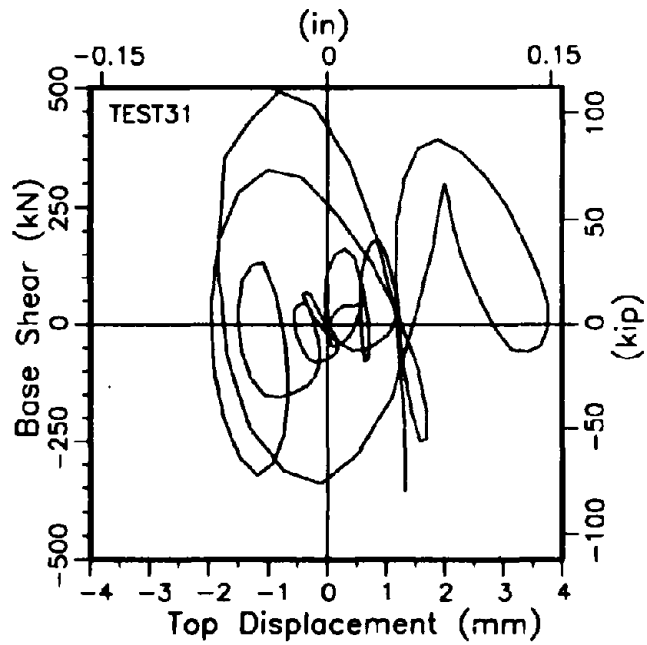


(b) Restoring Force time History

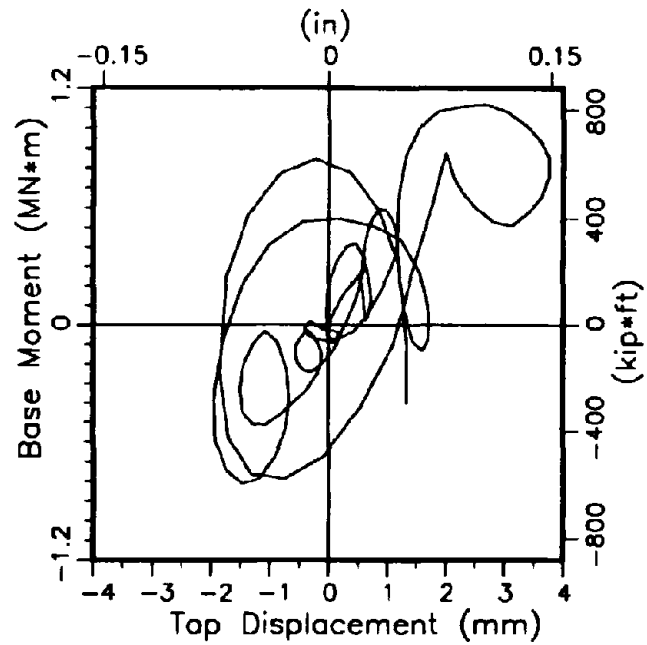


(c) Displacement Error Time History

Fig. 5.8. Time Histories, Test 67

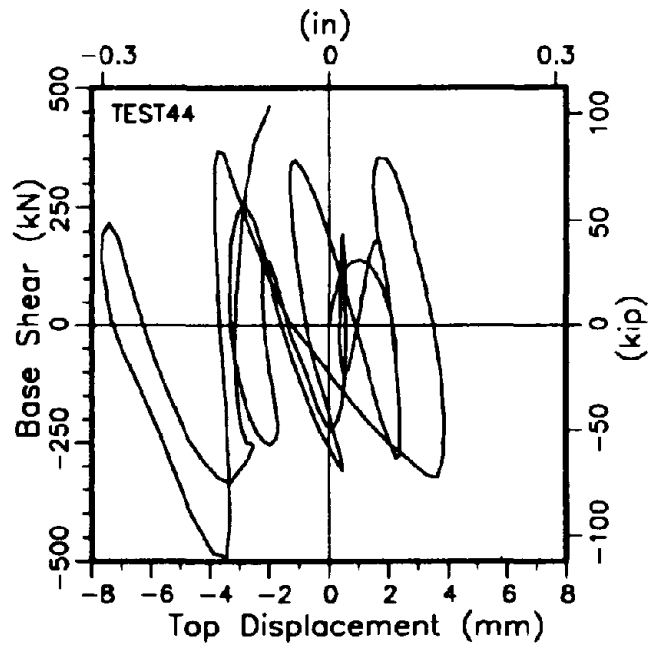


(a) Base Shear vs. Top Displacement

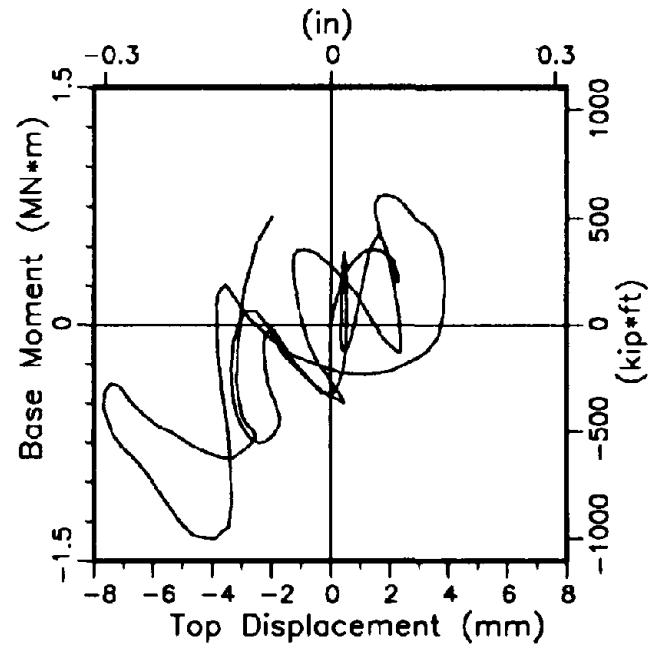


(b) Base Moment vs. Top Displacement

Fig. 5.9. Load-Displacement Behavior, Test 31

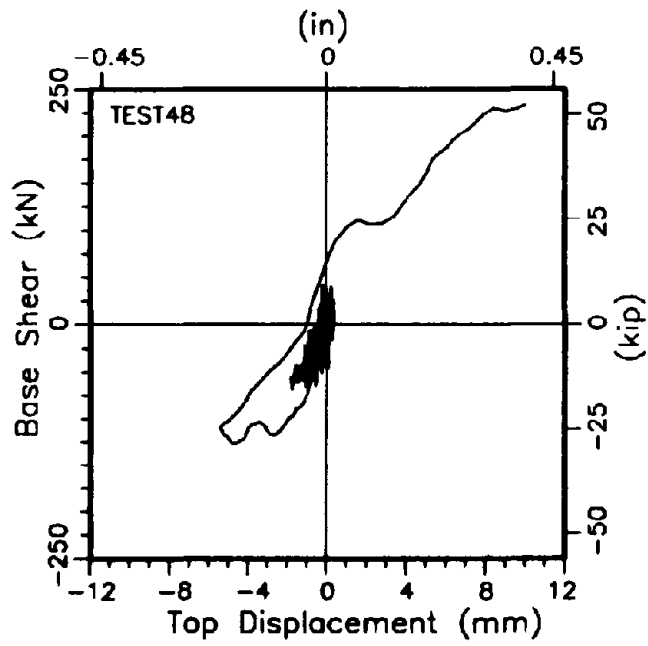


(a) Base Shear vs. Top Displacement

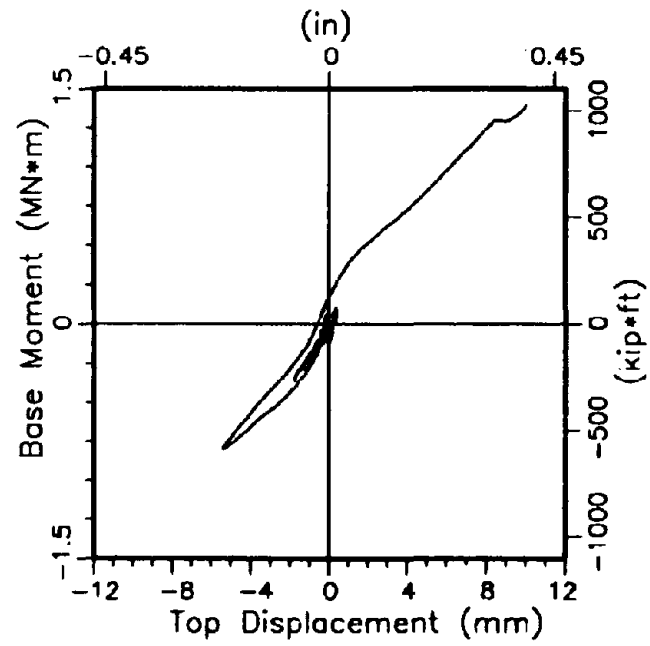


(b) Base Moment vs. Top Displacement

Fig. 5.10. Load-Displacement Behavior, Test 44

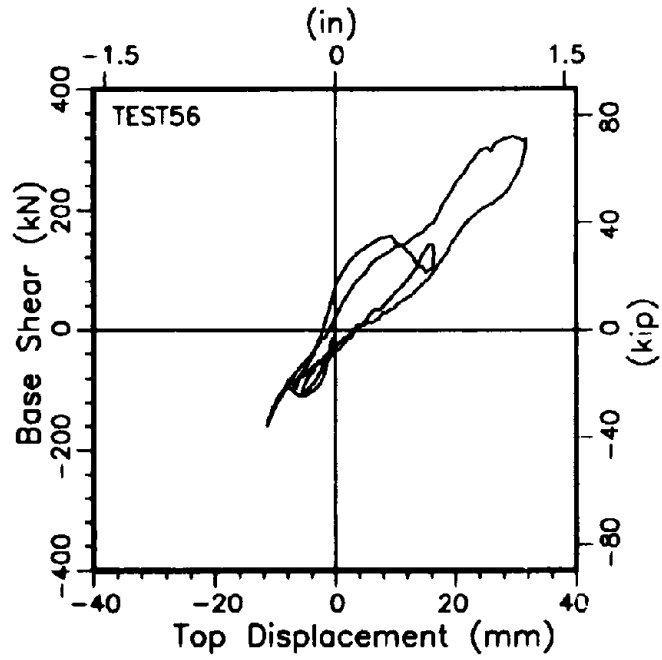


(a) Base Shear vs. Top Displacement

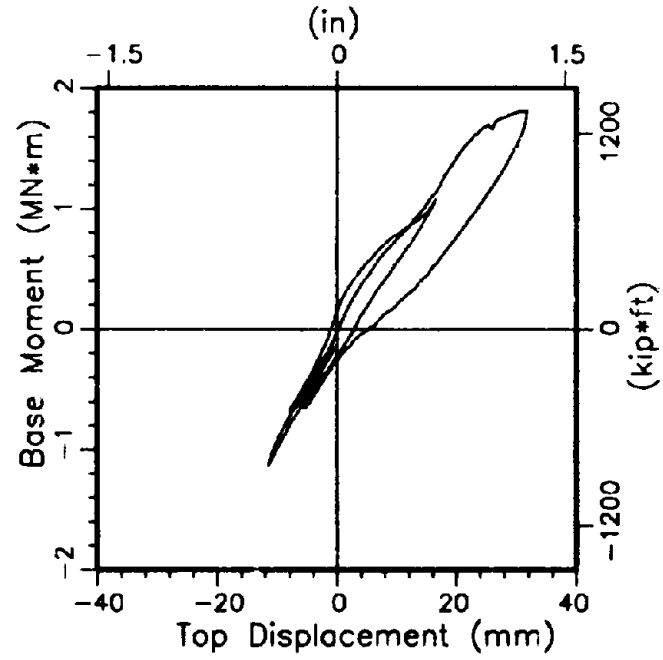


(b) Base Moment vs. Top Displacement

Fig. 5.11. Load-Displacement Behavior, Test 48

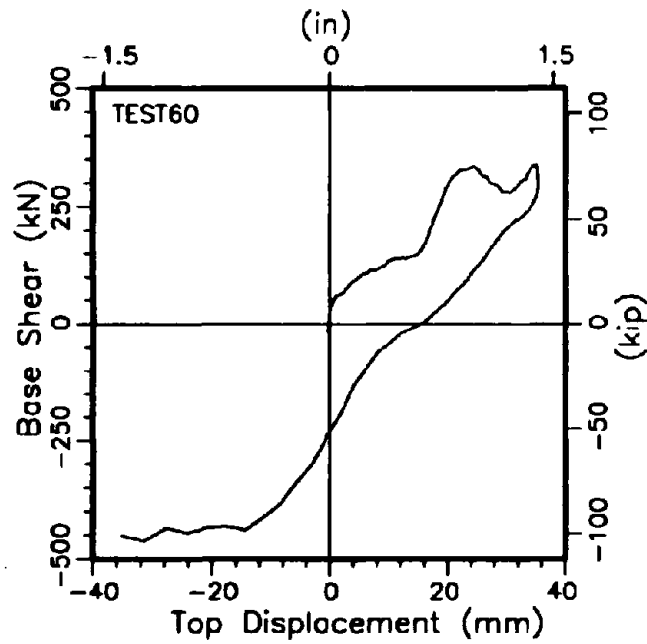


(a) Base Shear vs. Top Displacement

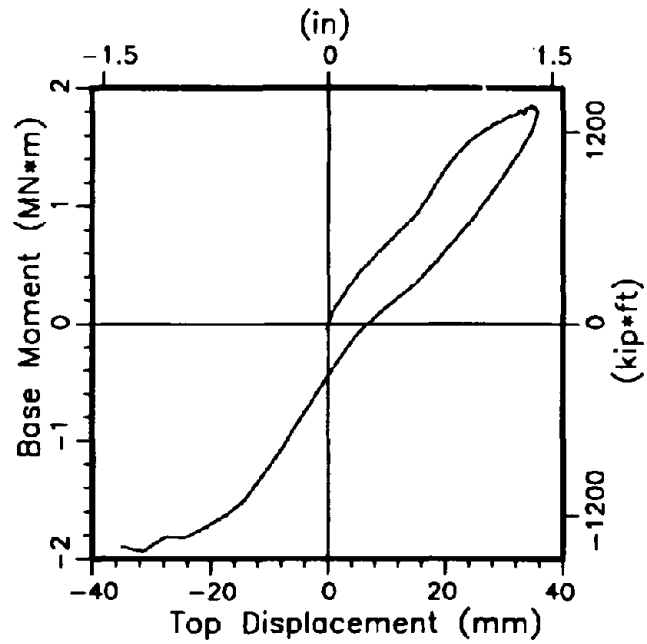


(b) Base Moment vs. Top Displacement

**Fig. 5.12. Load-Displacement Behavior, Test 56**

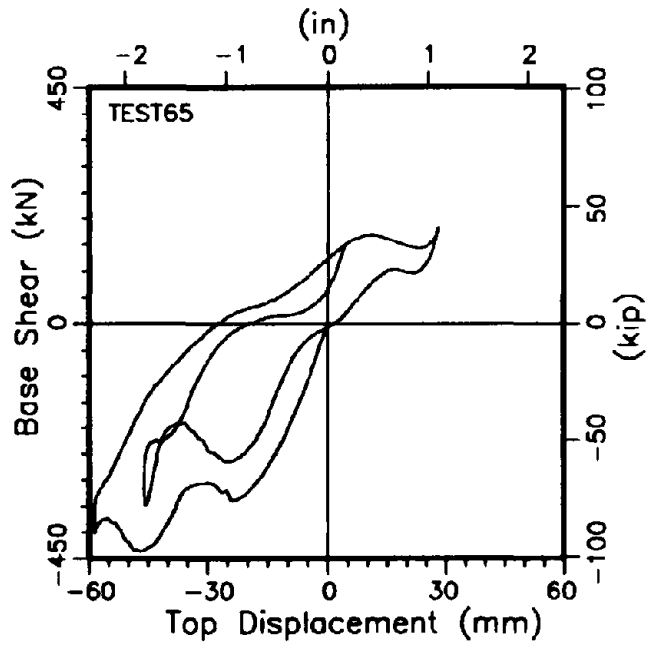


(a) Base Shear vs. Top Displacement

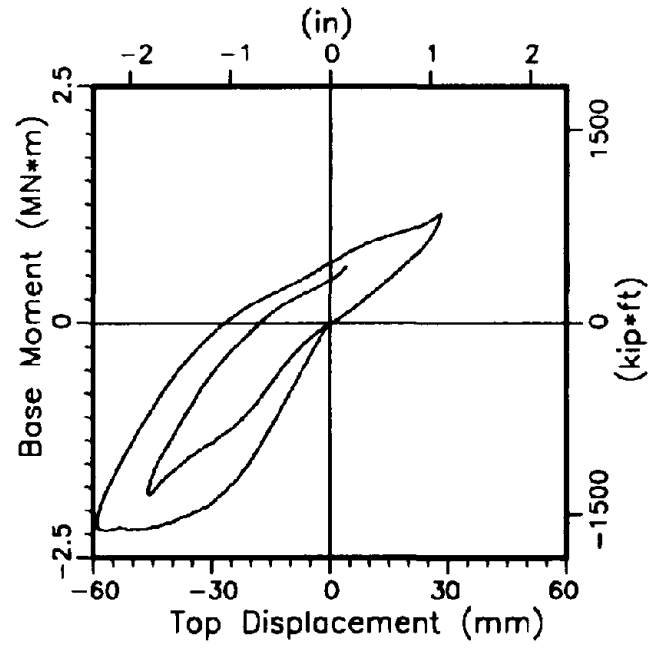


(b) Base Moment vs. Top Displacement

Fig. 5.13. Load-Displacement Behavior, Test 60



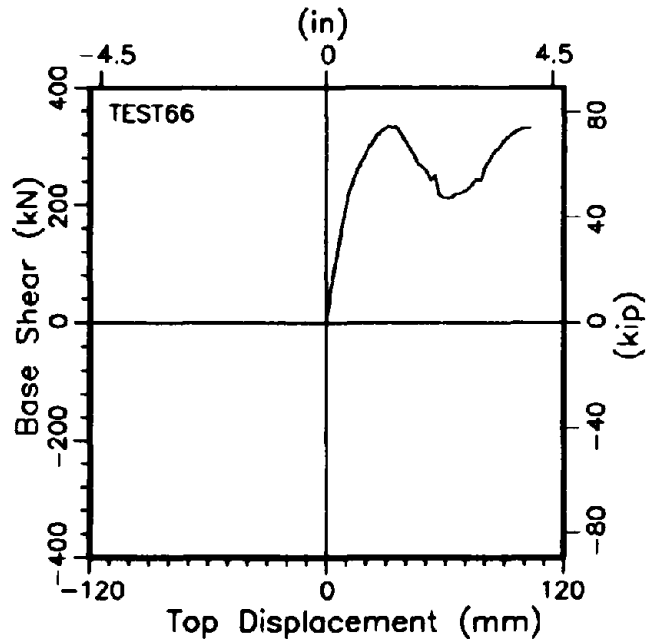
(a) Base Shear vs. Top Displacement



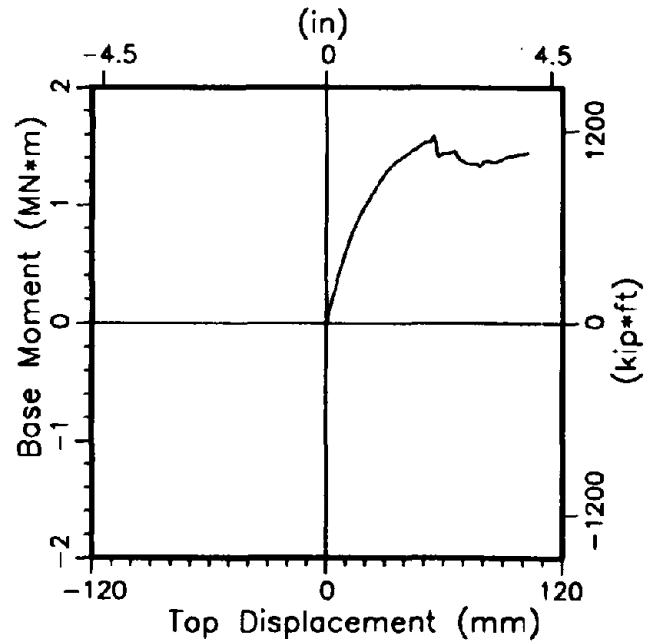
(b) Base Moment vs. Top Displacement

Fig. 5.14. Load-Displacement Behavior, Test 65



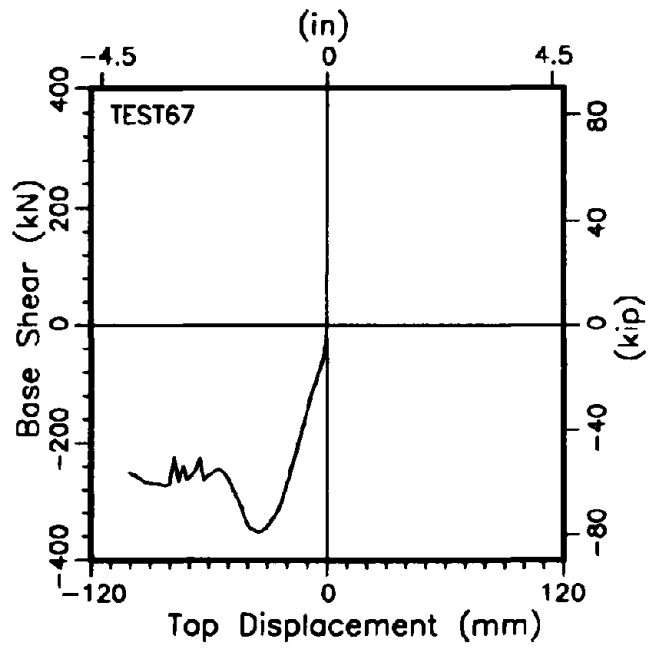


(a) Base Shear vs. Top Displacement

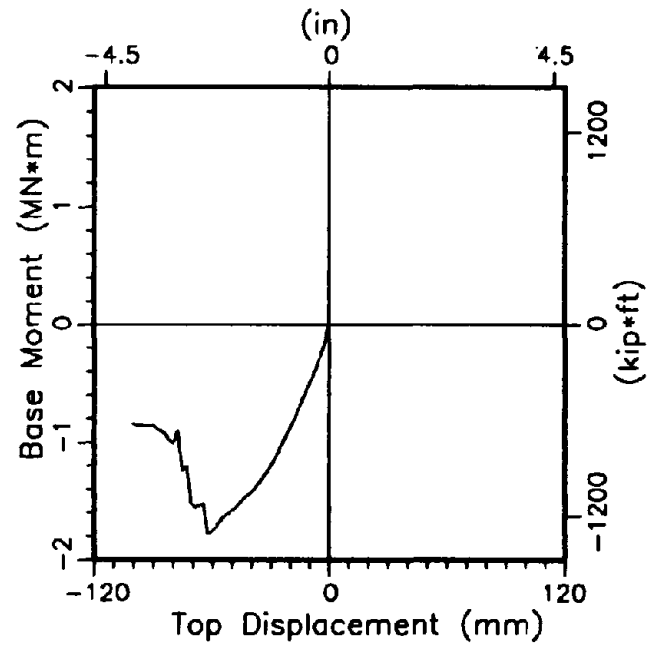


(b) Base Moment vs. Top Displacement

Fig. 5.15. Load-Displacement Behavior, Test 66



(a) Base Shear vs. Top Displacement



(b) Base Moment vs. Top Displacement

Fig. 5.16. Load-Displacement Behavior, Test 67

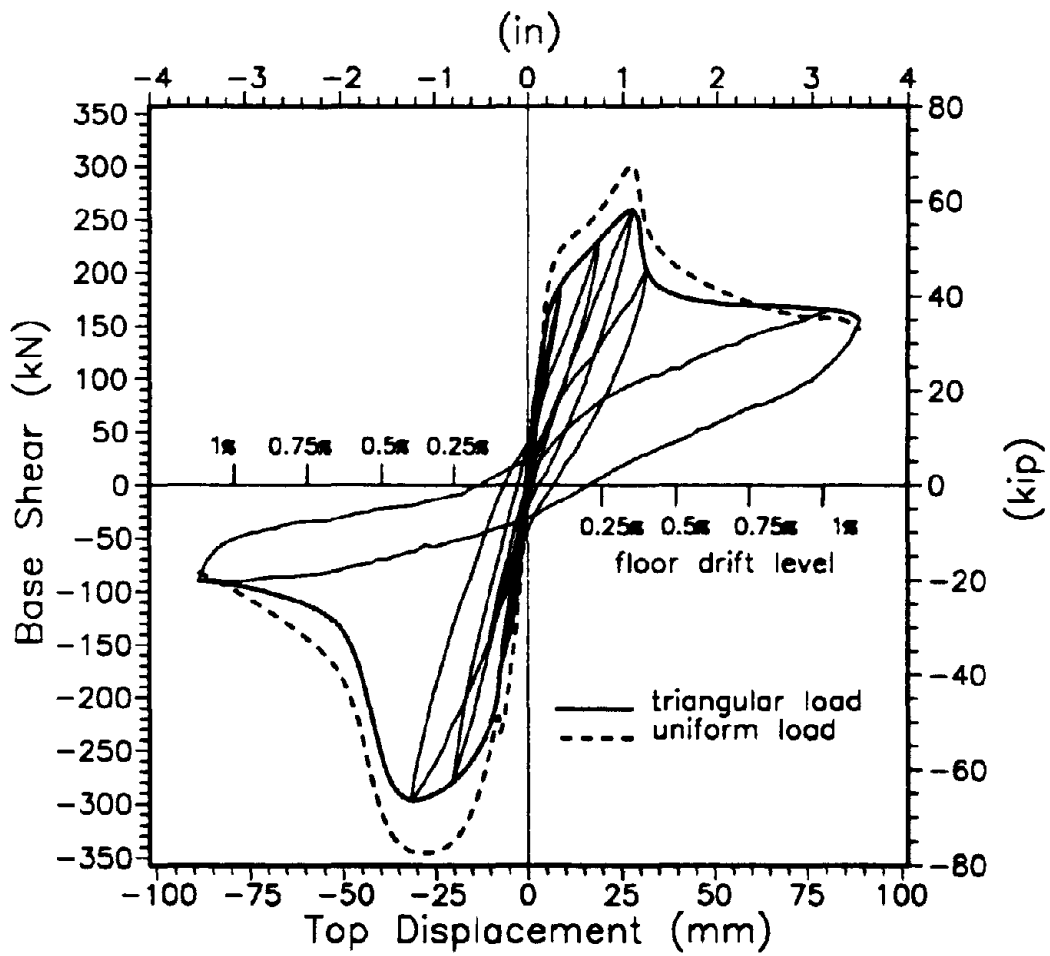


Fig. 5.17. Result of Inverse Triangular and Uniform Loading Test

design models. It can be seen from Figs. 5.9 to 5.16 that the hysteresis loops obtained in pseudo dynamic tests often contain higher mode response, which make it difficult to directly compare the pseudodynamic test results with conventional load distributions such as inverse triangular or uniform loading. In order to make a comparison possible, data points which represent dominant 1st mode response are selected using "filtering" [23]. First, the effective loading height of the resultant lateral load at each time step is calculated and checked if the height falls within the region corresponding to inverse triangular loading (that is  $2/3$  of the total height) and uniform loading ( $1/2$  of the total height). The width of the band is taken as 10" (0.25m), 20"(0.51m) and 30"(0.76m) for different levels of filtering. Results of this filtering indicated that few of the pseudodynamic test data points fall within the band around the uniform loading pattern, while inverse triangular filtering can obtain a significant data population. Hence, the filtering using the inverse triangular loading pattern is considered here. Figure 5.18 shows superimposed filtered data and envelope data for the hysteresis curves obtained from both loading pattern tests. In Fig. 5.18a, the band of 10" width (10" filter) was used to select the data points, while the result of the 20" filter and 30" filters are shown in Fig. 5.18b and 5.18c, respectively. These figures indicate that the GSD tests well represent the behavior of the shear wall under 1st mode response which produces the load pattern close to the inverse triangular shape loading. Incidentally, the last two tests, Test 66 and Test 67 are excluded from the GSD data points because of the large residual displacement offsets at the beginning of these GSD tests which make a comparison of the displacements difficult.

## **5.2. Individual Panel Deformations**

Based on the work by Saffarini and Wilson [17], a method was developed that allows the determination of overall deformation mode shapes of each story height wall panel, and even the displacements of the individual DOFs. This mode-shape information can be a valuable aid for the development of structural analysis models, such as the flexible zone method [17]. A brief

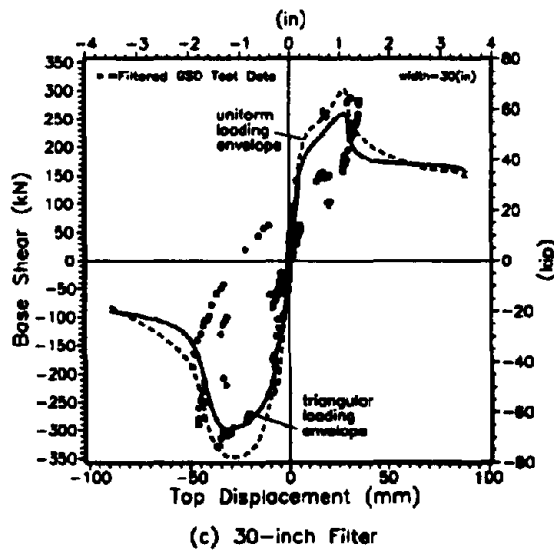
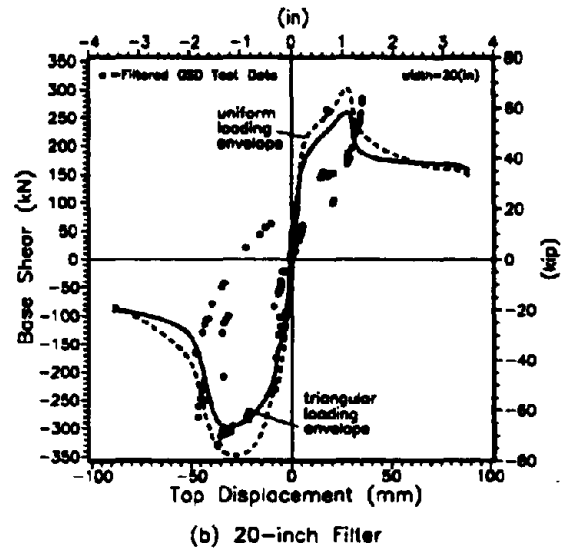
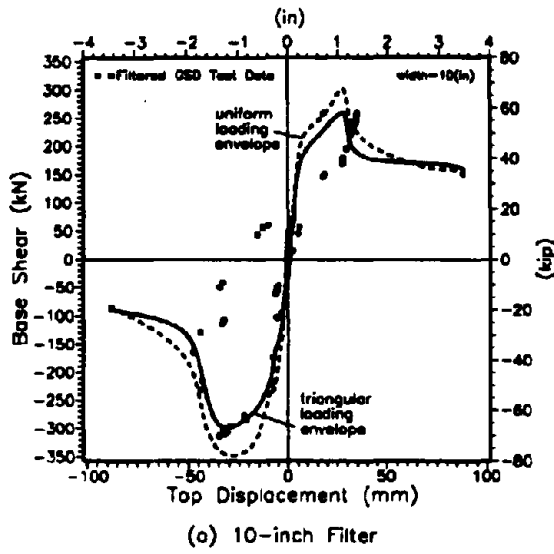


Fig. 5.18 Filtered GSD Test Data Points

description of the underlying theory is presented, and representative results for the experiments reported above are shown.

### 5.2.1. Decomposition of Behavior Modes

The basic idea is to assume linear deformation modes for a wall panel and decompose the overall deformation shape into a combination of 5 simple independent modes, as shown in Fig. 5.19. The 5 deformation quantities can be obtained from the 8 nodal displacements  $u_j$ , (Fig. 5.20) through a 5x8 transformation matrix:

$$\begin{pmatrix} \gamma \\ \theta_x \\ \theta_y \\ \epsilon_x \\ \epsilon_y \end{pmatrix} = \begin{bmatrix} \frac{1}{2H} & -\frac{1}{2D} & -\frac{1}{2H} & -\frac{1}{2D} & -\frac{1}{2H} & \frac{1}{2D} & \frac{1}{2H} & \frac{1}{2D} \\ \frac{1}{H} & 0 & -\frac{1}{H} & 0 & \frac{1}{H} & 0 & -\frac{1}{H} & 0 \\ 0 & -\frac{1}{D} & 0 & \frac{1}{D} & 0 & -\frac{1}{D} & 0 & \frac{1}{D} \\ -\frac{1}{2D} & 0 & -\frac{1}{2D} & 0 & \frac{1}{2D} & 0 & \frac{1}{2D} & 0 \\ 0 & \frac{1}{2H} & 0 & -\frac{1}{2H} & 0 & -\frac{1}{2H} & 0 & \frac{1}{2H} \end{bmatrix} \begin{pmatrix} u_{1x} \\ u_{1y} \\ u_{2x} \\ u_{2y} \\ u_{3x} \\ u_{3y} \\ u_{4x} \\ u_{4y} \end{pmatrix} \quad (5.1)$$

Since the  $u_j$  are difficult to measure in practice, these mode shape quantities are expressed in terms of the easily measurable quantities  $\zeta_i$  defined in Fig. 5.20. To do this, the nodal displacements are expressed in terms of the relative displacements  $\zeta_i$ , then substituted into eqn. (5.1) to get the desired relationship. Of the six  $\zeta_i$ , only five are needed to uniquely define the mode shapes. However, a more general approach, using all six, was taken as follows. First, the

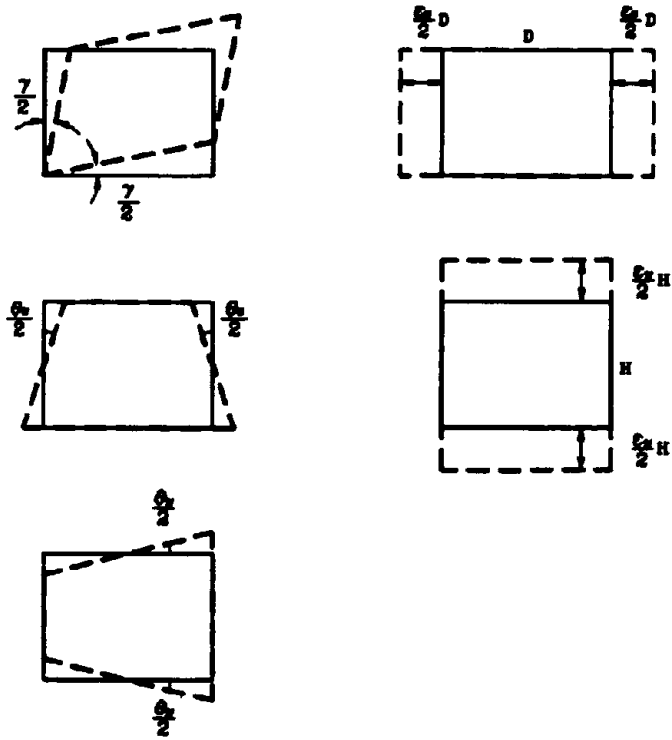


Fig. 5.19. Linear Deformation Modes

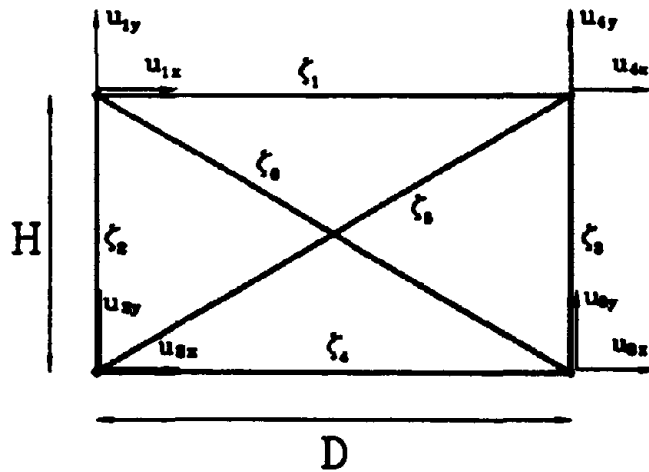


Fig. 5.20. Definition of Nodal Displacements and Relative Displacements

$\zeta_i$  are expressed in terms of the 8 quantities  $u_{ij}$ , which in general gives non-linear relationships. Next, recognizing that the  $\zeta_i$  can not provide rigid body translation or rotation information, three of the quantities  $u_{ij}$  are restricted based on experimental constraints. With the reasonable assumption of rigid floor slabs relative to the wall panels, the choice was

$$\left. \begin{array}{l} u_{2x} = 0 \\ u_{2y} = 0 \\ u_{3y} = 0 \end{array} \right\} \quad (5.2)$$

With this assumption, after appropriate linearization, the following relationship between the  $\zeta_i$  and the remaining 5  $u_{ij}$  is obtained:

$$\left\{ \begin{array}{l} \zeta_1 \\ \zeta_2 \\ \zeta_3 \\ \zeta_4 \\ \zeta_5 \\ \zeta_6 \end{array} \right\} = \left[ \begin{array}{cccccc} -1 & 0 & 1 & 0 & 0 & 0 \\ 0 & 1 & 0 & 0 & 0 & 0 \\ 0 & 0 & 0 & 1 & 0 & 0 \\ 0 & 0 & 0 & 0 & 0 & 1 \\ 0 & 0 & \frac{D}{\sqrt{D^2+H^2}} & \frac{H}{\sqrt{D^2+H^2}} & 0 & 0 \\ -\frac{D}{\sqrt{D^2+H^2}} & \frac{H}{\sqrt{D^2+H^2}} & 0 & 0 & \frac{D}{\sqrt{D^2+H^2}} & 0 \end{array} \right] \left\{ \begin{array}{l} u_{1x} \\ u_{1y} \\ u_{4x} \\ u_{4y} \\ u_{2x} \end{array} \right\} \quad (5.3)$$

Equation (5.3) can be expressed as

$$\mathbf{z} = \mathbf{T}_1 \hat{\mathbf{u}} \quad (5.4)$$

Since this is an overdetermined system, the singular value decomposition is used to obtain a solution in a least squares sense [18]. The least squares solution is defined as the  $\hat{\mathbf{u}}$  that minimizes the error defined by

$$\mathbf{e}^2 = (\mathbf{T}_1 \hat{\mathbf{u}} - \mathbf{z})^T (\mathbf{T}_1 \hat{\mathbf{u}} - \mathbf{z}). \quad (5.5)$$

The singular value decomposition is used to obtain the least squares solution. The matrix  $\mathbf{T}_1$  is factorized as

$$\mathbf{T}_1 = \mathbf{U} \mathbf{W} \mathbf{V}^T, \quad (5.6)$$



where

$U$  = a column orthogonal matrix of dimension  $6 \times 5$ ,

$W = \text{diag}(w_1, \dots, w_5)$ ,

$V$  = an orthogonal square matrix of dimension 5.

The least squares solution then is calculated by

$$\hat{u} = VW^{-1}U^Tz. \quad (5.7)$$

Finally,  $\hat{u}$  is combined with (5.2), then (5.1) to give the desired result. The advantage of using the least square method with all six possible relative displacement measurements  $\zeta_{ij}$ , is that this way the method allows the freedom to restrict any one of the  $\zeta_{ij}$  arbitrarily, without changing the formulation. For example, zero elongation of both upper and lower floor slabs for a wall panel can easily be accommodated.

### 5.2.2. Test Results

Representative results, using the technique described above, are shown in Figs. 5.21 through 5.28. It should be noted that, of the 5 deformation modes, shear  $\gamma$ , flexure  $\theta$ , and vertical expansion  $\epsilon_y$ , are dominant. When the test structure is exercised to large deformation, the vertical expansion component  $\epsilon_y$ , has a tendency to grow in the positive direction, rather than staying around the zero value, which corresponds to flexural growth of reinforced concrete members in the plastic region.

### 5.3. Curvature Distributions

Figures 5.29 through 5.36 show the measured curvature distribution over the bottom region of the 1st story wall. As can be seen from these figures, a localized stiff region is observed between 8 in.=0.20m and 16 in.=0.41m up from the base. This stiffening effect is due to the lap splice and the increased amount of reinforcement in this region.

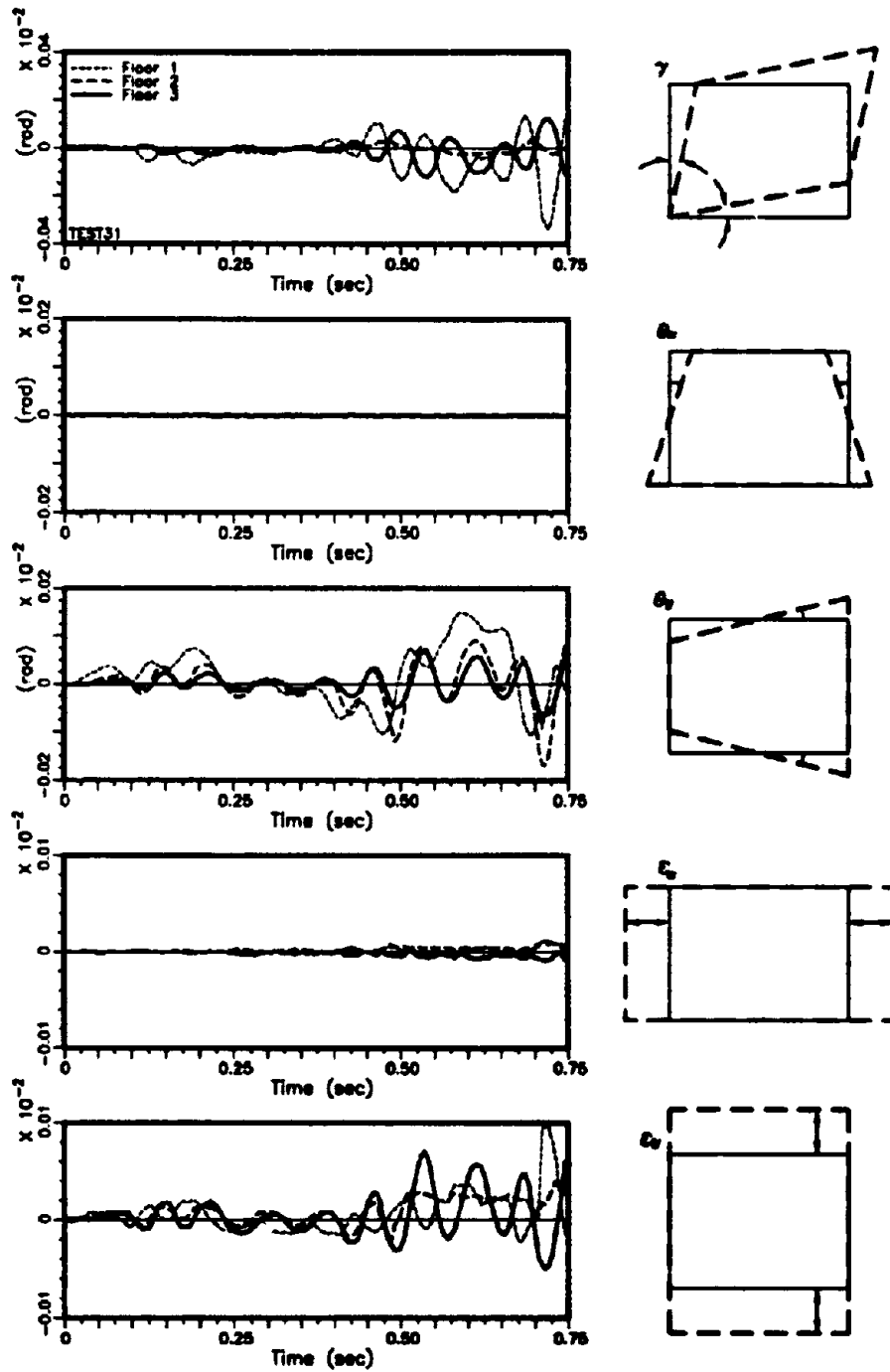


Fig. 5.21. Wall Panel Deformation Modes, Test 31

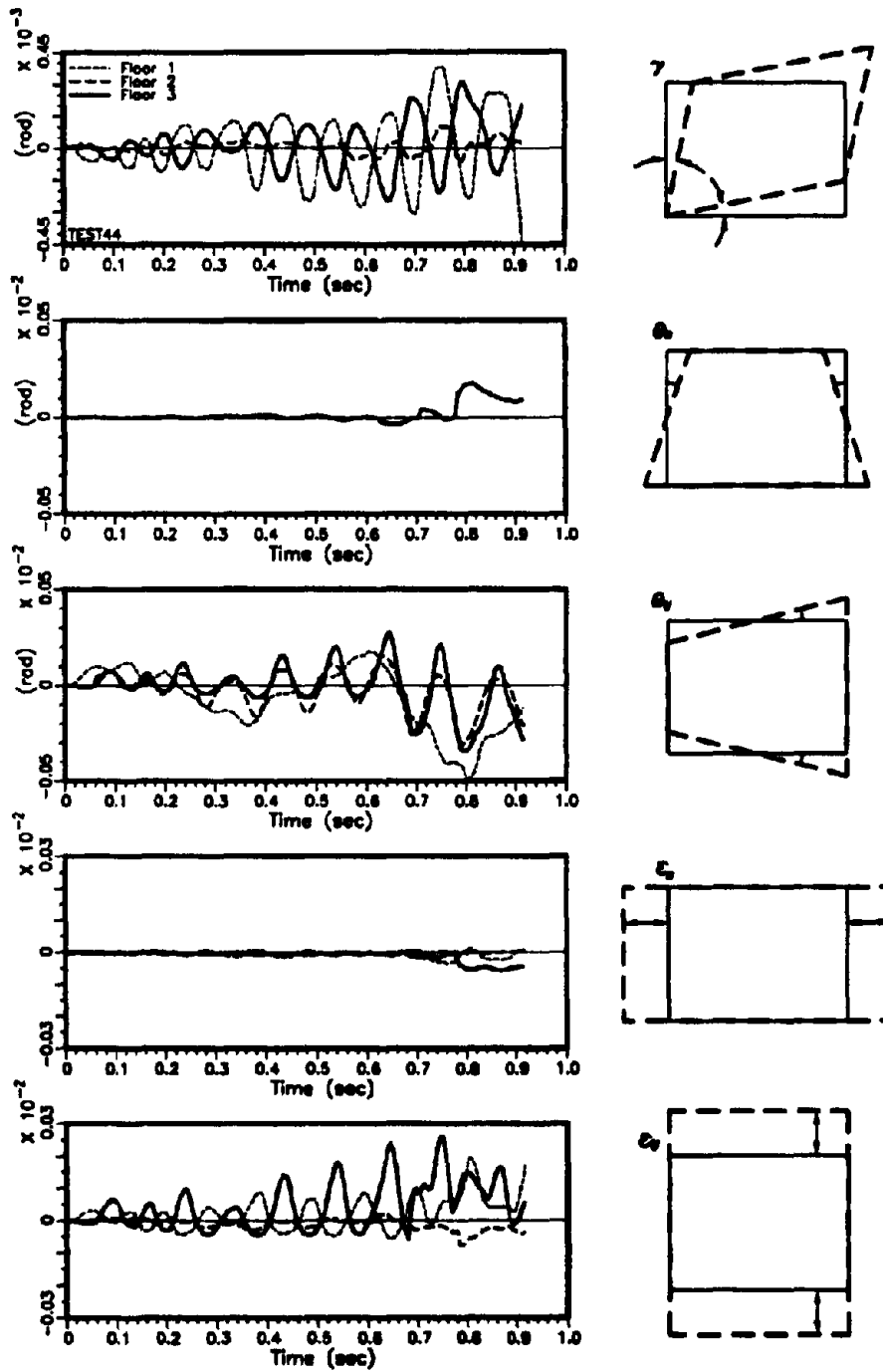


Fig. 5.22. Wall Panel Deformation Modes, Test 44

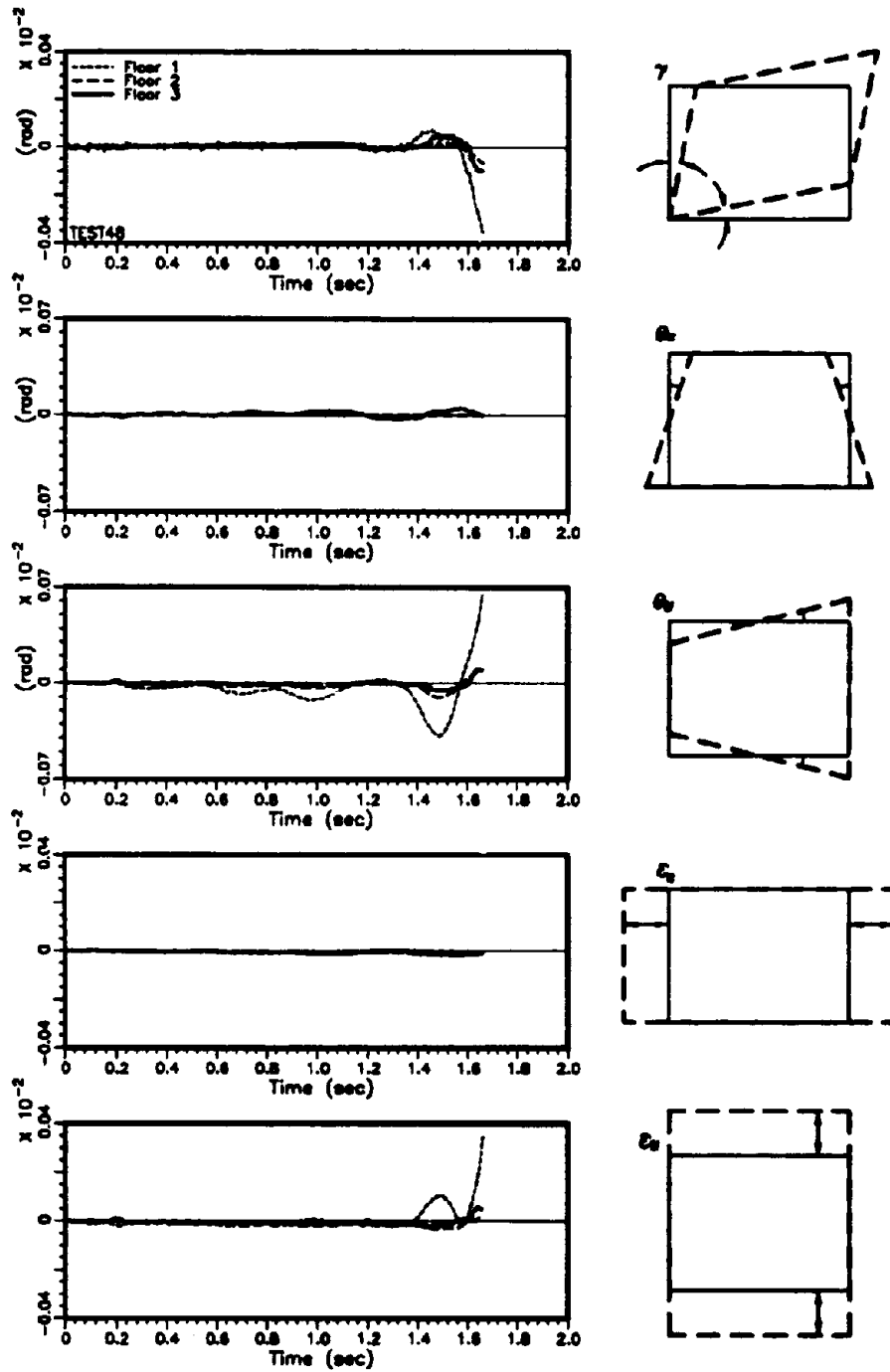


Fig. 5.23. Wall Panel Deformation Modes, Test 48

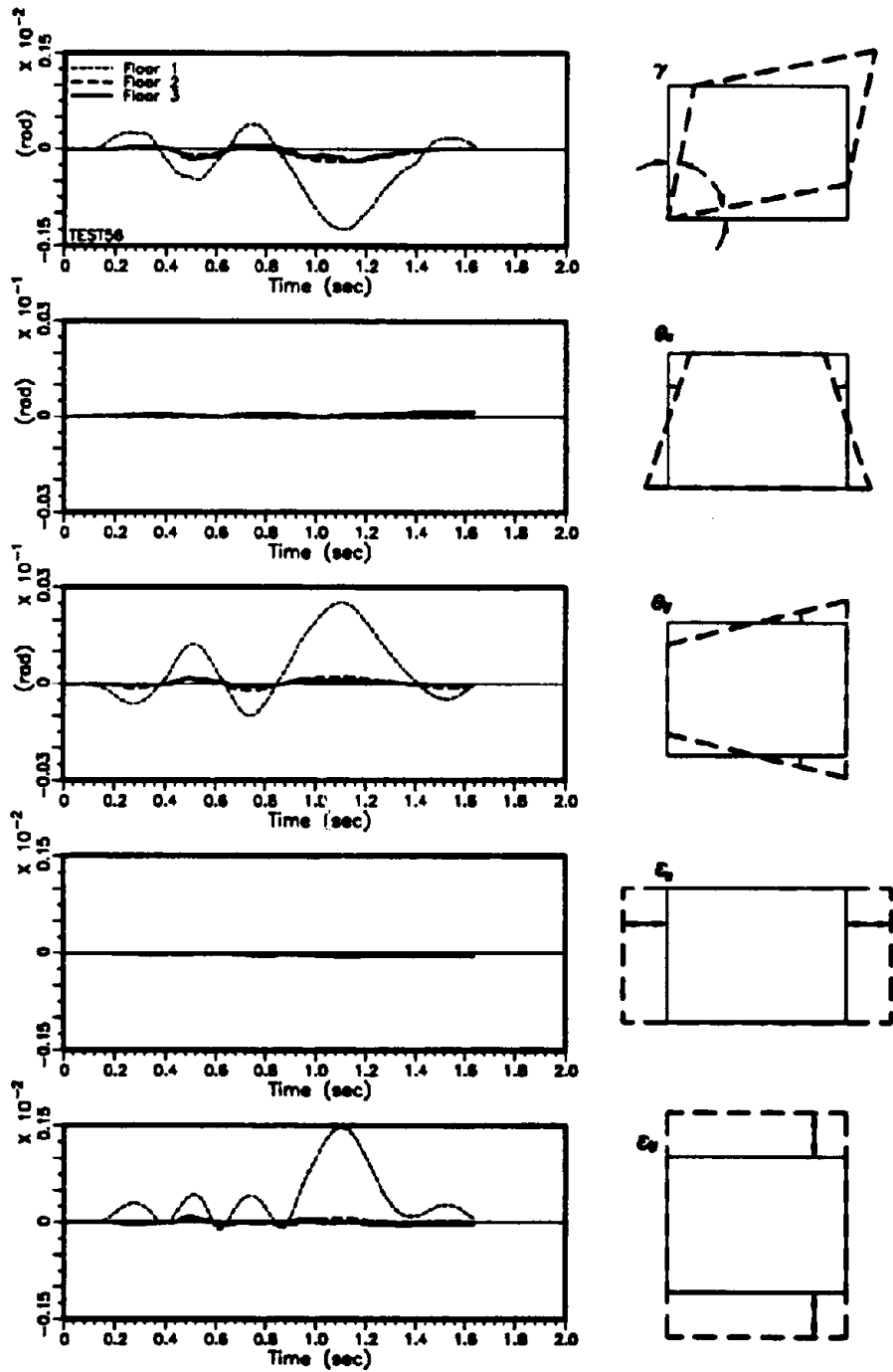


Fig. 5.24. Wall Panel Deformation Modes, Test 56

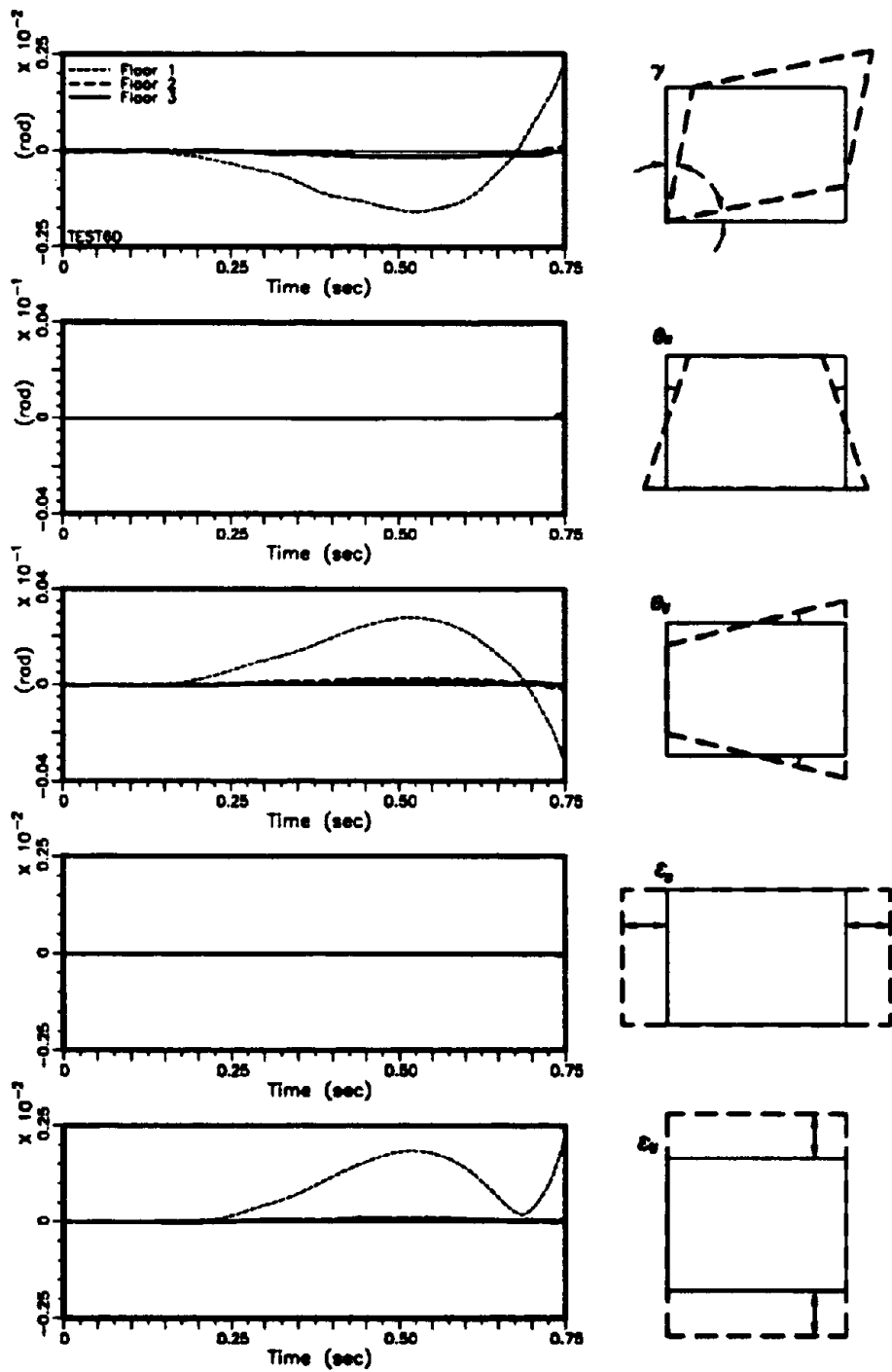


Fig. 5.25. Wall Panel Deformation Modes, Test 60

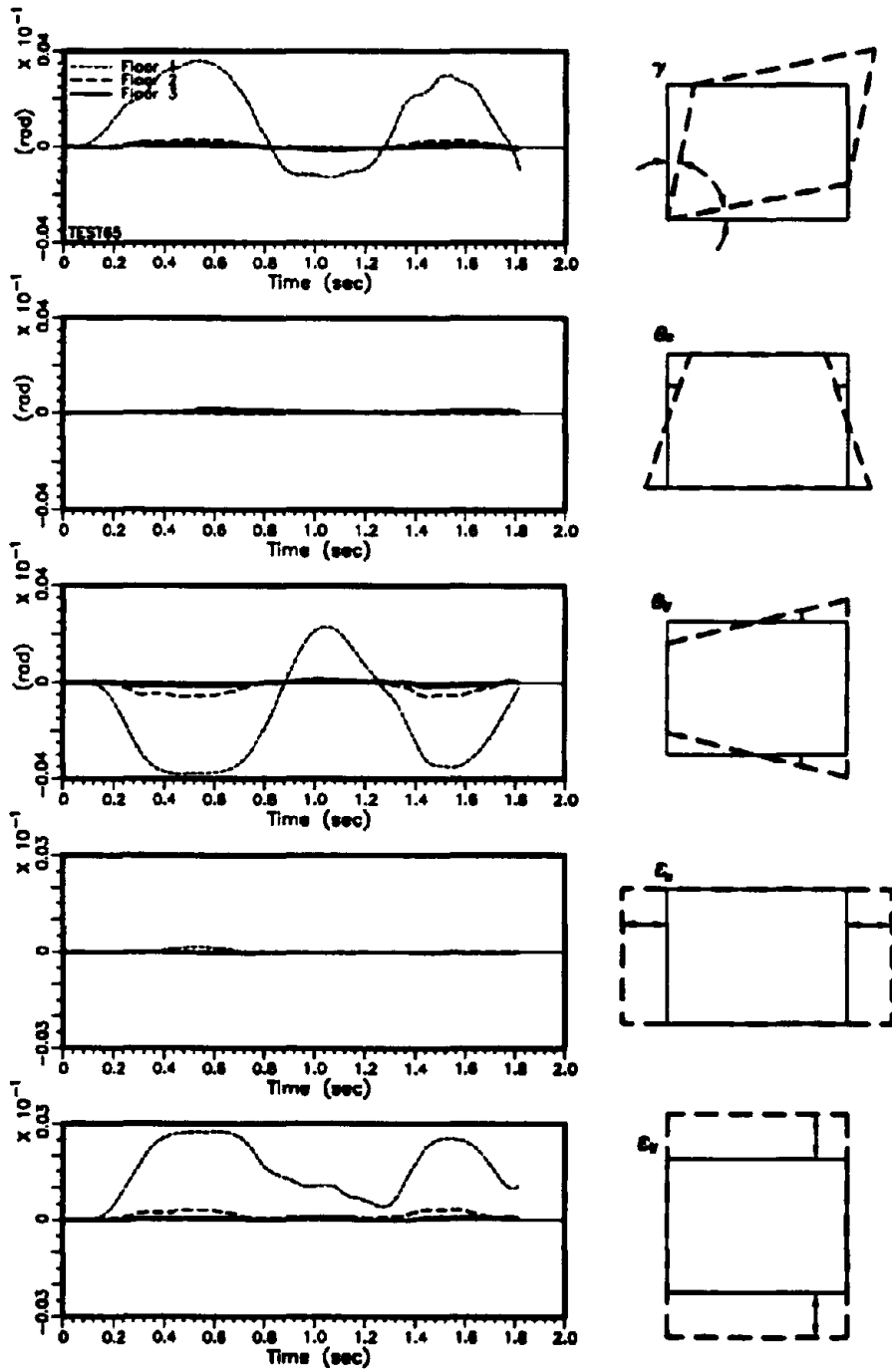


Fig. 5.26. Wall Panel Deformation Modes, Test 65

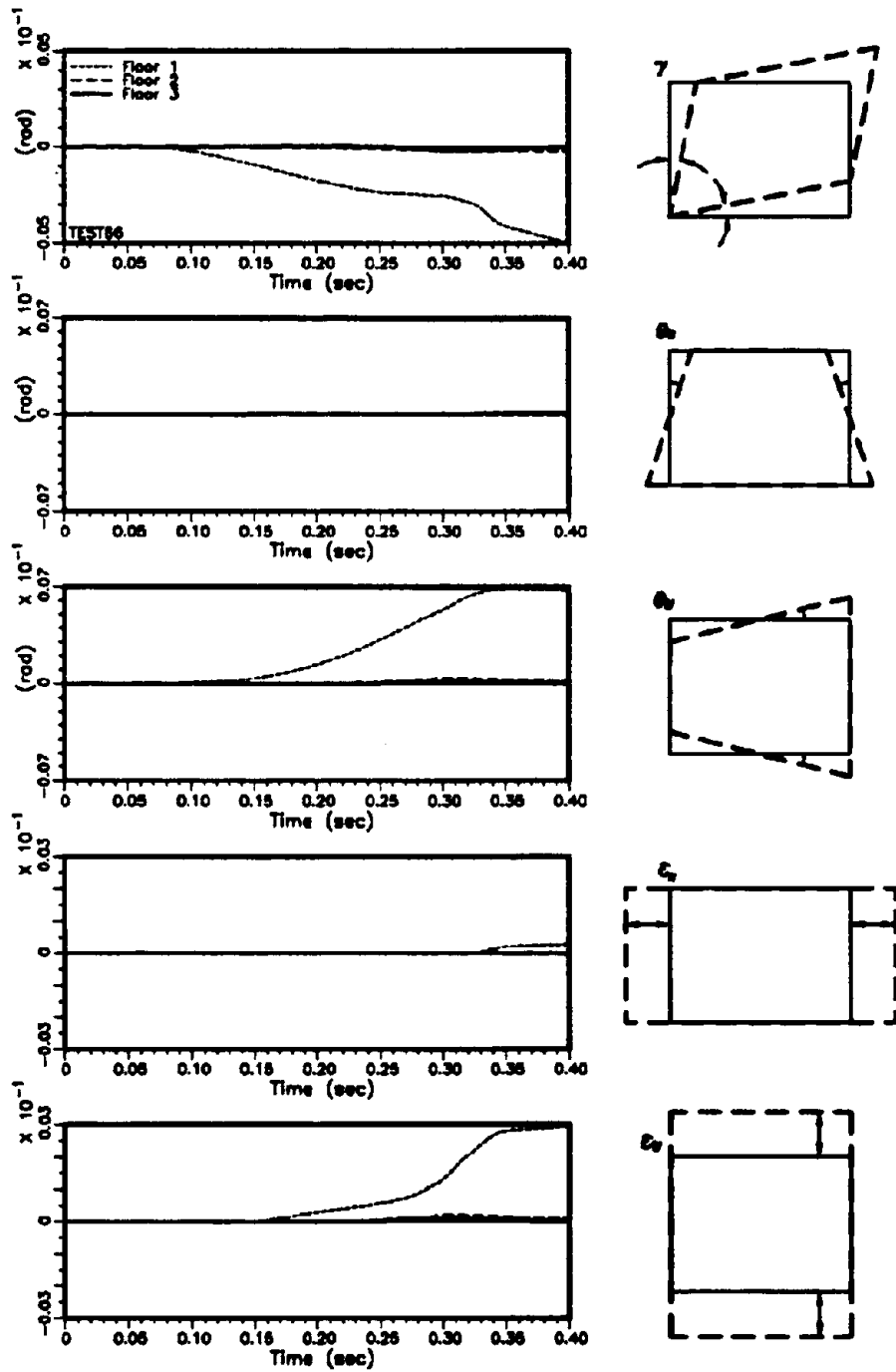


Fig. 5.27. Wall Panel Deformation Modes, Test 66



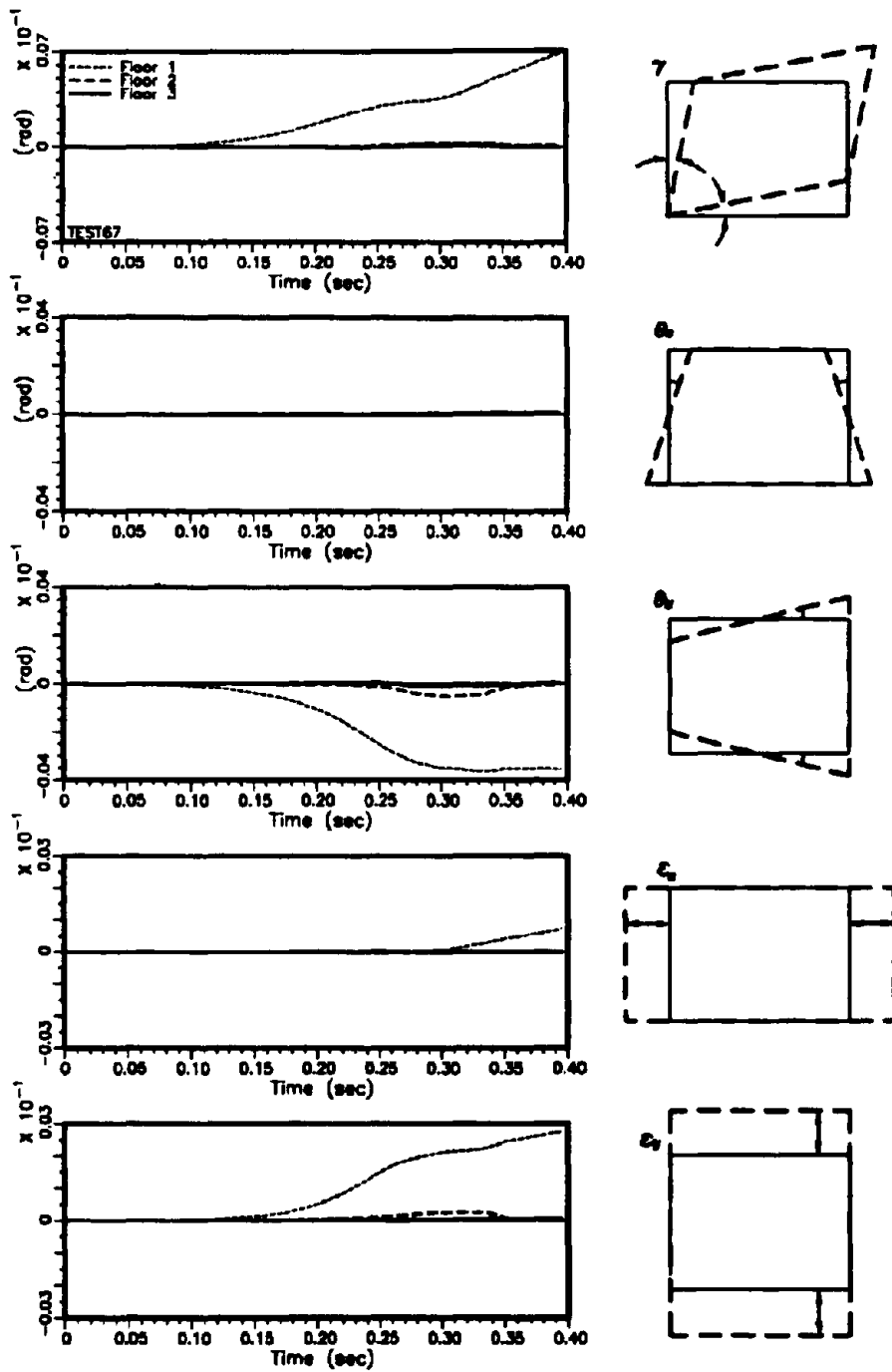


Fig. 5.28. Wall Panel Deformation Modes, Test 67

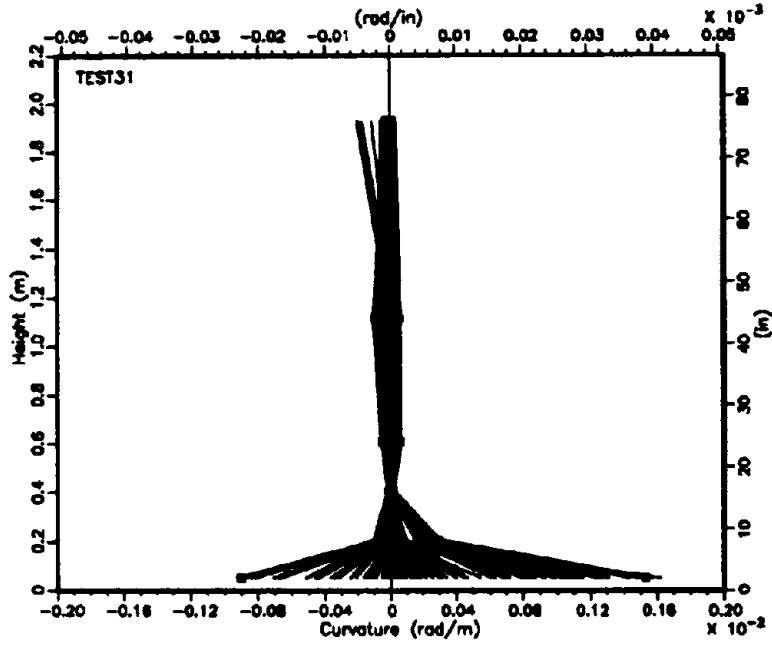


Fig. 5.29. Curvature Distribution, Test 31

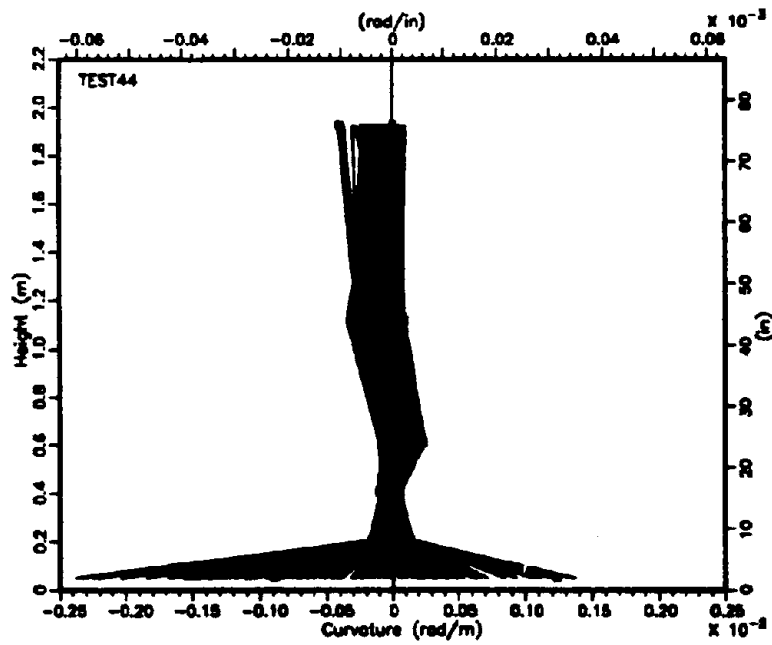


Fig. 5.30. Curvature Distribution, Test 44

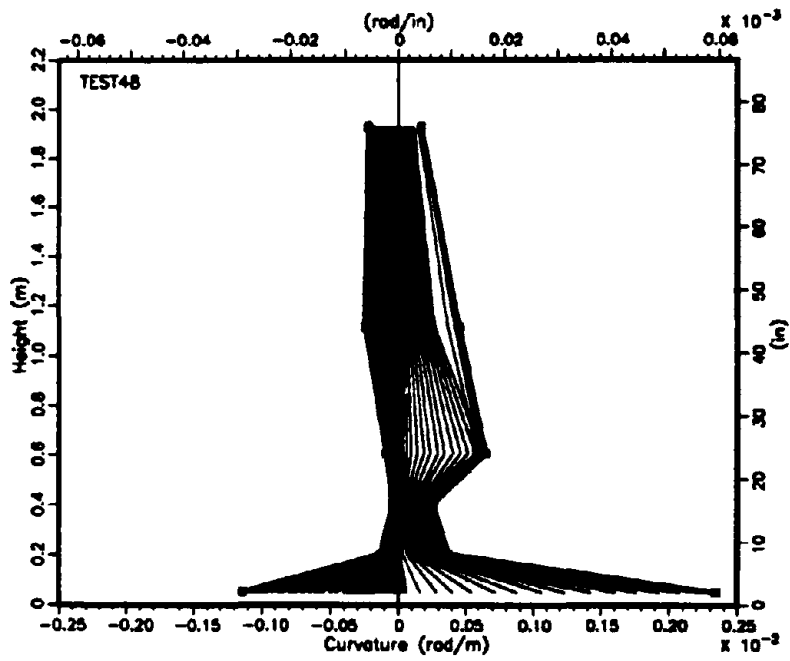


Fig. 5.31. Curvature Distribution, Test 48

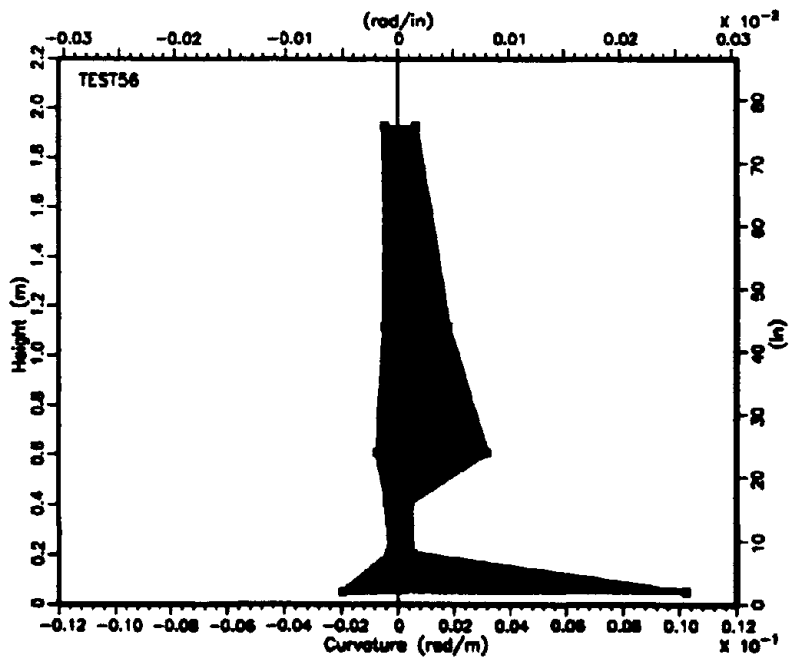


Fig. 5.32. Curvature Distribution, Test 56

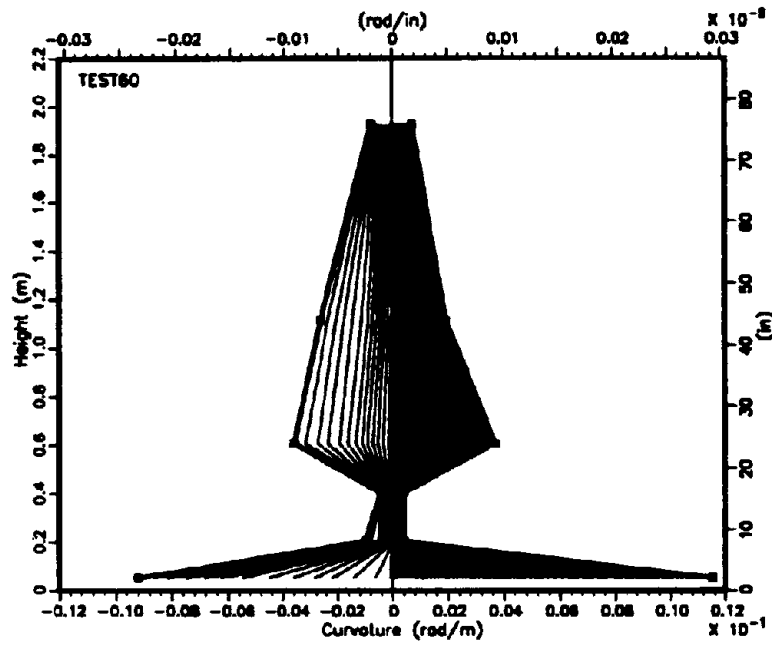


Fig. 5.33. Curvature Distribution, Test 60

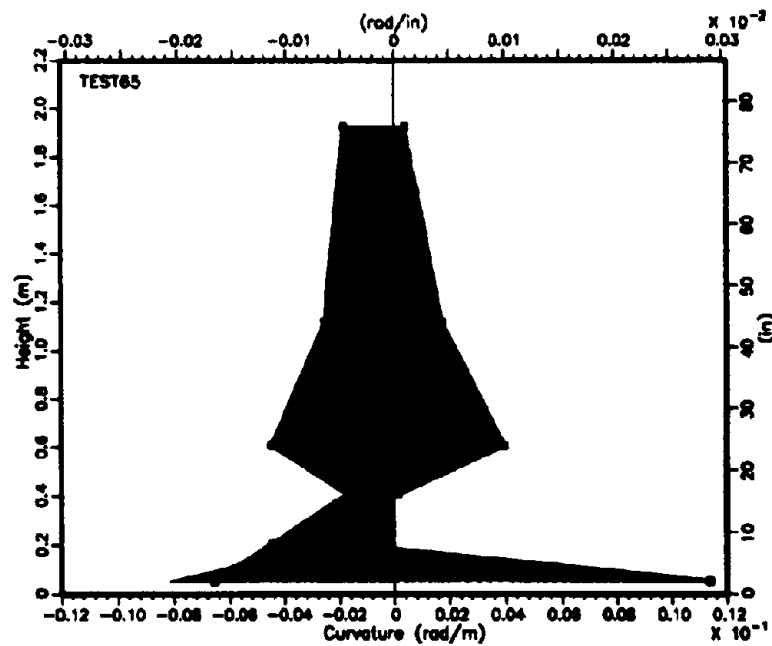


Fig. 5.34. Curvature Distribution, Test 65

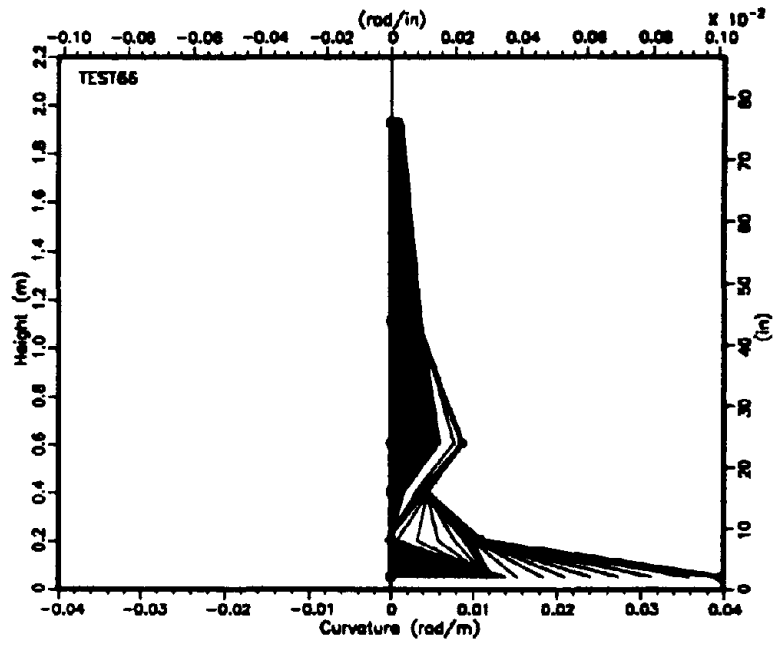


Fig. 5.35. Curvature Distribution, Test 66

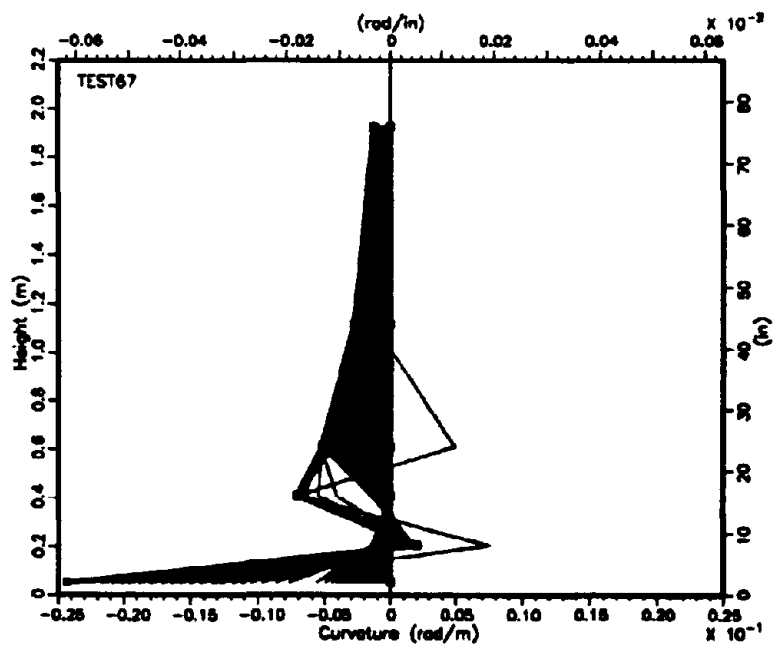


Fig. 5.36. Curvature Distribution, Test 67

#### **5.4. Rebar Strain**

Several rebar/strain distribution time histories are shown in Figs. 5.37 through 5.40. The first figure, Fig. 5.37, shows strain gage readings during Test 18, briefly described in the previous chapter, along the rebar strain gage locations 1 through 8 in Fig. 3.5. This figure represents the rebar strain behavior when the deformation is relatively small (maximum strain is about  $370\mu$ ). It can be observed that there is a neutral position where strain is always zero, similar to the neutral axis in linear bending. Figure 5.39, showing Test 44, represents the strain distribution when the peak strain exceeds the yield strain (maximum strain is about  $3100\mu$ ). The strains tend to distribute uniformly on the tension side. In Fig. 5.40 (Test 48), tension becomes dominant over the strains on compression side.

#### **5.5. Repair and Retest of 3-Story Wall**

After testing of the 3-story wall to the point of toe crushing, the wall was repaired and retested to investigate the effectiveness of repair measures. The repair measures consisted of rebuilding the crushed compression toe with polymer concrete, epoxy injecting all flexural cracks in the first story wall and overlaying 3 layers of  $45^\circ$  bidirectional woven glass fiber fabric/epoxy composites on both sides of the first story wall. In Figs. 5.41 through 5.44, the load/displacement hysteresis plots under inverse triangular loading of the repaired 3-story wall are shown. Narrow hysteresis loops and capacity drops are indicative of lap splice debonding or the wall reinforcement. This phenomenon is also captured by Figs. 5.45 and 5.46 which show the curvature distributions of the repaired 3-story wall during Test 76 and Test 77, respectively. It can be observed that flexural action is largely concentrated in the joint to the base of the wall.

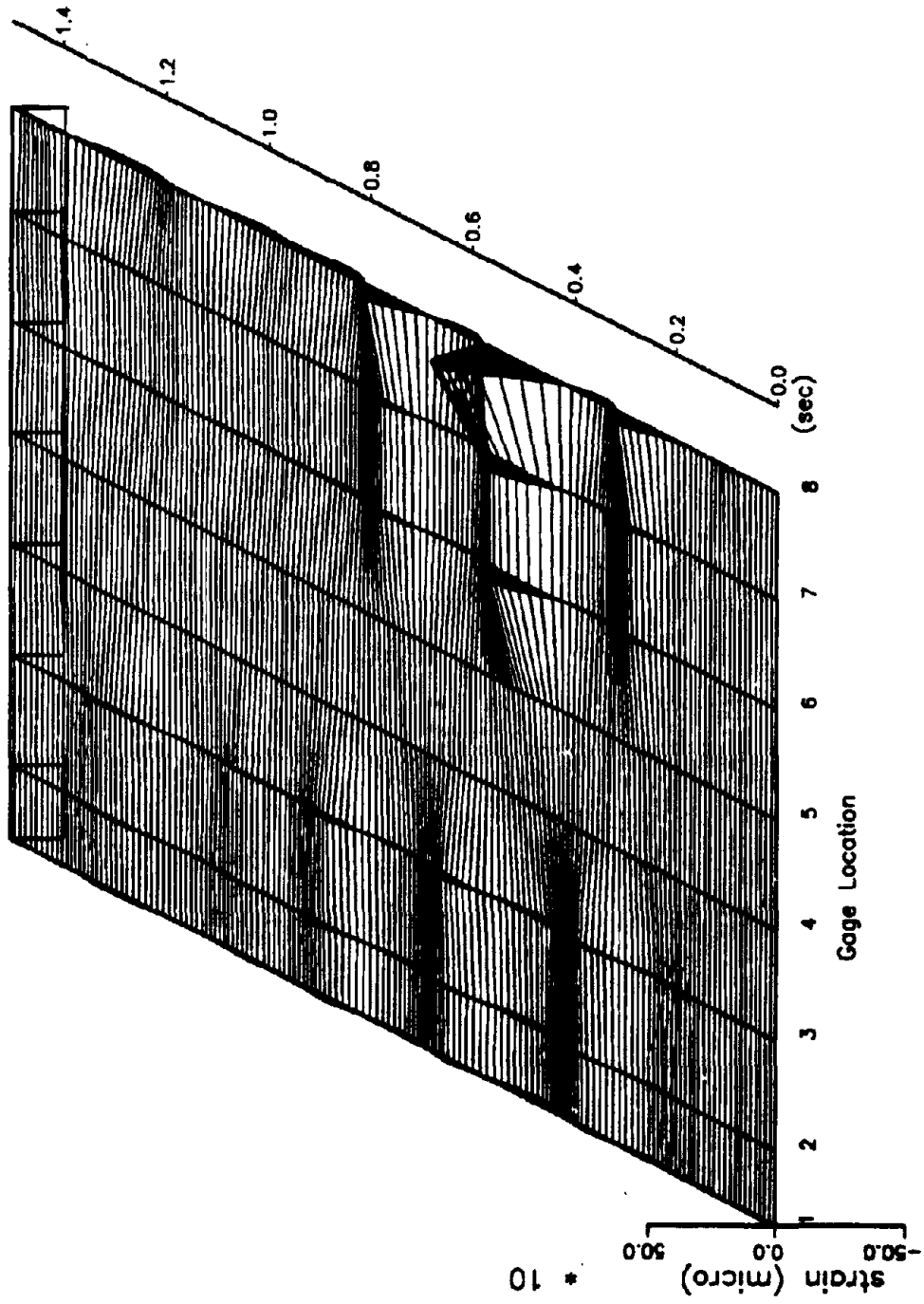


Fig. 5.37. Reinforcement Strain, Test 18

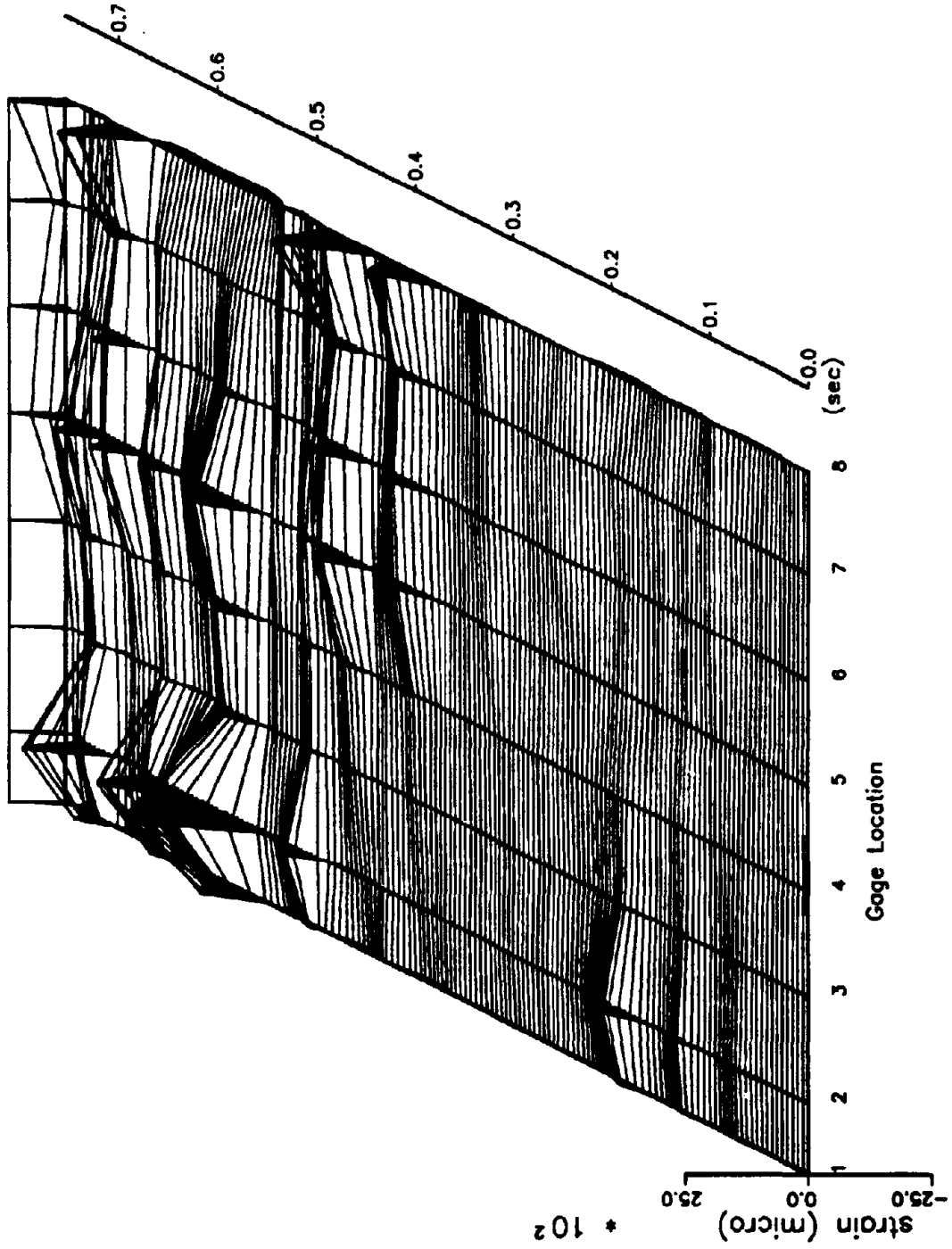


Fig. 5.38. Reinforcement Strain, Test 31



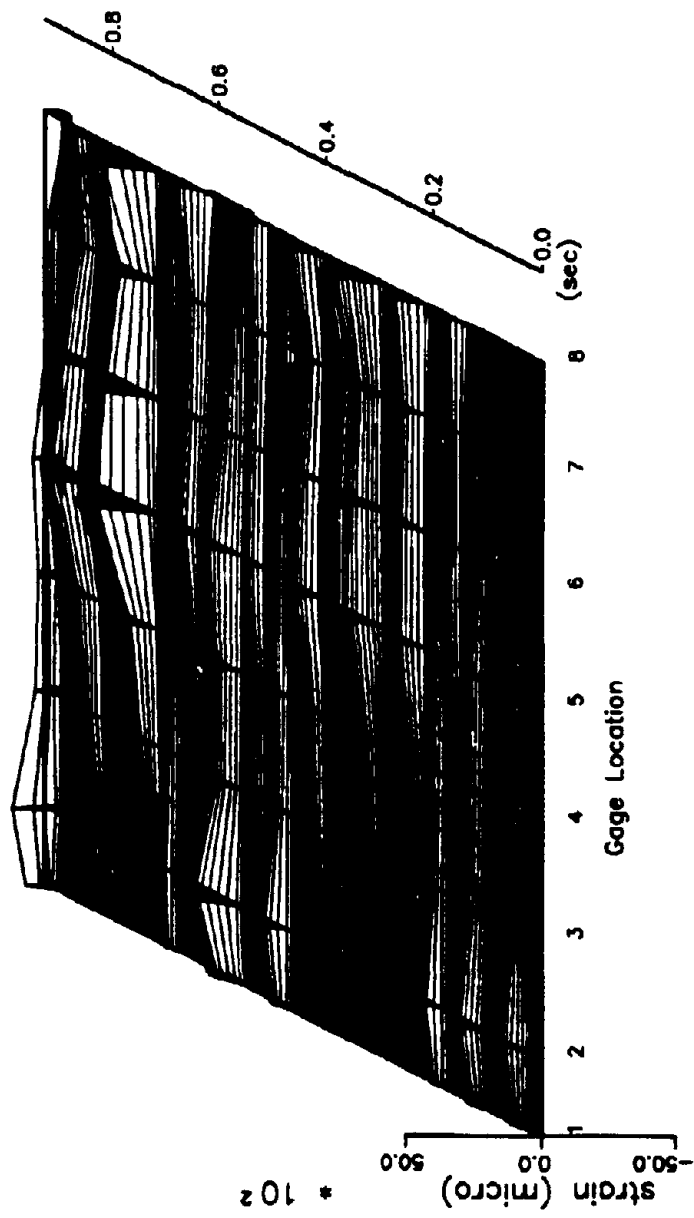


Fig. 5.39. Reinforcement Strain, Test 44

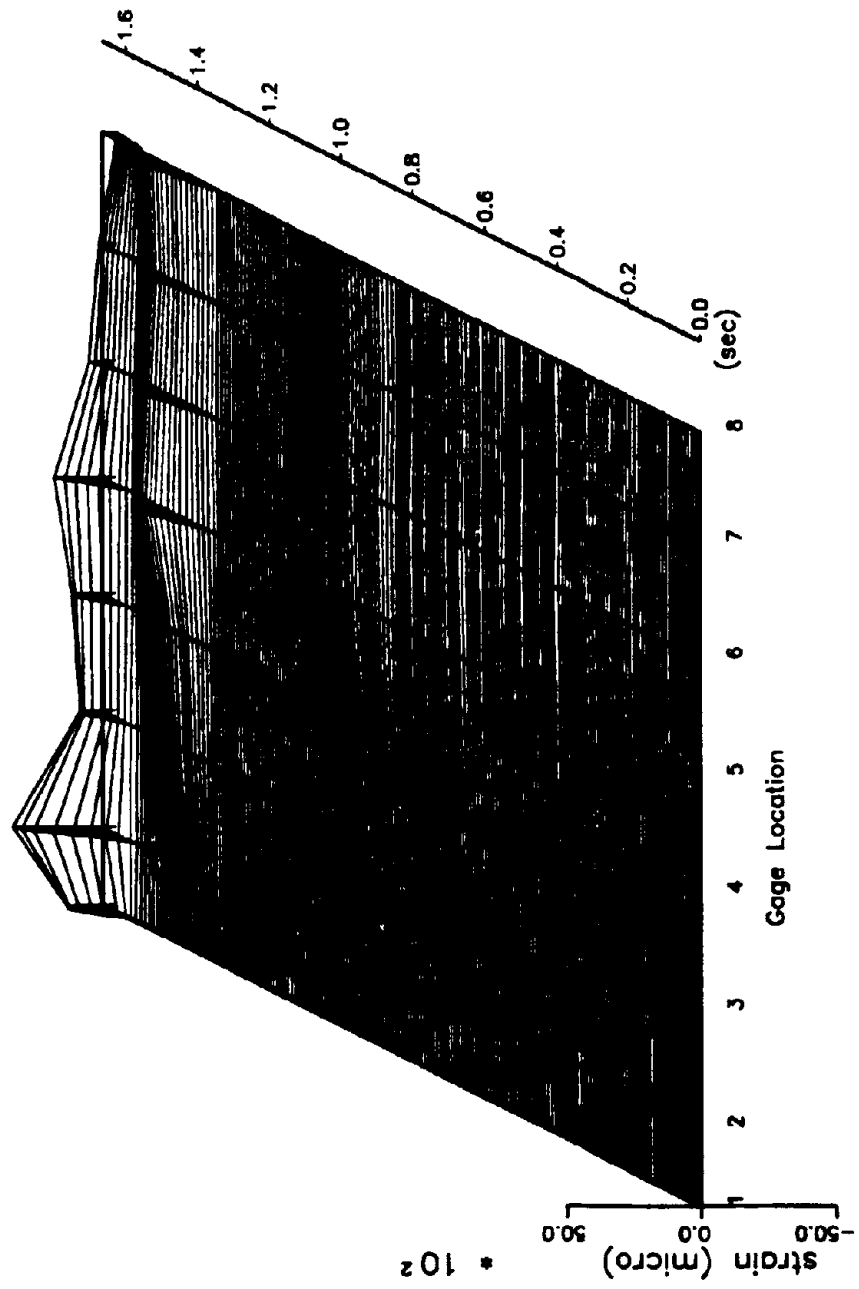
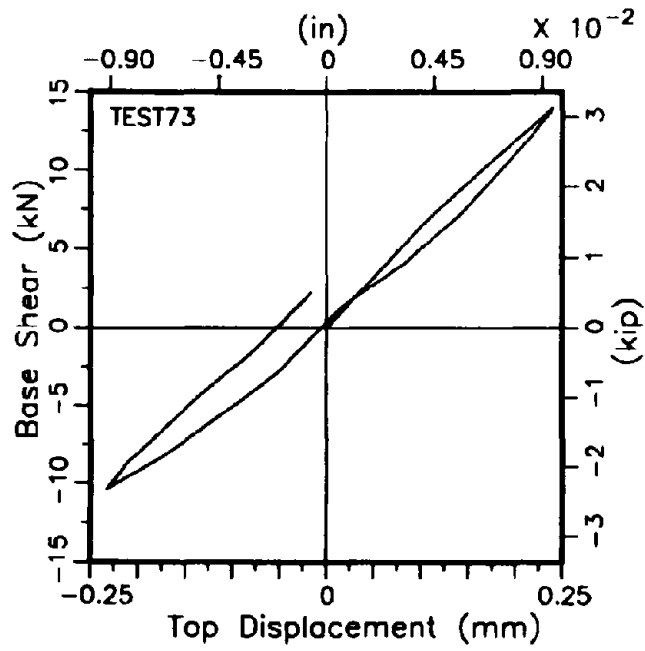
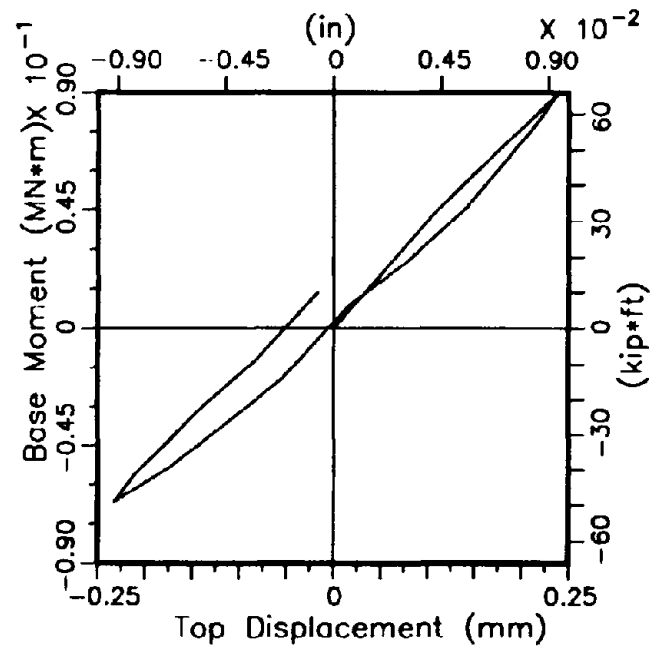


Fig. 5.40. Reinforcement Strain, Test 48

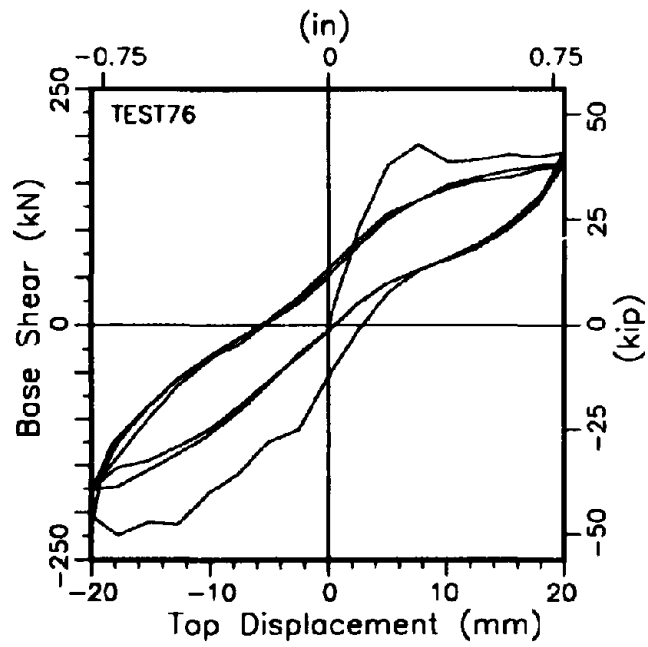


(a) Base Shear vs. Top Displacement

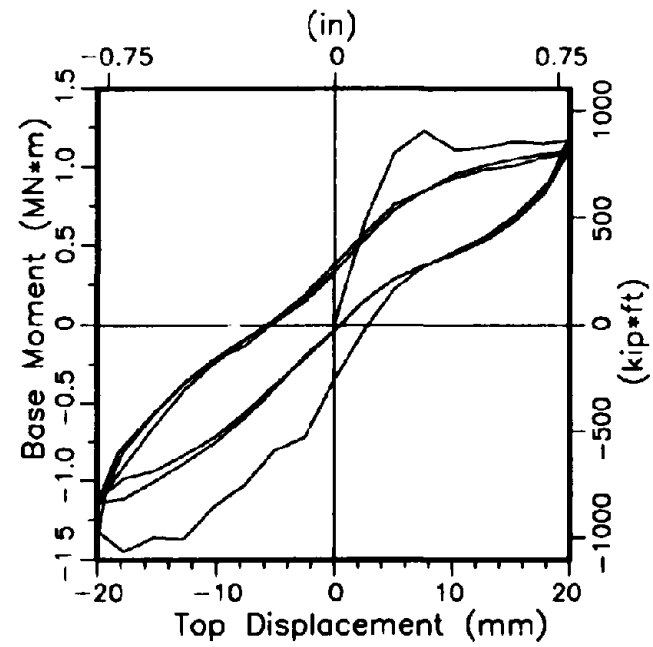


(b) Base Moment vs. Top Displacement

Fig. 5.41. Load-Displacement Behavior, Test 73

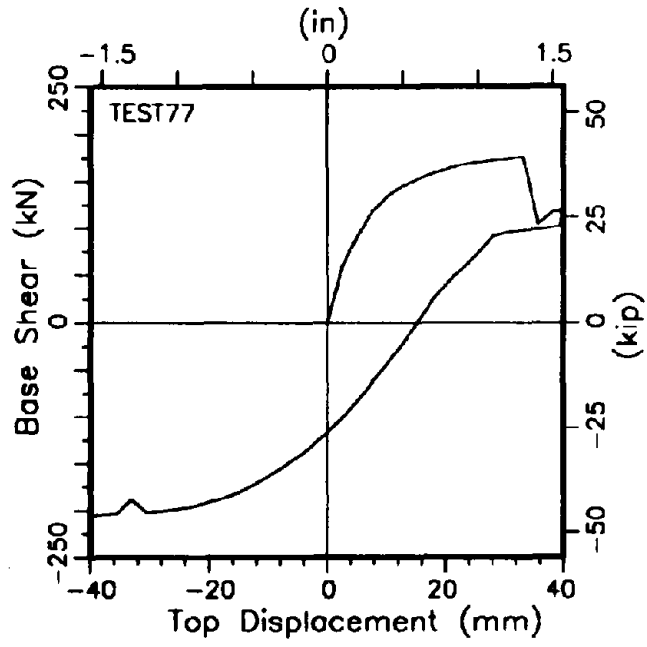


(a) Base Shear vs. Top Displacement

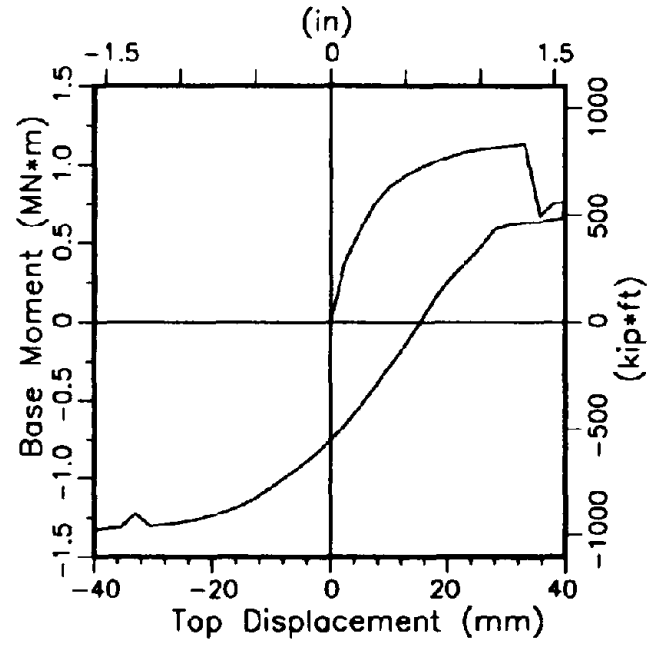


(b) Base Moment vs. Top Displacement

Fig. 5.42. Load-Displacement Behavior, Test 76

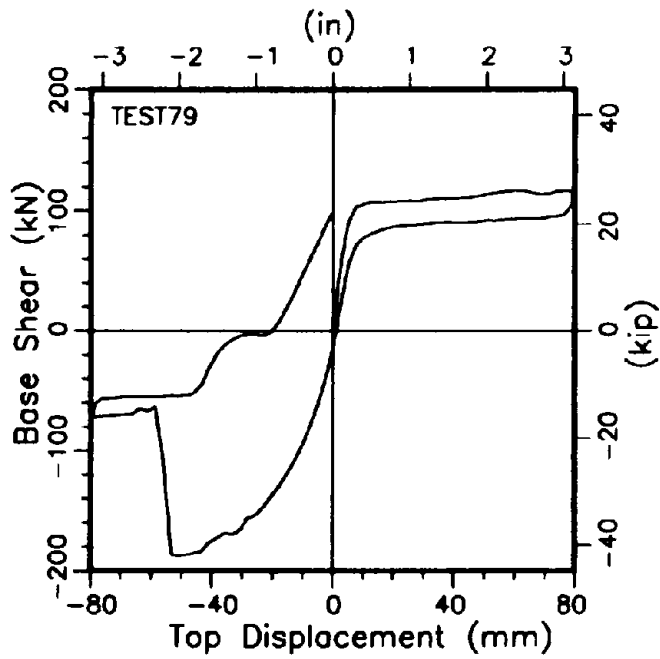


(a) Base Shear vs. Top Displacement

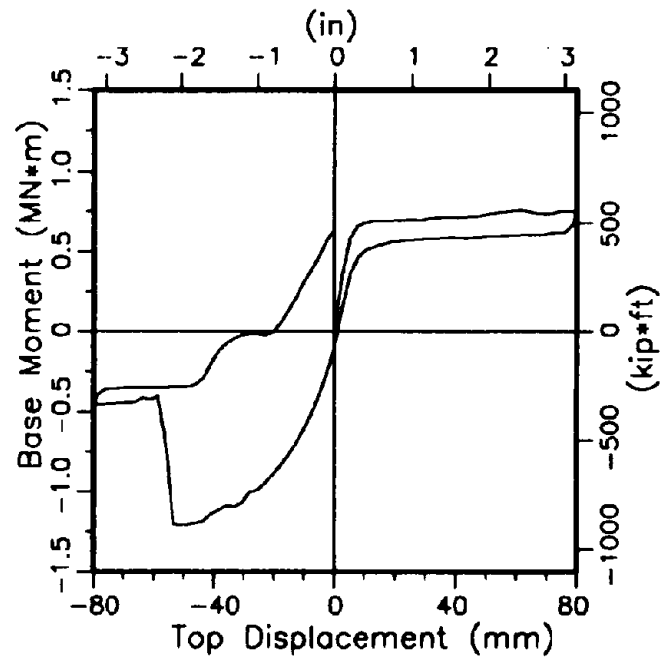


(b) Base Moment vs. Top Displacement

Fig. 5.43. Load-Displacement Behavior, Test 77



(a) Base Shear vs. Top Displacement



(b) Base Moment vs. Top Displacement

Fig. 5.44. Load-Displacement Behavior, Test 79

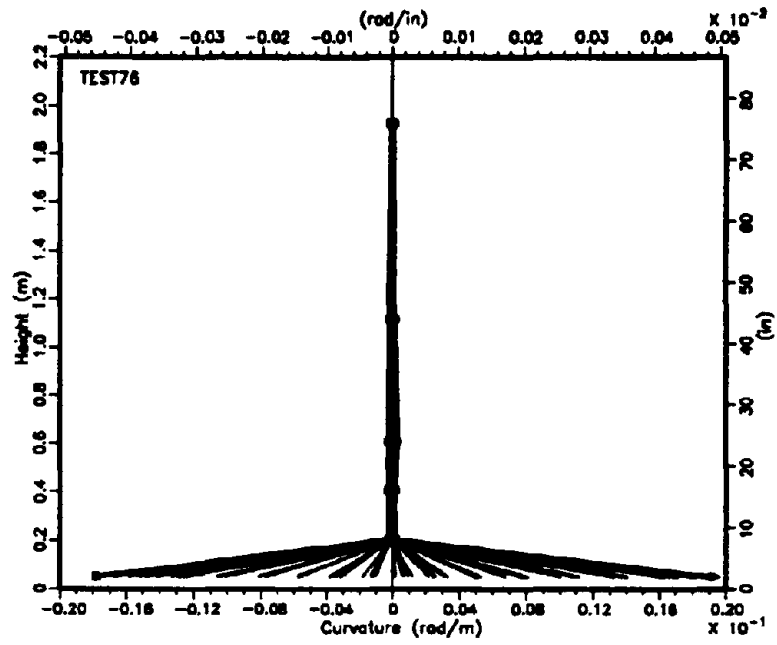


Fig. 5.45. Curvature Distribution, Test 76

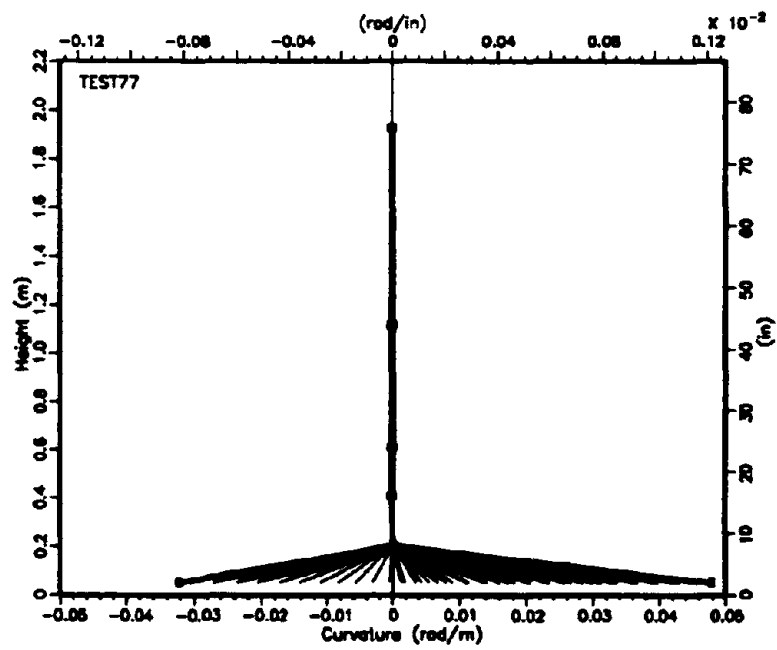


Fig. 5.46. Curvature Distribution, Test 77

## 6. DEVELOPMENTS FOR THE TCCMAR 5-STORY BUILDING TEST

The principal goal of the 3-story shear wall test was the development of the GSD testing procedure for the full-scale testing of a reinforced concrete masonry 5-story building [22], shown in Fig. 6.1. Several observations made during the 3-story shear wall tests suggest problems which would be encountered in the testing of the 5-story building. In the early stages of the 3-story wall tests, the restoring force time-histories indicated considerable level of higher mode response even though the displacement error tolerance was tight. One can expect that this tendency might be more severe in the case of a 5-story building test, since the stiffness of the structure is higher, and the number of degrees of freedom is larger. In the following, theoretical considerations on the convergence of the MDOF testing system and its consequences are developed, followed by an outline for improvements.

### 6.1. Convergence Analysis

It can be shown that the convergence of the structural displacement to the target displacement is obtained when the inner control loop algorithm is given by expression (2.24) or (2.25). For simplicity of the analysis, it is assumed that the system is linear (stiffness matrix of the test structure is  $\mathbf{K}$ , elastomeric pad stiffness is  $k_p$ ), and that

$$\mathbf{x}_a^{(k)} = \mathbf{x}_a^{(k)} \quad (6.1)$$

for all iteration steps  $k$ . This implies that the actuators perfectly follow the displacement command signals. Then algorithms (2.24) or (2.25) result in the following equation:



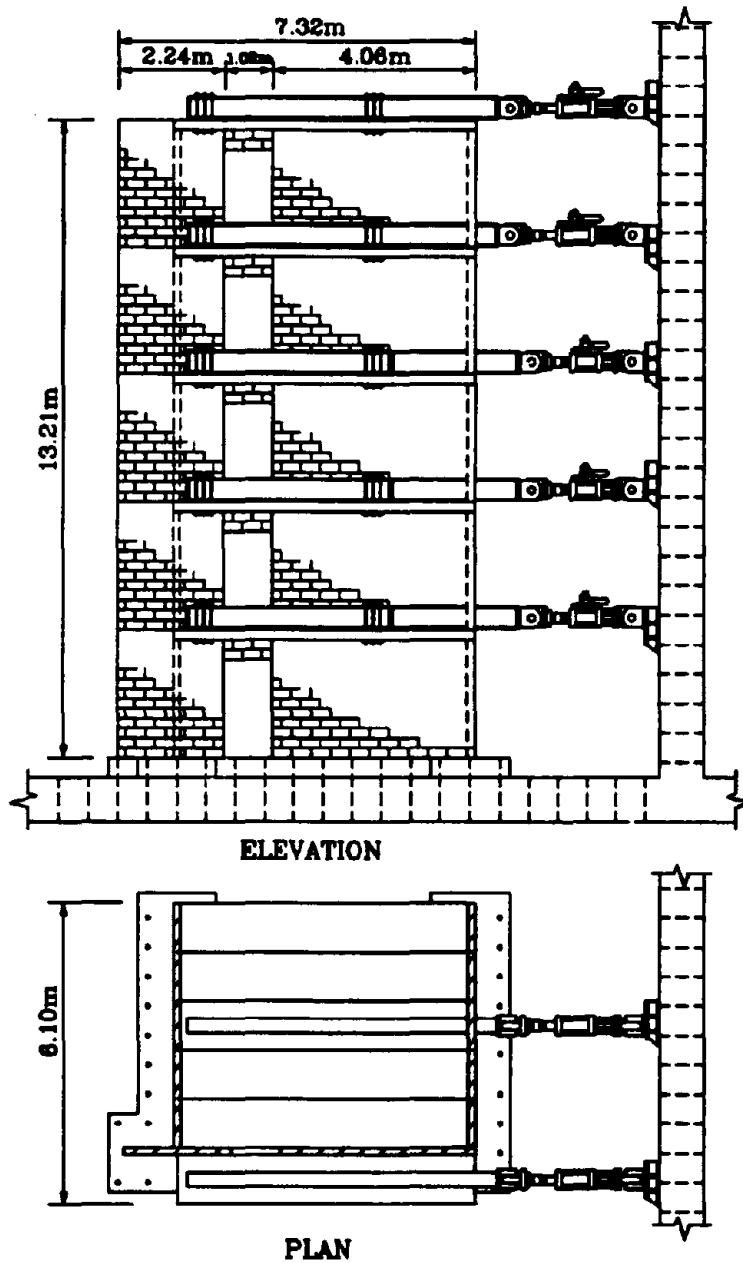


Fig. 6.1. TCCMAR 5-Story Research Building and Test Setup

$$\mathbf{x}_s^{(k+1)} = \mathbf{x}_s^{(k)} + \nu (\mathbf{x}_{target} - \mathbf{x}^{(k)}), \quad k=0,1,\dots \quad (6.2)$$

where  $\nu$  is a scalar multiplier such that  $\nu > 1$ ,  $\mathbf{x}_{target}$  is the structural displacement vector to be achieved,  $\mathbf{x}_s^{(k)}$  and  $\mathbf{x}^{(k)}$  are the actuator and structural displacement vectors at iteration step  $k$ , respectively.

Assuming a linear system as above, and substituting eqn. (2.9) in eqn. (6.2), a difference equation for the structural displacement is obtained as

$$\mathbf{x}^{(k+1)} = (\mathbf{I} - \nu \mathbf{Q}^{-1}) \mathbf{x}^{(k)} + \nu \mathbf{Q}^{-1} \mathbf{x}_{target} \quad k=0,1,\dots \quad (6.3)$$

along with the initial condition,  $\mathbf{x}^{(0)}$ .

If the target structural displacement vector  $\mathbf{x}_{target}$  is constant during the iteration, this difference equation can be solved in the following manner. The equation is rearranged to the form

$$\mathbf{x}_{target} - \mathbf{x}^{(k+1)} = (\mathbf{I} - \nu \mathbf{Q}^{-1}) (\mathbf{x}_{target} - \mathbf{x}^{(k)}) \quad (6.4)$$

Hence, if

$$\mathbf{u}^{(k)} = \mathbf{x}_{target} - \mathbf{x}^{(k)}, \quad k=0,1,\dots \quad (6.5)$$

is defined and substituted into eqn.(6.3), it is easy to show that  $\mathbf{u}^{(k)}$  is given by

$$\mathbf{u}^{(k)} = (\mathbf{I} - \nu \mathbf{Q}^{-1})^k \mathbf{u}^{(0)} \quad k=0,1,\dots \quad (6.6)$$

and the solution of (6.3) is expressed by

$$\mathbf{x}^{(k)} = \mathbf{x}_{target} - \mathbf{u}^{(k)} \quad (6.7)$$

Since the matrix  $\mathbf{Q}$  has the same eigenvectors as the stiffness matrix  $\mathbf{K}$ , and the corresponding eigenvalues are  $1 + \lambda_j / k_j$  ( $\lambda_j$  = the eigenvalue of  $\mathbf{K}$ ), the solution can be decomposed into

modes using the eigenvectors of the stiffness matrix, as

$$w_i^{(k)} = \mu_i^k w_i^{(0)}, \quad k=0,1,\dots \quad (6.8)$$

where  $w_i^{(k)}$  is the  $i$ th mode component in the vector  $u^{(k)}$ , i.e.

$$u^{(k)} = \Phi w^{(k)} \quad (6.9)$$

and

$$\mu_i = 1 - \frac{\nu}{1 + \frac{\lambda_i}{k_p}}, \quad i=1,2,\dots,n \quad (6.10)$$

Therefore, if  $|\mu_i| < 1$  (preferably  $0 \leq \mu_i < 1$ ), all the components of  $u^{(k)}$  converge to zero as  $k \rightarrow \infty$ . The numbers  $\mu_i$  ( $i=1,2,\dots,n$ ) correspond to the rate of convergence of the structural displacement to the target displacement in the  $i$ th mode. As can be seen in the above expression,  $\mu_i$  is larger for a higher mode (with larger  $\lambda_i$ ), thus the convergence is slower.

As an example, Fig. 6.2 illustrates the convergence behavior of the 2-DOF model shown in Fig. 2.3. Several simulated structural displacement paths are shown, starting from different initial structural displacements. Only the first seven iterated points are shown in the figure. In the two degrees of freedom displacement domain shown in Fig. 6.2, convergence along a positive slope corresponds to dominant first mode response while convergence along a negative slope indicates dominance of second mode contribution. In Fig. 6.2, it can be seen that the second mode (the highest mode in this case) becomes dominant in the displacement error vector near the target displacement point. Also, overshooting of individual DOFs can be observed which slows down the convergence behavior.

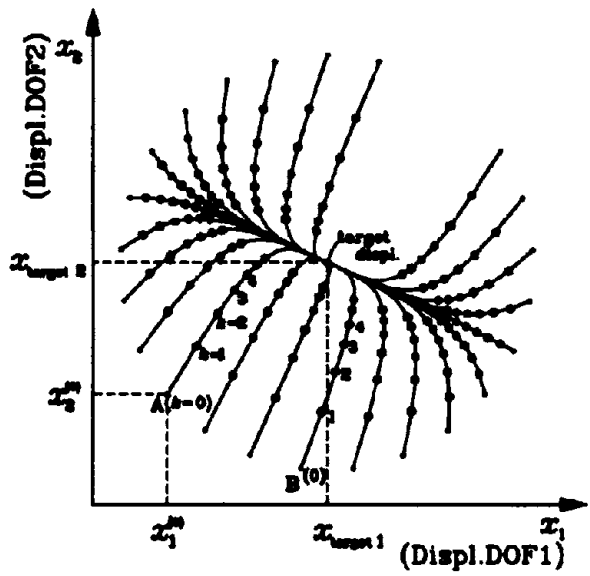


Fig. 6.2. Convergence Behavior of 2-DOF Model

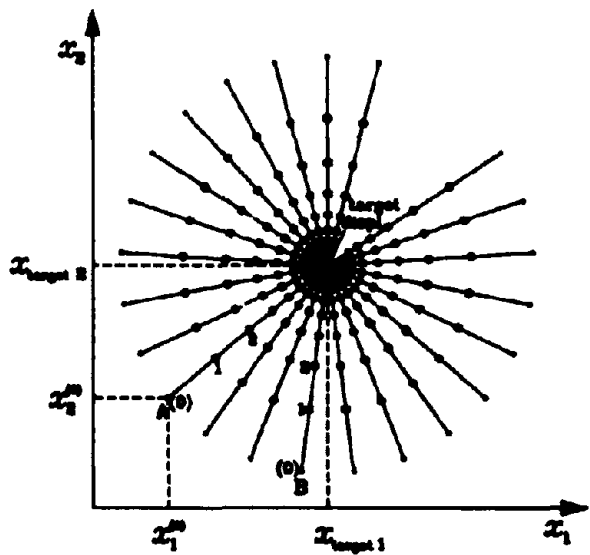


Fig. 6.3. Convergence of 2-DOF Model with Improved Algorithm

## 6.2. Improvement of Convergence

Since the higher mode converges slower than other modes, as shown in the previous section, the residual structural displacement error at the end of the inner loop iteration will contain predominant highest mode components. This may induce unrealistically large higher mode response, and it also significantly slows down the speed of convergence.

Hence, one of improvements considered to the inner control loop algorithm is to compensate the slow convergence of higher modes. In order to accomplish this, the inner control loop algorithm takes on the form

$$\mathbf{x}_a^{(k+1)} = \mathbf{x}_a^{(k)} + \mathbf{N}(\mathbf{x}_{target} - \hat{\mathbf{x}}^{(k)}) \quad (6.11)$$

where  $\mathbf{N}$  is an  $n \times n$  scaling matrix. By choosing the value of  $\mathbf{N}$ , the convergence properties of the algorithm can be controlled. The algorithm used in the three-story wall tests can be treated as a special case where

$$\mathbf{N} = \nu \mathbf{I} \quad (6.12)$$

In the above 2-DOF linear system example, if the matrix  $\mathbf{Q}$  is known through measurements, the choice

$$\mathbf{N} = \theta \mathbf{Q} \quad (6.13)$$

where  $\theta$  is a reduction factor, gives the structural displacement paths shown in Fig. 6.3. Note that all the modes have the same convergence rate in this case, and no overshooting is encountered.

In the actual testing, it is advantageous to set the matrix  $\mathbf{N}$  based on the real-time measurement (or pre-test instrumentation) of the amplification matrix  $\mathbf{Q}$ . This approach poses other technical issues with the measurement and on-line update of the estimated structural

stiffness matrix. These issues will be addressed in subsequent papers.

These latest improvements to the inner loop algorithm of the GSD procedure are implemented and tested for the 5-story full scale masonry research building test. Due to the stiff nature of the proposed 5-story research building, explicit integration schemes would require severe restrictions on the time step to maintain numerical stability, thus, implicit integration schemes with the discussed error correction are implemented. Some of these improved implementations are described in [22].

## **7. CONCLUSIONS**

**A testing methodology for full-scale reinforced concrete or masonry structures subjected to simulated seismic loads under laboratory conditions was developed, and the implementation and verification on three-story full-scale reinforced masonry shear walls was discussed. The new test method allows realistic seismic input simulation and trace of higher mode effects, even in the initial undamaged state of the structure. Problems typically associated with the stiff coupling between servo-controlled actuators in a multi-degree of freedom system were overcome with the introduction of elastomeric loading pads, which act as displacement amplifiers in the loading system. Advances in the actuator control loop also allowed testing without numerical damping in the time integration scheme, thus permitting the tested three-degree of freedom masonry shear walls to respond with lateral load distribution patterns consistent with the degree of structural stiffness deterioration.**

**With selected seismic ground motion input segments, stiff multi-degree of freedom structures can now be tested under realistic seismic loads to any predetermined critical design limit state. The Generated Sequential Displacement testing technique is also applied in the first U.S. full-scale building test on a five-story reinforced concrete masonry building.**

## REFERENCES

- 1) Okamoto, S. and Noland, J., "U.S.-Japan Coordinated Program on Masonry Research," *Dynamic Response of Structures* (Hart, G.C. and Nelson, B. eds.), Proc. 3rd ASCE conf., pp.55-70, University of California, Los Angeles, 1986.
- 2) Ewing, R.D., Kariotis, J.S., Engelkirk R.E. and Hart, G.C., "Analytical Modeling for Reinforced Masonry Buildings and Components - TCCMAR Category 2 Program," 3rd Meeting of the Joint Technical Coordinating Committee on Masonry Research U.S.-Japan Coordinated Earthquake Research Program, Tomaru, Japan, 1987.
- 3) Seible, F. and Hegemier, G.A., "From Materials and Components to Masonry Prototype Structures, the TCCMAR-U.S. Experimental Program," Proc. 4th North American Masonry Conference (Hart, G.C. and Kariotis, J eds.), University of California, Los Angeles, 1987.
- 4) Seible, F. and La Rovere, H.L., "Summary on Pseudodynamic Testing," SSRP-87/01, Department of AMES, University of California, San Diego, 1987.
- 5) Takanashi, K. and Nakashima, M., "A State of the Art: Japanese Activities on On-Line Computer Test Control Method," Report of the Inst. of Industrial Science, The University of Tokyo, Vol.32, No.3, 1986.



- 6) Shing, P.B. and Mahin, S.A., "Pseudodynamic Test Method for Seismic Performance Evaluation: Theory and Implementation," UCB/EERC-84/01, College of Engineering, University of California, Berkeley, 1984.
- 7) Shing, P.B., Manivannan, T. and Carter, E., "Evaluation of Reinforced Masonry Shear Wall Components by Pseudodynamic Testing," Proc. Fourth U.S. National Conference on Earthquake Engineering, vol.2, pp.829-838, 1990.
- 8) Yamazaki, Y., Kaminosono, T., Teshigawara, M., and Seible, F., "The Japanese 5-Story Full-Scale Reinforced Concrete Masonry Test - Pseudo-Dynamic and Ultimate Load Test Results," The Masonry Society Journal, Vol.7, No.2, T1-T18, 1988.
- 9) Mahin, S.A. and Shing, P.B., "Pseudodynamic Method for Seismic Testing," Journal of Structural Engineering, ASCE, Vol.111, No.7, pp.1482-1503, 1985.
- 10) Nakashima, M., "Summary of BRI Works on Developing Pseudo Dynamic Testing Techniques," 7th JTCC Meeting of US-Japan Cooperative Research Program Utilizing Large Scale Testing Facilities, 1987.
- 11) Yamazaki, Y., Nakashima, M. and Kaminosono, T., "Reliability of Pseudodynamic Test in Earthquake Response Simulation," Journal of Structural Engineering, ASCE, Vol.115, pp.2098-2112, 1989.
- 12) Shing, P.B. and Mahin, S.A., "Experimental Error Propagation in Pseudodynamic Testing," UCB/EERC-83/12, Earthquake Engineering Research Center, University of California, Berkeley, 1983.

- 13) Thewalt, C.R. and Mahin, S.A., "Hybrid Solution Techniques for Generalized Pseudodynamic Testing," UCB/EERC-87/09, Engineering Research Center, University of California, Berkeley, 1987.
- 14) Shing, P.B., Manivannan, T. and Carter, E., "Implicit Time Integration for Pseudodynamic Tests," *Earthquake Engineering & Structural Dynamics*, Vol.20, pp.551-576, 1991.
- 15) Nakashima, M. and Kato, H., "Accuracy of Earthquake Response in Pseudo Dynamic Testing," *Proceedings of the Seventh Japan Earthquake Engineering Symposium*, Tokyo, Japan, pp. 1273-1278, 1986 (in Japanese).
- 16) Nakashima, M. and Kato, H., "Experimental Error Growth in On-Line Computer Test Control Method," *Research Paper*, Building Research Institute, Ministry of Construction, No. 123, 1987.
- 17) Saffarini, H.S. and Wilson, E.L., "New Approaches in the Structural Analysis of Building Systems," UCB/SESM-83/08, Department of Civil Engineering, University of California, Berkeley, 1983.
- 18) Press, W.H., Flannery, B.P., Teukolsky, S.A. and Vetterling, W.T., "Numerical Recipes (The Art of Scientific Computing)," Cambridge University Press, 1986.
- 19) Gill, P.E., Murray, W. and Wright, M.H., "Numerical Linear Algebra and Optimization Vol.1," Addison-Wesley, 1991.

- 20) Mahin, S.A., Shing, P.B., Thewalt, C.R. and Hanson, R.D., "Pseudodynamic Test Method -Current Status and Future Directions." *Journal of Structural Engineering*, Vol.115, No.8, pp.2113-2128, ASCE, 1989.
- 21) Seible, F. and Igarashi, A., "Full Scale Testing of Masonry Structures under Simulated Seismic Loadings," *Experimental and Numerical Methods in Earthquake Engineering* (Donea,J. and Jones,P.M. eds.), pp.119-148, 1991.
- 22) Seible, F., Priestley, M.J.N., Hegemier, G.A., Kingsley, G.R., Igarashi, A. and Kürkchubasche, A.G., "The Test Plan for the 5-Story Full-Scale TCCMAR Research Building," SSRP-91/07, Univ. of California, San Diego, Dept. of AMES, 1991.
- 23) Seible, F, Hegemier, G.A., Priestley, M.J.N., Kingsley, G., Kürkchubasche,A. and Igarashi,A., "The U.S.-TCCMAR 5-Story Full-Scale Masonry Research Building Test," Report No. TR-92/01, University of California, Department of AMES, 1992.
- 24) Igarashi, A., Seible, F. and Hegemier, G.A., "Testing of Full Scale Shear Wall Structures under Seismic Load," *Proc. Tenth World Conference on Earthquake Engineering*, pp.2653-2658, Balkema, 1992.

Document 14

DOCN 000005538

AN 6032

DA 821200

PG 24

PC NTIS

TI Housing the Hispanic Population: Are Special Programs and Policies Needed.

AU Hakken, Jon

IN Department of Housing and Urban Development, Washington DC. Office of Policy Development and Research.

AV HUD USER, P.O. Box 6091, Rockville, MD 20850.

DE Hispanic persons. Housing discrimination. Needs assessment. Equal opportunity housing laws. Federal housing subsidy prgs.

FM REPORT

AB This paper explores the consequences for Federal housing policy of the recent explosive growth of the Hispanic population in the United States. By comparing the housing problems faced by Hispanic households with those of Black and White households of similar family size and income, the author seeks to identify the special housing needs of Hispanic households and determine whether current HUD programs are adequately addressing them. Previously published studies have shown that although Blacks and Hispanics experience similar incidences of inadequate housing conditions, housing discrimination, and residential segregation, their participation in HUD programs is disturbingly low. Blacks file fair housing complaints at a rate eleven times that of Hispanics. The author notes that enlisting community-based organizations to conduct education, outreach, and investigation of housing discrimination has yielded encouraging results. In addition, poor Hispanic households are only half as likely as poor Blacks to live in HUD-subsidized rental housing, a fact that the author attributes in large part to the lack of availability of HUD-subsidized rental projects in Hispanic neighborhoods. Hispanic participation rates were much more nearly proportionate in the Section 8 voucher program, as well as in other means-tested subsidy programs such as Medicaid, food stamps and subsidized school lunch program programs that would allow Hispanics to remain in predominately Hispanic neighborhoods.